Title
Advanced ignition for automotive engines

Author
Pineda, Daniel Ivan

Publication Date
2017

Peer reviewed|Thesis/dissertation

Advanced ignition for automotive engines

by

Daniel Ivan Pineda

A dissertation submitted in partial satisfaction of the

requirements for the degree of

Doctor of Philosophy

in

Engineering – Mechanical Engineering

in the

Graduate Division

of the

University of California, Berkeley

Committee in charge:

Professor Jyh-Yuan Chen, Chair
Professor Carlos Fernandez-Pello
Professor David B. Graves

Spring 2017

Advanced ignition for automotive engines

Abstract

Advanced ignition for automotive engines

by

Daniel Ivan Pineda

Doctor of Philosophy in Engineering – Mechanical Engineering

University of California, Berkeley

Professor Jyh-Yuan Chen, Chair

Spark plugs have been igniting combustible mixtures like those found in automotive engines for over a century, and the principles of the associated ignition techniques using *thermal* plasma (inductive or capacitive sparks) have remained relatively unchanged during that time. However, internal combustion engines are increasingly operating with boosted intake pressures (i.e. turbo- or super-charged) in order to maintain power output while simultaneously reducing engine size and weight, and they are also operating with increased recirculated exhaust gas dilution to reduce the production of harmful nitrogen oxides. This "downsizing" to increase fuel economy compounded with diluting to decrease emissions leads to challenges in both obtaining traditional ignition and promoting sufficiently fast combustion under this operating paradigm. In conjunction with appropriate electrode design, transient *non-thermal* plasma can exploit certain non-equilibrium chemistry and physics to bypass these challenges and ultimately promote more reliable ignition and faster combustion. Applied and fundamental experimental investigations of two different advanced ignition techniques are presented: 1) corona discharges igniting gasoline/air/exhaust mixtures in a boosted direct-injection single cylinder research engine and 2) repetitively pulsed nanosecond discharges igniting methane/air mixtures in a constant volume chamber. The engine experimental results show significant decreases in fuel consumption and nitrogen oxide emissions under boosted operation, and both experiments demonstrate more robust ignition and faster flame development. The constant volume chamber results in particular raise important questions about the relative contributions of chemistry and transport to the experimentally observed combustion enhancement. These results highlight the critical importance of electrode design in advanced ignition techniques—the shape and position of electrodes greatly influences the hydrodynamics of developing flame kernels into fuel-air charges. While this work demonstrates that non-thermal plasma ignition is a promising solution to both increase fuel economy and decrease emissions of future automotive engines, much work remains to be done to understand the beneficial coupling between the detailed non-thermal plasma chemistry and the hydrodynamics associated with these real ignition devices.

To my family

Contents

List of Figures

List of Tables

Nomenclature

$[C_i]$	Concentration
$\Delta\theta_b$	Rapid burning angle; number of crank angles between CA10 and CA90
$\Delta\theta_d$	Flame development time; number of crank angles between ignition and CA10
$\Delta\theta_o$	Overall burning angle; sum of $\Delta\theta_d$ and $\Delta\theta_b$
η	Thermodynamic efficiency
γ	Ratio of specific heats
$\hat{R}_u$	Universal gas constant
μWASP	Microwave-Assisted Spark Plug
ϕ	Equivalence ratio
τ_d	Flame development time; time between ignition and when 10% of the total heat release from the charge has been achieved
τ_o	Overall burning time; sum of τ_d and τ_r
τ_r	Flame rise time; time between when 10% and 90% of the total heat release from the charge has been achieved
θ	Crank angle degree
θ_{ign}	Ignition crank angle
$\vec{E}$	Electric field
E/n	Reduced electric field
E_a	Activation energy
L_f	Flame kernel size
n_i	Moles or molar density of species i

P Pressure

r_c Compression ratio

s_b Burned flame speed

s_u Unburned flame speed

T Temperature

V Volume

X_i Mole fraction of species i

C_2H_5OH Ethanol

CH_4 Methane

CO_2 Carbon dioxide

CO Carbon monoxide

H_2 Hydrogen

N_2 Nitrogen

NO_X Nitrogen oxides

O_2 Oxygen

UHC Unburned hydrocarbons

AC Alternating Current

BSFC Brake-Specific Fuel Consumption

CA10 Crank angle where 10% of the total heat release from the charge has been achieved

CA50 Crank angle where 50% of the total heat release from the charge has been achieved

CA90 Crank angle where 90% of the total heat release from the charge has been achieved

CAFE Corporate Average Fuel Economy

CI Compression Ignition

CNG Compressed Natural Gas

COV_{IMEP} Coefficient of Variation in Indicated Mean Effective Pressure

DC Direct Current

DI Direct-Injection

EGR Exhaust Gas Recirculation

HCCI Homogeneous Charge Compression Ignition

HEI High-Energy Ignition

HP Horsepower

HRR Heat Release Rate

MBT Maximum Brake Torque

MEP Mean Effective Pressure

MIE Minimum Ignition Energy

PAI Plasma-Assisted Ignition

PND Pulsed Nanosecond Discharge

RF Radio Frequency

RFCDI Radio Frequency Corona Discharge Ignition

RFS Renewable Fuel Standard

RON Research Octane Number

SCR Selective Catalytic Reduction

SCRE Single Cylinder Research Engine

SI Spark Ignition

TDC Top Dead Center

TEL Tetra-ethyl-lead

Acknowledgments

This section of my dissertation is probably longer than those of most dissertations, but I feel particularly lucky—I have never felt like I simply received what I have *deserved*—that word still makes me uncomfortable. Admittedly, I have been wanting to write this for some time, if only to finally express my gratitude to the universe, and I would be remiss if I missed anyone. The central theme is as follows: Someone took a chance on me, and I pushed myself to meet those new expectations, becoming better in the process. It's a good formula. It's the best any student of any subject can hope for.

Broadly, I would like to thank the National Science Foundation for both the direct and indirect support from which I have benefited over the course of my lifetime. Many of my favorite educational science programs that I enjoyed as a child were sponsored by the NSF, and I know that this has been a significant influence on my choice of career path. It was only fitting, I suppose, that I would circle back and receive more support from them as a graduate student. Much of the work presented in this dissertation was supported by the NSF Graduate Research Fellowship Program, Grant No. DGE 1106400. I provide more specific agency acknowledgments in the dissertation chapters for which they are applicable, but notably, much of my conference travel during my time as a graduate student was paid for by the Western States Section of the Combustion Institute.

I am grateful for the professional mentorship I have received during the past decade. Many of these individuals believed in me even when I did not believe in myself, and I am forever thankful for that. I thank Dr. Elaine Neenan of the University of Texas Health Science Center at San Antonio for her unwavering support in my pursuits during my employment in the public health sector. An amazing woman of strong moral character, she has consistently inspired me to make sure that my work is always completed with an eye on the greater good. I thank Professor Janet L. Ellzey of The University of Texas at Austin and Dr. Colin Healey Smith, who both took a chance on me by bringing me in to Professor Ellzey's research group. Both of them have instilled in me a motivation to be the most honest scientist I can be, and to remember that the most interesting discoveries often happen by accident and should be celebrated rather than reviled. In the years since, Colin has become one of my best friends and has continued to provide valuable guidance for me as I have navigated through graduate school. That being said, my career certainly still wouldn't be anywhere near viable without the mentorship I received at UC Berkeley. I am thankful to Professor Jyh-Yuan Chen for being a wonderful research advisor— he allowed me to pursue many topics that I found personally engaging, and I am well aware that not every graduate student receives that opportunity. Professor Robert Dibble has always challenged and motivated me to think more critically about research problems, while simultaneously challenging and motivating me to have more fun with it, something with which I have always struggled—and he could tell from the day we met. Critically, both Bob and J.Y. allowed me to make mistakes from which I would learn something, and this has made me all the better a researcher. Professor Carlos Fernandez-Pello has been a wonderful mentor, and I will always appreciate his life advice as well as his teaching methods. He has inspired me to take on

the rigorous academic life ahead of me. Professor David Graves really came through for me by agreeing to be on my committees despite us having not met before, and I'm grateful to him for his amicability and open-mindedness. His insights on my research have only made my work better. Outside of research, there are some faculty at UC Berkeley who deserve recognition for their commitment to their pedagogy. Instructors of endless patience, these people set the standard for myself for my future life in academia: Professors Fotini Chow, Robert Harley, David Chandler, and Philip Geissler are among the most caring instructors from whom I've ever had the pleasure to learn. They have truly helped me round out my studies in my minors of Environmental Engineering and Chemistry.

Much of the work presented here would not have been possible without Professor Chen's graduate students who came before me and set in motion both the funding and the experimental apparatuses I used in my research: Benjamin Wolk and Anthony DeFilippo. Both have laid the groundwork that I was able to build upon, and Ben in particular never hesitated to help me whenever I asked for it, even after he had graduated. Additionally, I would not have survived navigating the perils of graduate school at UC Berkeley without the help from my fellow labmates Don Frederick, Greg Chin, Tiernan Casey, Xian Shi, Yulin Chen, Je Ir Ryu, Alex Frank, and Charles Scudiere. Outside of Professor Chen's lab, I benefited greatly both professionally and personally from conversations with Vi Rapp, Casey Zak, Ravi Singh, Jim Oreluk, James Urban, Maria Thomsen-Solis, Dan Murphy, Sarah Scott, Sara McAllister, and Shmuel Link. Beyond the scope of this dissertation, my research contributions on working fluid replacement in internal combustion engines would have been impossible without the groundwork laid by Miguel Sierra-Aznar and Tim Sennott, and it would have been much more challenging without the essential contributions of Bradley Cage, a rising star undergraduate who has since become a great friend of mine.

Behind the scenes and often in the front lines, the staff of the department have kept the machinery of my Ph.D. in well-oiled operation. Yawo Akpawu and Isabel Blanco of the Student Services Office have helped me navigate endless paperwork during my service as a Graduate Student Instructor and during my own qualifying exam scheduling crisis. The technical staff, including Pete Graham, Mick Franssen, and Jesse Lopez really helped me out when I needed to machine various parts for my experiments. I especially want to thank Michael Neufer, Alex Jordan, and Scott McCormick; their technical expertise enabled me to become a better instructor and motivated me to come up with new ideas to teach at the college level. I cannot emphasize enough the importance of these individuals to the well-being and success of graduate students in the Mechanical Engineering Department.

A few individuals I've come to know both in Berkeley and the broader San Francisco Bay Area have made the time I have spent here both fun and enjoyable: Colin Ho, Matthew Wright, Andrew Sabelhaus, Rebecca Freund, Amy Arneson, David Torres Irribarra, Ana Maria Albornoz Reitze, Lianne Ippel, Alysha Owen, Kurt Lavetti, and Amie Knieper have all broadened my horizons and helped me make the most of life on the west coast.

Outside of Berkeley, I am lucky enough to have the support of a posse of close friends. These people have always been there for me, some of them for as long as I can remember. While they are now all over the country and the world, we have not lost each other. They

have helped me assuage my self-doubts and my fears, they have lifted my spirits and kept me honest when I needed it most. With all my heart, I thank Veronica Sandoval, Matthew Rodgers, Colin Smith, Kristin Davis, Jordan Nerison, Antonia Vita, Brenda Yang, Steven Tang, ToniAnn Treviño, Nauman Charania, Ben Kobe, Luke Hall, Ryan Kostrzewa, Geoffrey Dilly, Hannah Bull, Andrew Craft, Edward Wittlif, Akeem Roberts, and Elise Lebourg for helping me become who I am today. The list seems large, but I am very fortunate to have been alive at the same time as these amazing individuals, and that our paths have crossed as they did, however cosmically accidental it may have been. I'm proud to admit that I love each of them, and I will cherish our friendship forever.

Most importantly, I want to thank my family for the support I have received over my entire life. I was born to a family that—somehow instinctively—looks beyond their own generation. It is not a luxury; but rather, a duty, no matter the cost, no matter the hardship. The education of both myself and my brothers has always come first in my family, often times at great expense of both time and effort to my parents, particularly when I was very young. I've given them terrible headaches and scares, but I trust that I have also given them pride and joy. My parents were able to do well for themselves because their parents put them first, and I am no different. I will do my best to continue the legacy bestowed upon me. I have been given an enormous opportunity, and though this has at times put equally enormous pressure on me, I am better off for it. I am eternally grateful to my family.

Chapter 1

Introduction, motivation, and background

In gasoline internal combustion engines, the basic principles of igniting combustible mixtures with a spark plug have not changed in over 100 years. Demands on future automotive engines—driven by environmental and societal forces put in motion over the last century—necessitate an examination of practical advanced ignition strategies. The work presented in this dissertation aims to provide such an applied experimental examination in the context of immediate (5–15 years) impacts to rapidly reduce harmful emissions and increase fuel economy.

Organization of dissertation

This dissertation is presented in a fashion that begins with the "big picture" of automotive engines and their role in society, followed by a brief introduction to the fundamentals of plasma-assisted ignition. These two background topics—internal combustion engines and plasma chemistry—are, on the surface, disparate subjects individually; this dissertation aims to examine a present problem in combustion engineering by applying concepts from a subject traditionally concerned with much smaller length and timescales. The dissertation then narrows in scope to applied internal combustion engine experiments, followed by a further narrowing of scope to more fundamental constant volume chamber experiments.

1. This first chapter provides a very broad scope of the dissertation. Importantly, it outlines the social, scientific, technical, and historical contexts in which the dissertation work exists. These contexts help establish the place of the dissertation in the field of combustion and the role of combustion in the world. Automotive engines (which are, in essence, consumer products) are more outputs of engineering than of fundamental science, and do not exist in a vacuum. The historical and social contexts, in particular, are necessary for proposing reasonable and practical political and technical solutions to current energy problems. Some of these solutions are discussed, and their advan-

tages and disadvantages are weighted with how soon they can be implemented. The first chapter ultimately establishes the research and development of advanced ignition strategies as a viable method for increasing the efficiency and reducing the emissions of automotive engines in the near-term. Additionally, various combustion-specific terms and concepts used throughout the dissertation are defined and explained for the facilitation of reading the subsequent chapters.

2. The second chapter provides a brief scientific background on the ignition of combustible fuels, followed by a technical background on various advanced ignition strategies currently under active research by the engine community. The fundamental concepts of plasma-assisted ignition with respect to ignition chemistry are discussed, and a comparison of currently competing strategies is made. Ultimately, two techniques are singled out for further work presented in this dissertation: 1) corona discharge ignition and 2) pulsed nanosecond discharge ignition. The fundamental plasma chemistry of these two techniques is highly similar, but the implementation of the discharge is different.

3. The third chapter focuses on corona discharge ignition, and presents experiments utilizing this technique in a boosted gasoline direct-injected research engine. The ignition strategy is shown to provide benefits in increasing fuel efficiency and reducing emissions relative to traditional spark ignition operation. Following the presentation of results, the reasons for the observed benefits of the advanced ignition strategy are discussed with references to more fundamental experiments present in the literature.

4. The fourth chapter focuses on pulsed nanosecond discharge ignition, with an initial discussion of engine experiments in the literature that show various benefits in engine performance. This advanced ignition technique—as implemented in engine experiments—has received less attention in fundamental experiments, and so some experiments utilizing a constant volume chamber are presented. The purpose of these experiments is to clarify the reasons for the performance enhancement in the aforementioned engine experiments by others.

5. The last chapter concludes the dissertation with a thermodynamic analysis of some of the results, and provides a framework going forward for solutions. A discussion is presented that aims to bridge current current challenges in combustion with current challenges in non-thermal plasma science.

Contributions of dissertation

Contributions of the work presented in this dissertation to the increased understanding of the use of advanced ignition technologies in automotive engines include:

- Appropriate technical context for the most strategic use of advanced ignition technologies in automotive engines to increase fuel economy and reduce harmful emissions.

- Experimental data and analysis of corona discharge ignition in high-load, high-dilution internal combustion engine operation. At present, these experiments represent the highest power density exhaust gas recirculation limit extension using advanced ignition available in the literature.
- Experimental data of pulsed nanosecond discharge ignition in fuel-lean constant volume chamber tests. These experiments present the first high-speed schlieren imaging data of pulsed nanosecond discharge ignition using electrodes expected for use in automotive engines.

1.1 History of the internal combustion engine

Humans have been manipulating energy to suit their needs since antiquity, but have only in the last three centuries begun to understand the fundamental physico-chemical processes involved in combustion—namely, that there is a "mechanical equivalent of heat" (Smith, 2003) and that combustion is an oxidative process that converts reactants to products (Guillaume et al., 2016). In modern history, three forces have primarily driven innovation in internal combustion engines: 1) increasing fuel efficiency and energy security, 2) reducing pollutants harmful to human health, and 3) reducing emissions harmful to the environment. The evolution of the internal combustion engine in the early 20th century was largely driven by demands for increased fuel efficiency and power, without much regard to human health or the environment. In the 1960s and 1970s, negative impacts from combustion on human health and the environment motivated widespread pollutant regulations, though emerging energy crises concurrently constrained engine manufacturers to maintain efficiency improvement efforts. Today, concerns about anthropogenic climate change combine these efforts to both reduce greenhouse gas emissions and increase fuel efficiency, since research efforts that accomplish one of these goals typically also accomplish the other.

Heat engines and the development of thermodynamics

A heat engine is a term used to describe any device that converts thermal energy (heat) into mechanical energy, which we often consider "useful work" (Callen, 1985). The heat engines considered in this dissertation are nearly always practically employed in assemblies in which an expanding gas in a cylinder presses against a movable piston and *displaces* it some distance. For the heat engines discussed here, this thermal energy must first come from the chemical energy stored in the bonds of a fuel molecule, and this energy is liberated through interaction with other reactants including molecular oxygen or radical species with unpaired electrons. Inherently, this thermal energy is associated with molecular motion and molecular collisions, which for gases are typically in random directions and orientations, respectively (Vincenti and Kruger, 1967). However efficient it would be for the chemical energy in the bonds of a fuel molecule to convert into molecular motion in the exact direction

necessary for maximum useful work, it is a highly ordered (and improbable) configuration of the gases in the cylinder. This concept, a consequence of the second law of thermodynamics, constrains the maximum possible efficiency of heat engines (Kittel and Kroemer, 1980). The *internal combustion engine* is an example of a heat engine, and this term is often applied to engines which generate the heat inside the piston-cylinder assembly rather than outside it.

Energy equivalence

In the mid-1800s, as the steamships and steam locomotives of the industrial revolution changed human life, scientists and engineers made the connection that mechanical energy (in the form of work) and thermal energy (in the form of heat) can be converted to one another (Smith, 2003). Furthermore, *changes* in thermal energy, $đQ$, are equivalent to changes in mechanical energy, $đW_M$. Concurrently, the development of electric lighting and electric motors accompanied the realization that there is an equivalence between changes in electrical energy, $đW_E$ and changes in thermal energy and also between changes in electrical energy and changes in mechanical energy, respectively. A formalized mathematical expression for this concept, additionally including changes in chemical energy $đW_C$, is expressed in Equation 1.1 (Callen, 1985).

$$dU = đQ + đW_M + đW_E + đW_C \tag{1.1}$$

In Equation 1.1, U is the total internal energy of a system. If the system is *closed*, then U is constant, so $dU = 0$, and positive changes in any of the remaining terms on the right hand side must be balanced by negative changes in one or more of the other terms. This is a form of the first law of thermodynamics. This energy-conversion concept by itself was not necessarily new, but the notion that energy was *conserved* as it was converted from one form to another was profoundly consequential. The concept of energy efficiency and methods to calculate it were effectively established, and maximum bounds on the theoretical efficiencies of different (idealized) thermodynamic cycles could be determined. These cycles could be compared, and engineers could make informed decisions about how to best design an efficient heat engine.

The Otto Cycle

In the early 1800s, the earliest internal combustion engines often used combustion of "coal-gas" / "illuminating gas" (a mixture of carbon monoxide, CO, and hydrogen, H_2, produced from coal and often supplied to cities for gas lamp illumination) or vaporized distilled spirits principally to expand a gas in a piston-cylinder assembly; the cooling gases would subsequently create a vacuum and the atmospheric pressure outside of the cylinder would push the piston to its original position to generate work. By the mid-1800s, slightly better ignition control (either with a clever pilot lighting system or a primitive electrical discharge) gave rise to a *power stroke*, wherein work was produced during combustion. However, no

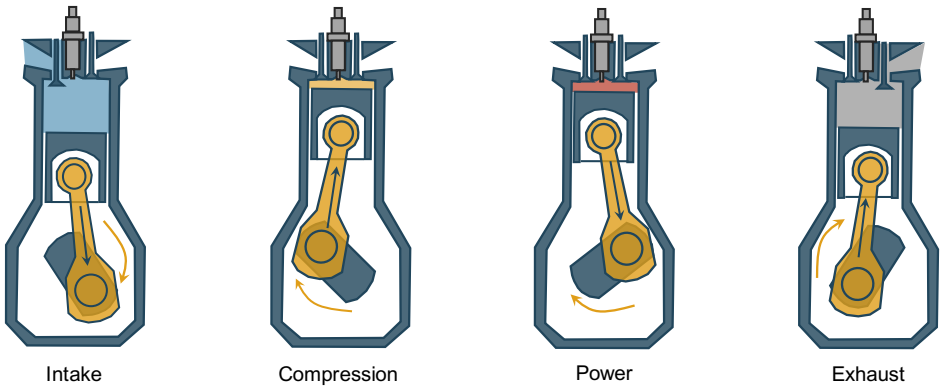

Figure 1.1: Diagram of the four strokes of the four stroke Otto cycle, adapted from Seinfeld (1975). From left to right: Intake, compression, power, exhaust.

compression took place prior to combustion, limiting the amount of useful power for a given engine size (Cummins, 1976).

In the 1870s, the four-stroke cycle—in which the fuel-air charge was compressed before ignition—came into fruition. A basic overview of thermodynamics is necessary to understand the advantages of compression prior to ignition in these early internal combustion engines. Dimensional analysis reveals that the unit of pressure is equivalent to energy per unit volume, so pressure multiplied by volume yields energy, or—in the case of changing volume—mechanical work. This relationship is shown in Equation 1.2 (Callen, 1985):

$$W_M = \int_{V_A}^{V_B} đW_M = -\int_{V_A}^{V_B} P \cdot dV \tag{1.2}$$

Thus, for a given system we are principally concerned with the relationship between pressure and volume, $P = f(V)$, because that relationship reveals how to extract the maximum amount of work possible for a prescribed heat addition to the system. One such possible relationship is that of *isentropic* compression and expansion—that is, compression and expansion without heat losses through the cylinder walls or heat gains from frictional processes. An informal walkthrough of an idealized four-stroke cycle assuming isentropic compression and expansion follows. This is a "cold air-standard" cycle (Moran and Shapiro, 2000): we assume that the gas in the cylinder has the properties of air at room temperature and that these properties are constant throughout the cycle. A diagram is shown in Figure 1.1. During the *intake stroke*, the piston moves to increase the volume in the cylinder, drawing in a fuel-air charge from an open intake valve. As the volume expands to its maximum, the intake valve shuts, and the piston subsequently changes direction to compress the fuel-air charge in the cylinder, which is now sealed. As the volume decreases during this *compression stroke*, the pressure in the chamber increases isentropically, and the piston is doing work on the gas. When the volume is compressed to its minimum, a large amount of heat is added to the chamber through the ignition of the fuel-air charge. In Equation 1.1, an interplay between

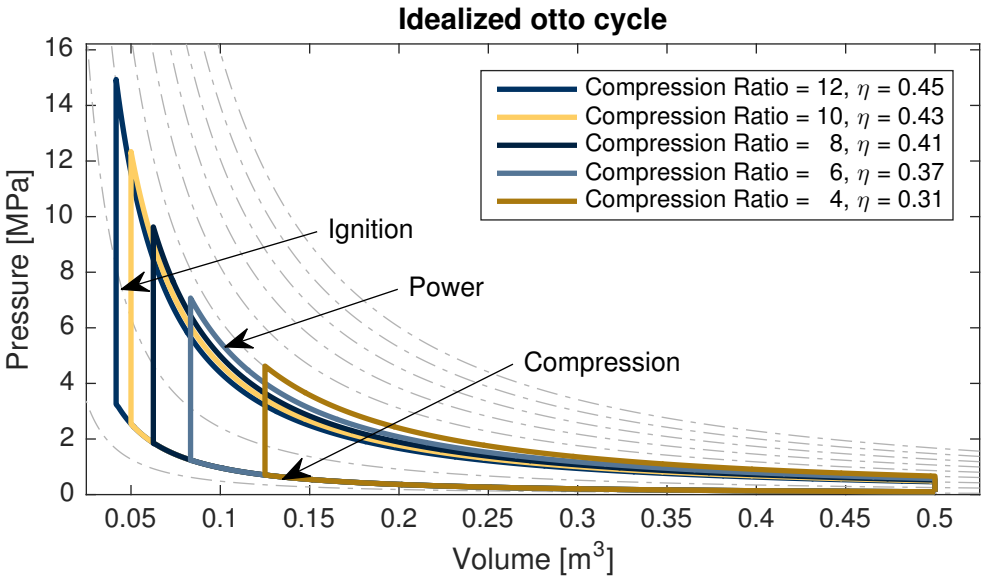

Figure 1.2: Simulated cold air standard Otto cycle curves with a constant amount of heat addition for different compression ratios. Only the compression and power strokes are shown here for clarity. The code to generate this plot is given in Appendix A.

$đQ$ and $đW_C$ corresponds to the conversion of the chemical energy stored in the fuel into heat and chemical products (mostly water, H_2O, and carbon dioxide, CO_2, but others are discussed later). This heat addition rapidly increases the temperature and pressure in the cylinder, and the gas pushes against the piston to expand the volume in the chamber during the *power stroke*. Now, the isentropically expanding gas is doing work on the piston. As the volume again approaches its maximum, the exhaust valve opens, allowing the combustion gases to escape the cylinder. This difference in minimum and maximum volume during the expansion stroke is referred to as the *displacement* of the engine. The piston then changes direction and the volume decreases in the *exhaust stroke*, pushing the exhaust gases out of the chamber. The cycle starts over again with a new intake stroke. Because the pressures during the power stroke are higher than during compression stroke, the net amount of work produced by the heat engine is positive. This cycle is referred to as the Otto cycle, named after Nikolaus August Otto, who is primarily responsible for bringing the four-stoke cycle into popular use (Cummins, 1989).

A series of idealized Otto cycle pressure-volume (P-V) diagrams for a hypothetical engine is presented in Figure 1.2 for the compression and power strokes only. Each of the different solid curves starts in the same thermodynamic state—that is, each has the same initial temperature, pressure, and volume. Each has the same mass of working fluid and each receives the same amount of heat at the end of their respective compression strokes. The only difference between the different cycles is the amount of compression the gases undergo prior to heat addition (ignition). It can be seen clearly that the systems that undergo greater compression have a larger volume on the P-V diagram—they produce a greater amount of

work for a given heat addition. For ideal gases that are compressed or expanded in a chamber isentropically, a family of pressure changes exist for a given volume change. A set of isentropic dashed lines are overlaid in Figure 1.2. For increasing initial pressure, the pressure rise is steeper as the system is compressed. This divergence of isentropic pressure-volume curves is why more compression before ignition results higher efficiency. Heat addition for a compression ratio of 4 results in a pressure increase of approximately 4 MPa, but the same amount of heat addition for a compression ratio of 12 results in a pressure increase of approximately 11 MPa. This pressure acts on the piston over a larger volume change, producing more work for a given amount of heat, and this additional work output exceeds the additional initial work input required to compress the gas more. A more formal thermodynamic analysis (Moran and Shapiro, 2000) reveals that the efficiency of the Otto cycle—expressed in Equation 1.3 as work output divided by energy input—depends only on the compression ratio, r_c, and the ratio of specific heats of the working fluid, γ.

$$\eta = \frac{W_M}{Q_{fuel}} = 1 - \frac{1}{r_c^{\gamma-1}} \tag{1.3}$$

The higher the compression ratio, the more efficient the engine. Calculated efficiencies for the different hypothetical cycles considered are shown in the legend of Figure 1.2. From a more fundamental thermodynamic point of view, this happens because the increase in compression ratio results in a higher temperature mixture before heat addition. For a Carnot cycle (Carnot, 1897), the temperature of the high temperature reservoir, T_H, is a governing factor in the ideal thermodynamic efficiency η_{Carnot}, given in Equation 1.4.

$$\eta_{\text{Carnot}} = 1 - \frac{T_L}{T_H} \tag{1.4}$$

Greater compression results in greater T_H, which results in a greater thermal efficiency. Though neither the Carnot cycle nor the *idealized* Otto cycle is possible in practice, this concept places a fundamental bound on heat engine efficiency. The first Otto engine ran on coal-gas and was limited to low speeds, but most modern engines and reciprocating heat engine cycles resemble this cycle. For example, the Diesel cycle compresses only air, and injects fuel during the power stroke. For this reason, Diesel engines do not have the fuel-air auto-ignition problems discussed in the following section, and can have much higher compression ratios. The Diesel cycle is relevant for the heavy-duty automotive engine research, but is otherwise not discussed at length in this dissertation.

Combustion chemistry and engine knock

The advent of the four-stroke engine demonstrated significant promise for more efficient machinery to make factories and nations more productive. Early engines, however, were limited to the available fuels of the time. The idealized Otto cycle is not possible to realize in practice, primarily due to combustion chemistry, which changes significantly depending on the fuel. Early engines were highly sensitive to fuel quality, and many fuel-air mixtures could

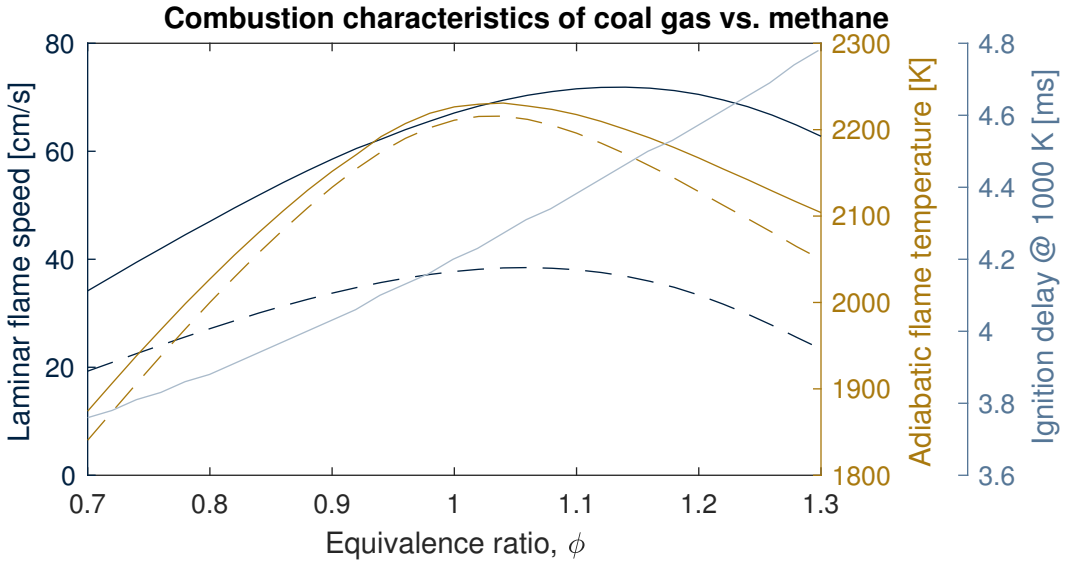

Figure 1.3: Plots of laminar flame speed (blue, left y-axis), adiabatic flame temperature (gold, right y-axis), and ignition delay (light blue, far right axis) for coal-gas (solid lines) and methane (dashed lines) as a function of equivalence ratio, obtained using CANTERA (Goodwin et al., 2014). Flame speed and flame temperature inlet conditions are specified as 300 K and 1 atm. Ignition delay initial conditions are specified as 1000 K and 1 atm. Ignition delay values for methane are not plotted because they are orders of magnitude larger than those of coal-gas. Coal-gas composition obtained from Scholte and Vaags (1959).

not be compressed beyond a certain compression ratio without uncontrolled explosive auto-ignition (henceforth colloquially known as *knocking*) (Cummins, 1989), limiting the efficiency of early engines. Knocking occurs when unburned regions of fuel and air in the cylinder auto-ignite before the flame front—initiated at the spark plug—can reach them. Each fuel-air mixture has both a characteristic *ignition delay time* and a *flame speed* depending on the fuel, the fuel-air ratio, temperature, and pressure. To illustrate, a diagram of computed flame speeds, flame temperatures, and ignition delay times for coal-gas as a function of molar fuel-air ratio is shown in Figure 1.3. In Figure 1.3, ϕ is the *equivalence ratio*, a non-dimensional expression for the molar fuel-air ratio, defined by:

$$\phi = \frac{n_{fuel,a}/n_{\mathrm{O}_2,a}}{n_{fuel,s}/n_{\mathrm{O}_2,s}} \tag{1.5}$$

The terms in the numerator, $n_{fuel,a}/n_{\mathrm{O}_2,a}$, represent the actual molar fuel-air ratio of a system, while the terms in the denominator, $n_{fuel,s}/n_{\mathrm{O}_2,s}$, represent the stoichiometric molar fuel-air ratio for a given fuel. For example, the stoichiometric reaction for methane, $\mathrm{CH_4}$, is:

$$\mathrm{CH_4} + 2\,\mathrm{O_2} \longrightarrow \mathrm{CO_2} + 2\,\mathrm{H_2O} \tag{1.6}$$

Thus, $n_{\mathrm{CH}_4,s}/n_{\mathrm{O}_2,s} = 1/2$. Values of ϕ that are larger than 1 are said to be *rich*, while values lower than 1 are said to be *lean*. In Figure 1.3, coal-gas and methane have similar flame

temperatures, but their flame speeds differ by about a factor of 2 and their ignition delay times differ by many orders of magnitude. Thus, combustion characteristics vary greatly with the fuel used, and engines must be designed for a specific range of these characteristics. The increased availability of liquid fuels with higher resistance to auto-ignition would enable both greater mobility and efficiency gains for society in the 20th century. However, several economic, technical, and sociological factors would shape the evolution of the internal combustion engine, all of which remain relevant today, guiding both current and future engine research.

Co-evolution of engines and fuels

An internal combustion engine ultimately transforms the chemical energy contained in fuel into mechanical energy to perform useful work, but the form of the fuel itself has a large impact on the feasibility of engine design. Prior to the large scale discovery of oil in the ground in the mid 19th century, most liquid fuels were derived from animal fats (e.g., whale oil) or from various plants (e.g., ethanol and turpentine) (National Research Council, 2011). Liquid fuels were relatively scarce and not competitive with other widely-available primary energy sources such as coal (Beaton, 1957). The large-scale discovery of oil in the ground and rapidly-developing crude oil refinement techniques of the time provided methods to control what kind of molecules could be extracted from the oil (Beaton, 1957).

At the dawn of the 20th century, the increased availability of liquid fuels enabled the mass production of automobiles, increasing demand for oil as a primary energy source (Beaton, 1957). However, the quality of the fuel was difficult to control, often causing engine knock and limiting compression ratios of production engines to around 4 (Splitter et al., 2016). Both World War I and the rapid increase in the number of automobiles in the United States increased the demand for gasoline, spurring both domestic and foreign oil exploration with significant success (Little, 2008). The advent of thermal cracking techniques enabled chemists to extract a greater amount of gasoline from a barrel of crude oil, and other separation techniques came into widespread use as government demand for specialized chemical feedstocks increased during the war (Beaton, 1957). These factors simultaneously increased the supply and purity of fuels available for use in engines. In the 1920s, researchers began to understand the relationship between fuel chemistry and engine knock (Ricardo, 1922), culminating in the controversial (Lewis, 1985) but successful introduction of tetra-ethyl lead (TEL) into gasoline (Amann, 1989; Splitter et al., 2016). As shown in Figure 1.4, the increased ability to resist engine knock enabled engine designs with higher compression ratios and therefore higher thermodynamic efficiency, as previously indicated in Equation 1.3. Shortly thereafter, a "quantifiable" measurement of fuel anti-knock tendency, the *octane rating*, was proposed (Edgar, 1927) and implemented in standardized tests and research engines (Pope and Murdock, 1932; Amann, 1989). In this metric—still in use today—a fuel blend exhibiting the same engine knocking behavior as a fuel comprising 100% iso-octane is given an octane rating of 100, while a fuel exhibiting the same knocking behavior as a fuel comprising 100% n-heptane is given an octane rating of 0 (Amann, 1989). Molecular

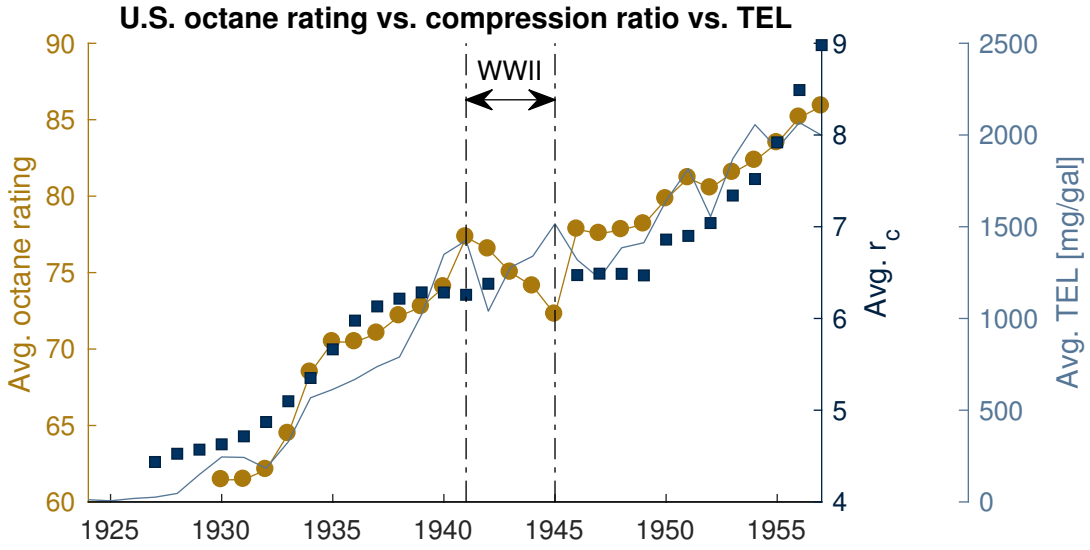

Figure 1.4: Plot of average octane number of U.S. gasoline (left axis) average engine compression ratio r_c of the U.S. automotive fleet (right axis) and average tetra-ethyl lead concentration in U.S. gasoline (far right axis) in the second quarter of the 20th century. Data sourced from Splitter et al. (2016). The drop in octane rating of available U.S. gasoline between 1941 and 1945 is due to high demand for high-octane aviation gasoline during World War II (Beaton, 1957). Likewise, there are no r_c data for engines during these years because no new automobiles were manufactured (Shelton et al., 1981).

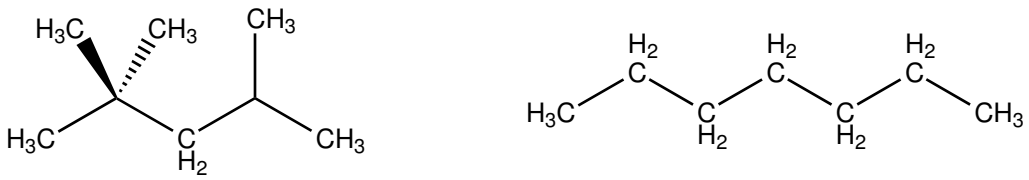

Figure 1.5: Species used in the development of the octane rating. Iso-octane (IUPAC name: 2,2,4-Trimethylpentane) (left), and n-heptane (right). The relationship between the structures of these molecules and their ignition characteristics is discussed in Chapter 2.

structures of these molecules are depicted in Figure 1.5. Thus, a fuel blend with an octane rating of 87 (widely available at the time of writing) exhibits the same knocking behavior as a blend of 87% iso-octane and 13% n-heptane, regardless of the actual iso-octane and n-heptane content in the fuel. These two molecules were chosen because iso-octane, though rare and expensive (roughly $360/gallon in 2017 USD), was one of the most knock-resistant hydrocarbons known at the time and high-purity n-heptane supplies were abundant. Inexpensive polymerization, alkylation, and isomerization techniques to synthesize iso-octane were soon discovered during the 1930s, dropping the price nearly 30-fold in the span of one year (to roughly $13/gallon in 2017 USD). Iso-octane was then blended with TEL other high-octane hydrocarbons produced from catalytic cracking to produce a relatively inexpensive ($3/gallon in 2017 USD) “100-octane” gasoline (Beaton, 1957).

These processes increased the average octane rating of gasoline, and, as shown in Figure 1.4, this greater abundance of cheap knock-resistant fuel coincided with the manufacture of engines with higher compression ratios (Splitter et al., 2016). Aviation engines with still higher compression ratios ($r_c \approx 8$) were also built in the mid-1930s, resulting in fuel savings of at least 15%, enabling the possibility of long-range aircraft (Beaton, 1957). These advances in engine efficiency were soon put to use: In World War II, the Allied effort consumed almost seven billion barrels of oil, and the United States supplied about 85% of it (Little, 2008), representing "more than a quarter of all the oil produced in America ... up to the beginning of 1941" (Beaton, 1957). Further wartime demands on aviation engine performance at a larger range of ϕ led to the increased synthesis and blending of aromatic hydrocarbons into gasoline, which remain a critical component of gasoline at the time of writing. After World War II, a combination of government interest in national energy security and corporate interest in market share enabled western oil firms to cooperatively extract more crude oil from the Middle East, further increasing the global supply of gasoline in the 1950s (Little, 2008). At the same time, the emerging plastics industry increased demand for more specific hydrocarbons (Beaton, 1957), coinciding with further innovations in the refining capabilities of the oil industry, such as catalytic cracking (Shelton et al., 1981). This sudden large supply of high quality fuel combined with favorable Western/Middle Eastern geopolitical climates kept the U.S. price of gasoline low in the following decade even as domestic oil production fell, and American automotive manufacturers produced bigger and more powerful cars to cater to consumer demand without significant regard to fuel efficiency (Shelton et al., 1981; Cooney and Yacobucci, 2007; Splitter et al., 2016). This often meant operating engines at rich ϕ, as shown in the left of Figure 1.6, since slightly rich combustion results in slightly higher flame temperatures and flame speeds, as indicated earlier in Figure 1.3.

Visible pollution and global competitiveness

Pollution becomes a problem

The rapidly increasing number of operating internal combustion engines—particularly in automobiles—reached a point where combustion products in the exhaust could no longer be ignored, particularly in regions bounded by topography keeping the pollution from dispersing (Shelton et al., 1981). In the 1940s, the air pollution plaguing the Los Angeles Basin in California was directly attributed to automotive exhaust (Seinfeld, 1975). The *smog* (a combination of the words "smoke" and "fog") was found to be generated by nitrogen oxides emitted from internal combustion engines and hydrocarbons reacting in the presence of ultraviolet light (as found in sunlight) to produce ground-level ozone (Haagen-Smit, 1952; Haagen-Smit et al., 1953) and was termed *photochemical smog*. The presence of hydrocarbons was (and still is) largely attributed to unburned hydrocarbons resulting from incomplete combustion of fuel in automotive engines, as well as evaporation of gasoline from fuel tanks and industrial emissions. The presence of nitrogen oxides, however, is due to the oxidation of nitrogen from air in small quantities into NO and NO_2 (collectively referred to as NO_X)

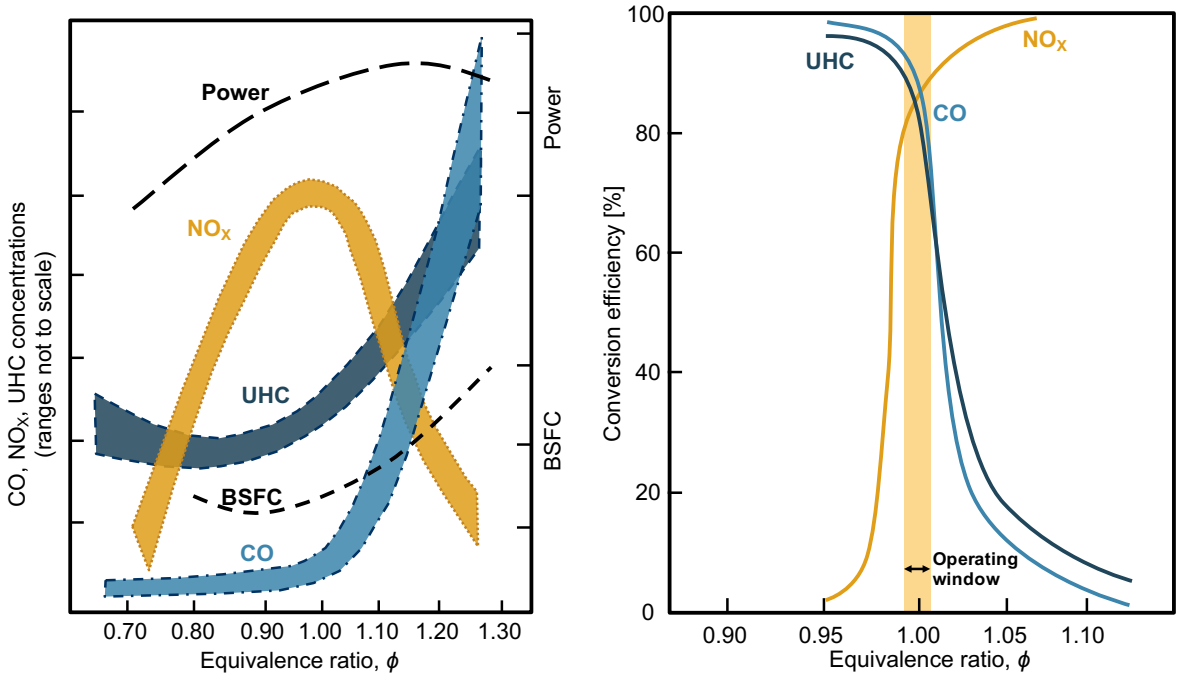

Figure 1.6: Typical engine-out emissions, brake-specific fuel consumption, and power output from an automobile as function of equivalence ratio adapted from Mondt (1989a) and Seinfeld (1975) (left), conversion efficiency of three-way catalytic converters for different pollutants as a function of equivalence ratio adapted from Mondt (1989b) (right).

in automotive engines (Seinfeld, 1975). The mechanism of this oxidation had concurrently been discovered by Zel'dovich (1946), who determined that the production rate of NO_X was exponential with temperature. Thus, the increased compression ratios of automotive engines had increased their efficiency, but at the expense of also increasing their peak in-cylinder temperatures and consequently their NO_X emissions. Photochemical smog was found to adversely affect ground-level visibility, vegetation, and the integrity of rubber tires. Adverse effects of smog on humans are primarily in the form of eye and lung irritation (National Research Council, 1977b), but other pollutants in automotive exhaust, such as CO from incomplete combustion, are more acutely dangerous and poisonous to humans than smog, and these hazards were well known at the time (Seinfeld, 1975). The impacts of combustion pollution on human health became a significant worldwide public concern.

Addressing pollution

In response to the mounting levels of pollution and evidence of impact on the environment and human health, California became the first U.S. state to enact requirements for emission control technology in automobiles in 1961, and action on the federal level came with the passage of the U.S. Clean Air Act of 1963 (with subsequent amendments in 1965, 1967,

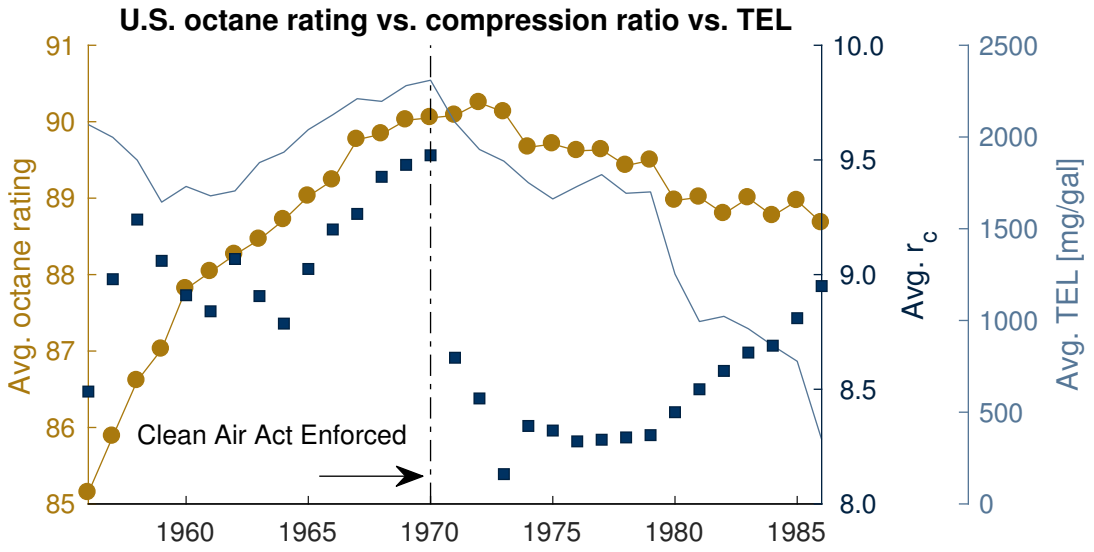

Figure 1.7: Plot of average octane number of U.S. gasoline (left axis) average engine compression ratio r_c of the U.S. automotive fleet (right axis) and average tetra-ethyl lead concentration in U.S. gasoline (far right axis) in the middle of the 20th century. Data sourced from Splitter et al. (2016).

1970, and 1977), directing automakers to begin reducing nitrogen oxides, carbon monoxide, and unburned hydrocarbons emitted from automobiles (Cooney and Yacobucci, 2007). As shown in the left of Figure 1.6, both the most fuel-efficient and the most powerful engine operation fuel-air ratios result in high NO_X emissions, rendering quick on-board solutions elusive.

As the U.S. Clean Air Act was enforced on a national scale in 1970, automobile manufacturers had no option except for substantially decreasing the compression ratio of their engines to meet tightening NO_X emissions standards (Splitter et al., 2016), as seen in Figure 1.7. In the 1970s, the oxidizing catalytic converter was developed and installed in many automobiles manufactured in the U.S. In this device, the engine exhaust mixes with fresh oxygen and passes through porous matrices of solid catalysts, facilitating the oxidation of CO and unburned hydrocarbons to CO_2 at lower temperatures in the exhaust. Leaded gasoline was detrimental to the lifetime of these catalytic converters, and so the average TEL content of gasoline began to decrease as unleaded gasoline became available (Lewis, 1985), and was eventually phased out completely by 1996 (Splitter et al., 2016). Unleaded gasoline required changes to fuel composition to increase its knock-resistance, but the reduced compression ratios of this period mitigated most adverse effects during the transition (National Research Council, 2011). Three-way catalytic converters were developed in the 1980s, allowing for the simultaneous reduction of NO_X and CO and HC emissions (Mondt, 1989b). As shown in Figure 1.7, compression ratios in new automotive engines gradually rebounded, giving cars more power while meeting the new emissions standards. However, as shown in the right of Figure 1.6, three-way catalytic converters are efficient in a very narrow operating range of equivalence ratios, limiting potential fuel economy gains that could be gained from overall

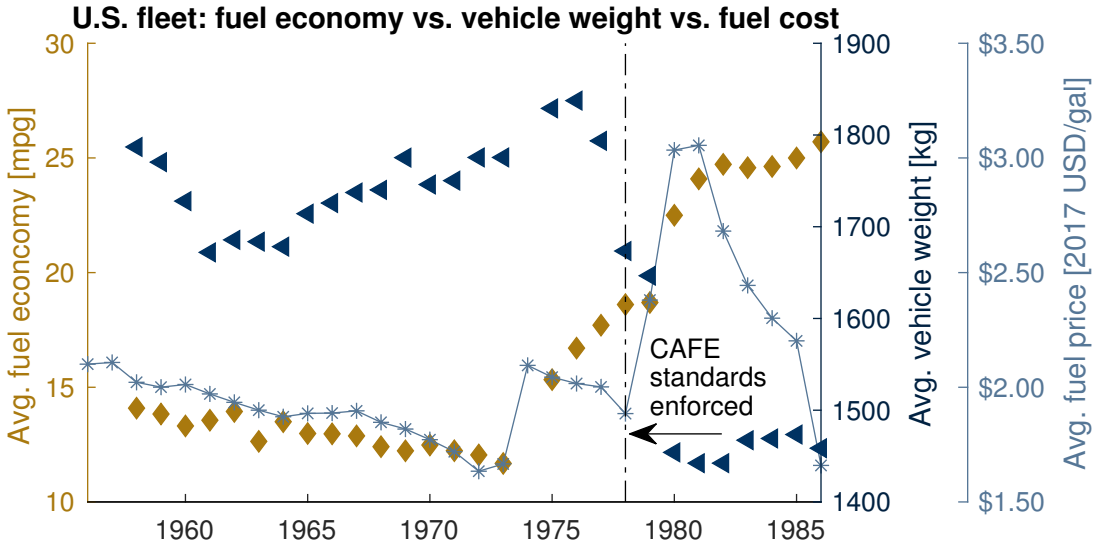

Figure 1.8: U.S. Fleet unadjusted fuel economy (left axis) and vehicle weight (right axis) sourced from Splitter et al. (2016), U.S. motor gasoline prices (far right axis) sourced from U.S. Energy Information Administration (2017) for the middle of the 20th century.

lean engine operation depicted in the left of Figure 1.6.

Energy security and fuel economy

Concurrently to these environmental concerns, matters of energy security became a problem for nations that had developed significant automotive infrastructure. In the 1960s, the relationship between the governments and oil firms of Western nations and the Middle Eastern nations soured. In 1973, the Arab Oil Embargo sharply reduced the available supply of gasoline for U.S. consumption, spurring an energy crisis (Little, 2008). U.S. automobile manufacturers, previously having a suite of cars that only made economic sense when gasoline was cheap, were unprepared for the sudden shift in market forces (Altshuler et al., 1984) as more fuel-efficient foreign cars began to enter the U.S. consumer market and erode the competitiveness of the U.S. automotive industry. In response, U.S. legislators passed The Energy Policy and Conservation Act of 1975, which established Corporate Average Fuel Economy (CAFE) standards for automobiles sold in the U.S (Cooney and Yacobucci, 2007). These standards mandated that automobile manufacturers sell a fleet of automobiles that meet a required average distance traveled per amount of fuel. As shown in Figure 1.8, an immediate fix on the part of automakers was to substantially decrease the weight of newly manufactured cars (Altshuler et al., 1984). An additional oil embargo in 1979 due to the Iranian Revolution caused more severe gasoline shortages and underscored the need for more efficient automobiles amid diplomatic uncertainty with oil-producing nations (Little, 2008).

Invisible pollution and anthropogenic climate change

In the initial phase of combustion emission regulation, much attention was focused on visible pollution which caused immediate consequences to the environment and human health. Internal combustion engines were prevalent enough to directly affect the environment on a regional scale, but it soon became apparent that their impact was global as well due to their generation of CO_2. As early as the 19th century, scientists postulated that increased levels of CO_2 in the atmosphere can increase the average surface temperature of the earth (Arrhenius, 1896). Throughout the 20th century, as temperature measurements for weather became more globally common, analyses revealed that the average temperature of the earth was steadily rising (National Research Council, 1977a). Measurements of ambient CO_2 began in the middle of the 20th century and, almost immediately, demonstrated that the concentration of ambient CO_2 was increasing steadily as well (Keeling, 1960). CO_2 absorbs energy strongly in the infrared spectrum of light due to its electronic structure (McQuarrie and Simon, 1997), and around this time was being considered partially responsible for the measured high surface temperatures of the planet Venus (Sagan, 1961). Most importantly, this range of wavelengths includes the long wavelengths associated with the thermal blackbody radiation of Earth (Seinfeld, 1975); thus, an increased concentration of CO_2 in the atmosphere has a physico-chemical basis for absorbing energy otherwise emitted into space. More sophisticated methods analyzing ice cores in Antarctica showed that, throughout the history of Earth, increased surface temperatures were associated with higher concentrations of CO_2 (Barnola et al., 1987). Though the consequences of higher Earth surface temperatures were not yet certain, it was apparent that combustion was influencing the global climate, causing concern among the research community (Pomerance, 1986).

1.2 The internal combustion engine today

Internal combustion engines, especially those in automobiles, have made tremendous advances in emissions reductions and fuel efficiency gains in the last few decades, both in the U.S. and around the world. Between 1970 and 2002, annual CO, NO_X, and unburned hydrocarbon emissions from highway vehicles fell by 62%, 42%, and 73%, respectively (Cooney and Yacobucci, 2007), and the CAFE standards are estimated to have reduced fuel consumption by as much as one third from what it otherwise would have been (National Research Council, 2002). The reduction of NO_X, in particular, is largely a result of using three-way catalytic converters in conjunction with operating automotive engines with increased recirculation of exhaust gas into the intake stroke. Exhaust gas recirculation (EGR) in modern automotive engines increases the concentration of CO_2 in the fuel-air charge, reducing the ratio of specific heats (γ) of the mixture, which therefore lowers the peak in-cylinder temperature when undergoing isentropic compression. According to Equation 1.3, this decreases the thermodynamic efficiency of the cycle; however, in practice, increased EGR increases the ignition delay time and thus lowers the likelihood of engine knock, enabling higher compression ratios

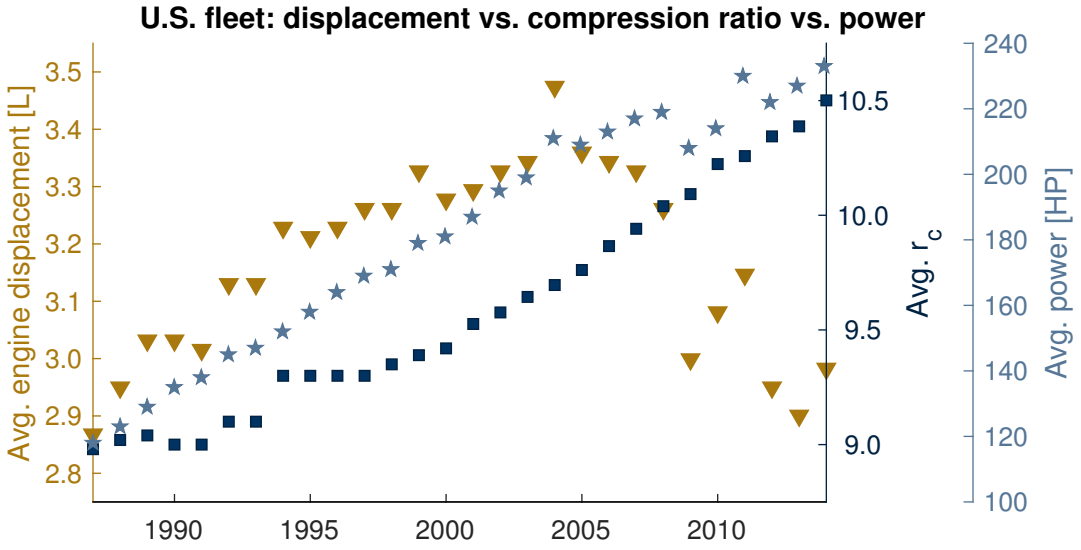

Figure 1.9: Plot of average displacement (left axis) average engine compression ratio r_c (right axis) and average power output of the U.S. automotive fleet (far right axis) in the last three decades. Data sourced from Splitter et al. (2016).

to compensate for any efficiency losses (Hoepke et al., 2012). Additionally, EGR gives any unburned fuel another chance to burn in the next engine cycle, increasing the amount of chemical energy converted into mechanical work in an engine (Heywood, 1988).

Current trends in engine designs

Since 2005, the average displacement of new engines in the U.S. automotive fleet has been getting smaller, reversing the trend of the 1990s and early 2000s. However, the average power output and compression ratio of these engines has been increasing, as shown in Figure 1.9. These trends also coincide with a stagnation in overall vehicle weight, shown in Figure 1.10. This is because spark ignition internal combustion engines are increasingly operating with boosted intake pressures in order to maintain power output while simultaneously reducing engine size and weight (Osborne et al., 2014; Turner et al., 2014). The introduction of technologies such as variable valve timing, direct-injection of fuel, cylinder deactivation, and continuously variable transmissions have all contributed to increased efficiency and reduced emissions (Splitter et al., 2016). Direct-injection of gasoline, in particular, has facilitated a substantial (about +1.0) compression ratio increase due to charge cooling effects resulting from evaporation of fuel in the cylinder (National Research Council, 2011).

Current energy, health, and environmental concerns

Clearly, there has historically been a myriad of interconnected sociological motivations influencing the development and use of internal combustion engine technology. These motivations

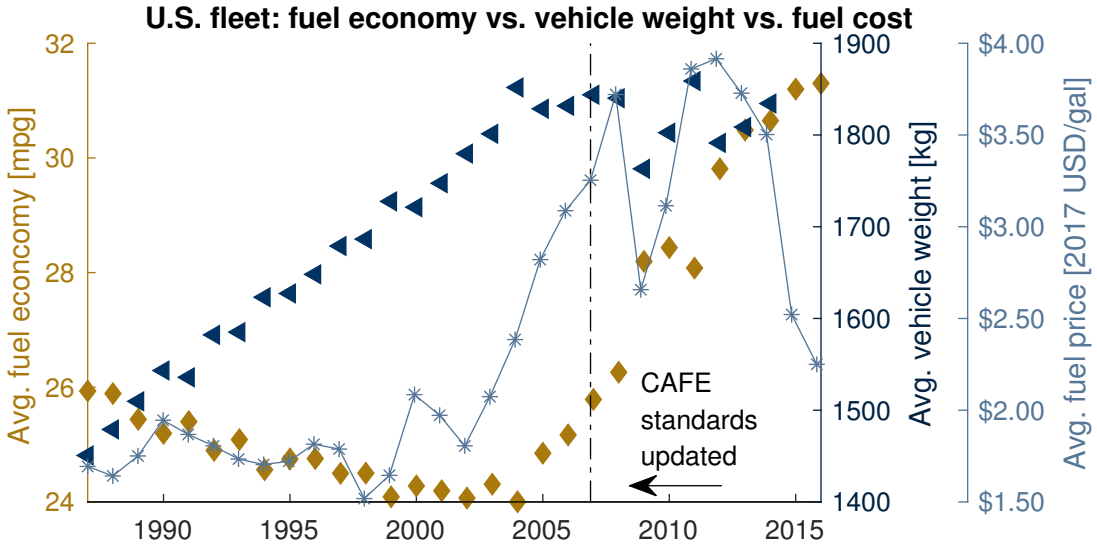

Figure 1.10: U.S. Fleet unadjusted fuel economy (left axis) and vehicle weight (right axis) up to 2014 sourced from Splitter et al. (2016), unadjusted fuel economy after 2014 sourced from Sivak and Schoettle (2017), U.S. motor gasoline prices (far right axis) sourced from U.S. Energy Information Administration (2017).

include improving the quality of human life responsibly, increasing the economic productivity of a nation, maintaining an advantage in geopolitical conflicts, and many others. These fundamental motivations have not significantly changed and are not likely to change in the foreseeable future. These issues are far beyond the scope of the research presented in this dissertation, but they nonetheless drive the motivation for the research and guide us to most intelligently solve the problems at hand.

Energy security in the United States

The aforementioned energy crises of the past are memorably stark motivations to increase energy security in the U.S, and all over the world. As of 2007, transportation represented 25% of annual U.S. energy demand, and about 60% of that energy was consumed by passenger cars. Additionally, all highway vehicles accounted for more than 75% of the energy used specifically for transportation, representing about 21% of all U.S. energy consumption (Cooney and Yacobucci, 2007). Thus, any significant fuel efficiency gains in automotive engines have the potential to reduce U.S. carbon emissions substantially and provide immediate benefits for people in the forms of fuel savings and less pollution, with longer term benefits such as reduced economic dependence on oil imports. The Energy Independence and Security Act of 2007 established CAFE standards of 35 miles per gallon (mpg) by 2020, a milestone that is currently on track to be met, as shown in Figure 1.10. This law also established the Renewable Fuel Standard (RFS), requiring an increasing share of biofuels in the gasoline supply, which has so far been accomplished with ethanol derived from corn (Schnepf and Yacobucci, 2013). More recently proposed updates to the CAFE standards for passen-

ger cars to achieve 54.5 mpg have been predicted to save about 4 billion barrels of oil and reduce greenhouse gas emissions by about 1.8 billion metric tons over the lifetimes of vehicles produced in Model Years 2017–2025 (U.S. EPA and U.S. NHTSA, 2012). However, at the time of writing, the enforcement of these proposed rules is in political contention, though the ability of manufacturers to effectively meet these requirements using emerging spark ignition engine technologies has been shown to be feasible (National Research Council, 2015). In general, recently tumultuous political climates in many nations render fuel economy regulations unreliable motivators for fuel efficiency research: Historically, when gasoline has been inexpensive, consumers have tended to purchase larger, less fuel-efficient vehicles, and automobile manufacturers have catered to consumer demand (National Research Council, 2011). This is reflected in Figure 1.8 for the years 1956–1972 and Figure 1.10 for the years 1990–2004 (Splitter et al., 2016). At the time of writing, crude oil prices have been low relative to historical values (U.S. Energy Information Administration, 2017), and so research into increasing the energy efficiency of automotive engines is absolutely necessary to increase future U.S. energy security and curb net CO_2 emissions.

Human health

Levels of pollution in any given region are controlled by three main factors: 1) how much pollution a device creates, 2) how many devices are concentrated in the region, and 3) how quickly the environment disperses the pollution (Seinfeld, 1975). Although many of the developed economies of the world have largely imposed appropriate regulations on combustion emissions, many developing economies are rapidly expanding as automobiles become more globally prevalent, and local regulations have not kept pace with the subsequent levels of pollution. Many regions, like the Los Angeles Basin, have a unique combination of weather, topography, and concentration of polluting devices that leads to unprecedented consequences on human health. Soot from combustion processes contributes to increased levels of particulate matter in the environment, which is associated with increased mortality in the population living nearby (Dockery et al., 1993). Highway vehicles in 2001 accounted for more than half of all CO emissions and roughly one third of all NO_X emissions and hydrocarbon emissions (Cooney and Yacobucci, 2007) in the U.S., representing a large target for emissions reductions that can positively impact human health.

Environmental policies put in place a few decades ago have already resulted in societal benefits. Lead, which can lead to severe neurological damage in humans (National Research Council, 1972), has been phased out of gasoline in the U.S. (Lewis, 1985), and in the years since its peak concentration in the environment, associated decreases with violent crime have been observed (Nevin, 2000). In the Los Angeles Basin alone, reducing harmful emissions has already had a measurably positive impact on human health: recent improvements in lung function for children are associated with declining levels of nitrogen dioxide and particulate matter (Gauderman et al., 2015), and statistically significant decreases in bronchitic symptoms have been observed as well (Berhane et al., 2016). Simply increasing the efficiency of combustion processes will reduce the overall levels of harmful emissions and is thus

a necessary subject of research.

Of course, regulations are only so good as they are enforced. Recent revelations of some automakers installing "defeat devices" on their emissions control systems have spurred investigations that have determined that some models of automobiles emit far more NO_X in real world driving conditions than stated (U.K. Department for Transport, 2016), particularly for automobiles with diesel engines, whose higher compression ratios inevitably result in high in-cylinder temperatures and high NO_X production. In Europe, substantial emissions reductions have occurred over the last few decades, but emissions of NO_X remain relatively high in countries in which diesel engines are widely used (Guerreiro et al., 2016).

Environment

As mentioned, it has been recognized for many decades that fossil fuel emissions—including CO_2—not only have the potential to contribute to global climate change, but are already doing so. It is the broad scientific consensus that human activities are driving observed climate change (Cook et al., 2013) and that average global temperatures will not stabilize if humans continue to emit CO_2 at current rates (IPCC, 2013). Natural variation in Earth's climate (Karl et al., 2015) and solar activity (Lockwood, 2008) have been definitively ruled out as alternative explanations for the temperature increases. The resulting climactic change has already impacted all geographical areas of the U.S. and will continue to intensify in the next few decades (Melillo et al., 2014). Expected impacts include rising sea levels, decreasing crop yields, and increasing geopolitical turmoil (IPCC, 2013). Mitigating these impacts will require substantial reductions in CO_2 emissions from fossil fuels (Pacala and Socolow, 2004).

In 2010, transportation related energy use was responsible for approximately 23% of global energy-related CO_2 emissions (Sims et al., 2014). In the U.S., this number was 25% in 2014, with light-duty vehicles accounting for about 17% of total net U.S. greenhouse gas emissions (National Research Council, 2013; U.S. Environmental Protection Agency, 2016). These percentages align with the overall energy consumption mentioned previously, highlighting the current dependence of the U.S. energy infrastructure on carbon-based fuels: As of the end of 2016, U.S. CO_2 emissions from the transport sector are greater than those of any other sector, including power generation (U.S. Energy Information Administration, 2017). Thus, the transportation sector represents a significant target for CO_2 emissions reductions, and research improvements to internal combustion engines will play a large role in these reductions. For example, in the U.S., increasing the current overall fleet average to 31 mpg would reduce CO_2 emissions more than several other individual measures combined, such as driving 1.2% less, reducing food and meat consumption by 2% and 7%, or flying 10% less (Sivak and Schoettle, 2016).

1.3 The future of the internal combustion engine

Though transitions to less carbon-intensive transportation and energy generation systems are required to mitigate the worst impacts of anthropogenic climate change (IPCC, 2013), economic and technical challenges limit large and rapid changes in energy infrastructure. These technical and economic challenges are briefly discussed here in the context of the transport sector, and a constrained set of solutions is presented.

Decarbonization of transport: Technical challenges

In a carbon-constrained world, the transition to less carbon intensive energy sources will not happen quickly and is not immediately feasible for all current energy requirements. Holistic strategies to reduce the carbon intensity of transportation—such as increased public transportation in cities to displace personal automobile travel and development of high-speed rail to displace intercity air travel—require years of urban planning and decades to implement (Sims et al., 2014). Such strategies are needed, but even in the near term, decarbonizing the transport sector is still daunting. In particular, high energy density is an indispensable feature of liquid fuels in transportation (Reitz, 2013), and will constrain near-term solutions to more efficient internal combustion engines (National Research Council, 2013).

Alternatives to heat engines

As discussed in Section 1.1, heat engines suffer from thermodynamic limitations associated with the second law of thermodynamics. Other propulsion technologies for automotive transport are under considerable research and development, but their large-scale implementation is still decades away. Electric motors have a significant advantage over heat engines in that the electrical energy-to-mechanical work efficiencies are typically much higher than those of even the most efficient heat engines (National Research Council, 2013). Two imminent technological pathways utilizing electric motors, storing energy in electric batteries and/or fuel cells, both show promise but have unique setbacks for near-term mass implementation. A Ragone plot (Ragone, 1968) comparing both the energy density and the power density of various propulsion systems for automobiles is presented in Figure 1.11.

Electro-chemical battery technology for all-electric-powered vehicles has advanced in recent years (National Research Council, 2011), but the energy density and replenish rate of rechargeable lithium-ion batteries—the imminent battery technology of the near future—remains low relative to liquid fuels (Ghoniem, 2011). Research to increase this energy density is ongoing, but this technical setback restricts all-electric vehicle power and range to light-duty urban driving in the near term (Reitz, 2013; Sims et al., 2014). Hydrogen (H_2) fuel cell technology for vehicles has also advanced, and does not have the energy density and replenishing rate problems associated with batteries, as indicated in Figure 1.11. However, infrastructure barriers for H_2-powered vehicles will remain for at least the next decade; there

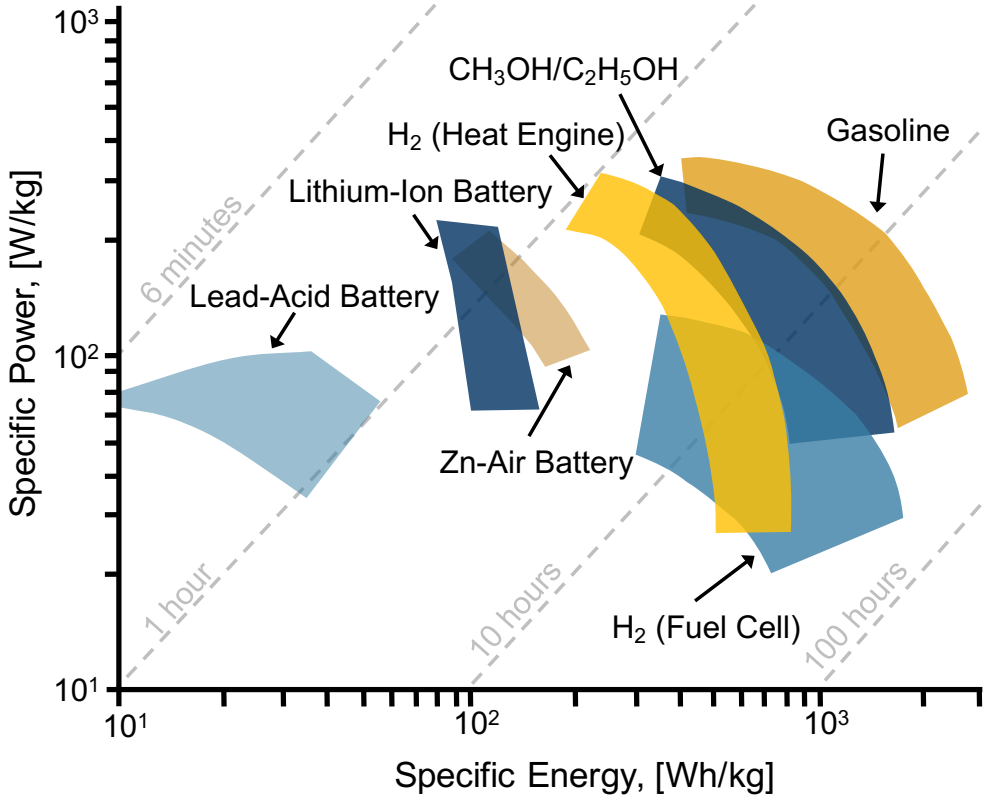

Figure 1.11: Ragone diagram (Ragone, 1968) comparing the energy density (in Wh/kg) and the specific power (in W/kg) of different propulsion technologies for automobiles, adapted from Ghoniem (2011). Diagonal lines indicate expected propulsion lifetime. Note that while power delivery and energy storage among H_2 fuel cells and heat engines powered by methanol/ethanol (CH_3OH/C_3H_5OH) and gasoline are similar, electrochemical batteries lag in energy density and thus have limited propulsion lifetimes.

are simply not enough refueling stations that service H_2-powered vehicles outside of large metropolitan areas (Schoettle and Sivak, 2016). These necessary infrastructure changes are themselves contingent upon adoption rates of vehicles that have the technology (National Research Council, 2013). More importantly, the storage of gaseous H_2 is difficult; because of its low molecular weight, it must be compressed to high pressures in order to provide for vehicle range comparable to that of current liquid-fuel powered automobiles. Additionally, its high diffusivity renders leaks a significant concern in transporting the fuel (Ball and Wietschel, 2009). A combination of lithium-ion battery and H_2 fuel cell technologies is expected to take advantage of the best of each technology to reduce overall dependence on liquid fuels in the far-term (20–30 years) (National Research Council, 2013), and research and development on each of the technologies will synergistically facilitate mutual benefits for the implementation of both.

Alternatives to liquid fuels

For many years, molecular H_2 has been investigated for use in automotive engines as a combustible gaseous fuel, because it contains no carbon and can, with some effort, be reproduced from renewable energy (U.S. DRIVE, 2013). Additionally, as indicated in Figure 1.11, an H_2 heat engine can deliver power comparable to a gasoline engine. As discussed early in Section 1.1, the earliest internal combustion engines ran on a fuel largely comprising H_2 gas, so this concept is not without precedent. However, all of the infrastructure and storage problems that currently afflict H_2 fuel cells also apply to H_2-fueled heat engines. Therefore, research and development on the infrastructure necessary for the storage and transport of H_2 will benefit both fuel-cell powered vehicles and H_2 heat engine vehicles.

Compressed natural-gas (CNG) powered vehicles offer greater energy security in countries with abundant natural gas supplies (Ball and Wietschel, 2009). They do not suffer from the same infrastructure problems as does H_2, since natural gas lines already exist for home and commercial heating in many developed countries and is typically not as dangerous to handle, though compression facilities to refuel automobiles are still sparse (National Research Council, 2013). However, in terms of greenhouse gas emissions, CNG vehicles will provide few benefits beyond reduced harmful engine-out emissions (e.g. CO, unburned hydrocarbons, soot), because they still burn fossil fuels, emit CO_2, and will largely compete with all-electric vehicles rather than liquid fuel-powered automobiles (Peterson et al., 2014).

Next-generation liquid fuels

As demonstrated nearly a century ago (Figure 1.4), an opportunity exists to once again improve the performance of engines by improving the quality of the fuel, either refined from petroleum or from carbon-neutral sources such as plants. The aforementioned negative repercussions of leaded gasoline, discussed in Section 1.1, must be kept in mind throughout this process, and any substantial efficiency gains must be weighed cautiously against any negative public health impacts. The use of more carbon-neutral fuels is already underway, in part because of the RFS, which has introduced ethanol distilled from corn into the U.S. gasoline supply (Schnepf and Yacobucci, 2013). Additionally, nations such as Brazil already have high bio-derived ethanol blends of fuel in their automotive energy supply, though the implementation there is easier due to the large availability of sugarcane in the country (National Research Council, 2013). The addition of ethanol, C_2H_5OH, boosts the octane rating of gasoline (Vuilleumier, 2016; Barraza-Botet et al., 2016), and its high-evaporative cooling characteristics allow for increased compression ratios when direct-injected into engines (Vuilleumier, 2016). However, as seen in Figure 1.11, ethanol has a lower energy density than gasoline, and so the effect is not readily apparent since most engines are still designed and manufactured with compression ratios corresponding to gasoline (National Research Council, 2011). Additionally, the oxygen atom present in C_2H_5OH facilitates the oxidation of fuel, reducing CO and unburned hydrocarbon emissions (Stein et al., 2013). Bio-derived drop-in-replacement fuels such as corn ethanol can offset petroleum-derived fuels, but land-

use changes associated with growing the crop for fuel instead of food raise significant ongoing ethical concerns (Tilman et al., 2009). While not the focus of this dissertation, research into bio-derived octane-boosting additives that are more land-use friendly than ethanol is ongoing (Westbrook et al., 2011; Ren et al., 2014; Bohon et al., 2017; Dames et al., 2015; Vallinayagam et al., 2017), and will play a significant role in reducing the carbon intensity of transportation in the near and far term.

Next-generation internal combustion engines

The success of the three-way catalytic converter has restricted the operation of automotive engines to near-stoichiometric fuel-air ratios in practice (as shown in the right of Figure 1.6), and lean-burn emissions aftertreatment systems that can fit in small automobiles remains a challenge (National Research Council, 2013; Stanton, 2013). Thus, the principal method of reducing peak in-cylinder temperatures and subsequently NO_X emissions in recent years has been to increase the amount of exhaust gas recirculated into the intake of the engines, rather than operating engines in low-temperature lean-combustion modes. Lean-burn engines have been a subject of significant research and development over the last decade, but the imminent technologies, such as Homogeneous Charge Compression Ignition (HCCI), suffer from combustion instability at high loads that is unacceptable for production automobiles (National Research Council, 2015). This is because these engines are controlled entirely by the reactivity of the fuel-air mixture rather than with a spark or injection event as is the case with spark-ignition and compression-ignition engines, respectively. Though recent progress has been made in HCCI engines (Vuilleumier et al., 2016), including increased understanding of expanded load limits using partial fuel stratification (Wolk and Chen, 2014; Wolk et al., 2015) and multiple-injection strategies (Kolodziej et al., 2014), HCCI is not presently considered a technology that will be on the road within the next 15 years (National Research Council, 2011).

Decarbonization of transport: Economic challenges

From the previously discussed technical challenges, it is clear that liquid-fuel powered automobiles are going to be part of daily life for the next several decades, in both the U.S. and in emerging economies around the globe (National Research Council, 2015). In 2004, the total economy of the automotive industry in the U.S. was estimated to be approximately $503 billion (in 2017 U.S. dollars) (Cooney and Yacobucci, 2007). Currently, the industry provides a backbone of manufacturing in the U.S., and facilitates the transport of goods and services across the country in an increasingly-connected economy. For developing countries in which emissions regulations may still be emerging, such an industry is an attractive pursuit for establishing economic independence and growth. The roles of such energy infrastructures during WWII and the energy crises of 1973 and 1979 further highlight the attractiveness of energy security, presenting challenges for developing nations in scenarios in which fossil fuel-based transport is much less expensive in the short term than renewable alternatives.

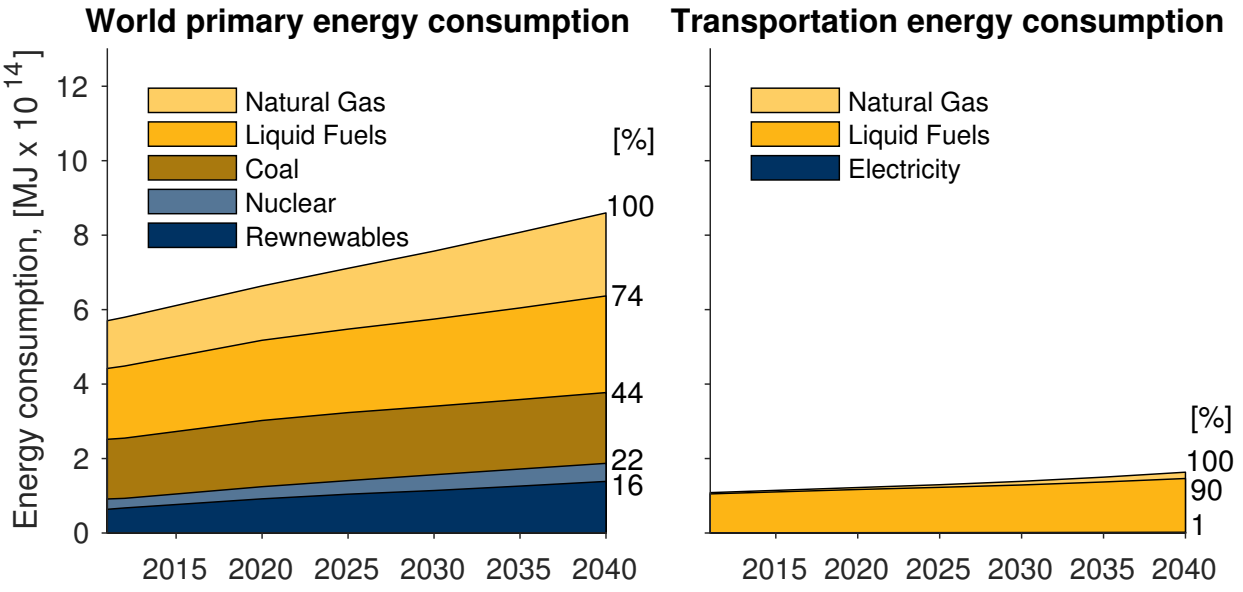

Figure 1.12: Total primary energy consumption by source (left) and total energy delivered in transportation by source (right), with projections to 2040 (U.S. Energy Information Administration, 2016). Y-axes are the same scale to demonstrate the role of transportation in overall energy demand.

Scholars estimate that there are significant global oil reserves remaining, and that as oil use in the heating and power generation sectors falls in favor of natural gas and renewable power, liquid fuels will increasingly be used solely for transportation (Altshuler et al., 1984), making up to 88% of the primary energy use for transportation by 2040 (U.S. Energy Information Administration, 2016), as shown in Figure 1.12.

Many of the aforementioned technical challenges generally have technical solutions, but existing solutions are often too expensive to implement in production automobiles. Lean-burn engine emissions aftertreatment systems—such as Selective Catalytic Reduction (SCR) and lean-NO_X traps—are currently only cost-effective for large, heavy-duty vehicles (National Research Council, 2010; U.S. DRIVE, 2013; National Research Council, 2015). CNG-powered vehicles, at the time of writing, are slightly more expensive to manufacture than liquid-fuel-powered automobiles (National Research Council, 2013). However, they are increasingly used in government and public transportation fleets (Sims et al., 2014), and this contributes to the projection estimate in Figure 1.12 that 10% of transportation energy will come from natural gas (U.S. Energy Information Administration, 2016). Long range (>200 mile) all-electric battery and fuel-cell powered vehicles are emerging, but at the time of writing are two to three times as costly as comparable gasoline powered automobiles without government subsidies, and so are not yet cost-competitive (National Research Council, 2013). Because of these technical and economic challenges, vehicles that still have an internal combustion engine—either as part of the drive train or as a range-extender for an electric motor—are expected to occupy 98% of the overall light-duty fleet through 2025 (National Research

Council, 2015) and are a significant factor in the energy consumption projections depicted in Figure 1.12 (U.S. Energy Information Administration, 2016). Pending significant advances in low-cost renewable transportation technologies or substantial government intervention, the availability of liquid fuels and the ubiquity of their infrastructures are likely to guarantee that automobiles will be, at root, powered by petroleum-based fuels for quite some time (National Research Council, 2013; U.S. Energy Information Administration, 2016). Thus, it is imperative to research and develop both carbon-neutral liquid fuels as well as technologies which markedly increase the energy conversion efficiency of liquid- and CNG-fueled automobiles.

Engine-specific solutions for immediate impact

Modest efficiency improvements of internal combustion engines in the short term can simultaneously reduce CO_2 emissions and increase energy security while alternative fuels and vehicles are developed for the long term. In fact, up to 15% of the emissions reductions necessary to stabilize greenhouse gas emissions can be met with fuel efficiency increases of existing automobile and power generation infrastructure (Pacala and Socolow, 2004). Policies which provide incentives to engine manufacturers for increased fuel efficiency and emissions reductions will need to be pursued (Sims et al., 2014), albeit with caution. For example, diesel engines are more efficient due to their higher compression ratios, but unenforced emissions controls result in substantially increased NO_X emissions (U.K. Department for Transport, 2016). For light-duty vehicles, a few engine-specific strategies have been identified for near-term increases in fuel efficiency and emissions reductions (National Research Council, 2011; U.S. DRIVE, 2013; Reitz, 2013; National Research Council, 2015):

- *Downsizing and boosting*: *Downsizing* an engine—that is, reducing its displacement—reduces frictional losses and lowers the overall weight of the engine, which can contribute to some fuel economy gains. However, the reduced displacement generally corresponds with a loss in maximum power output, and—while beneficial to low-load operation—is undesirable for high-load operation. This power loss can be offset by *boosting* the intake pressure via a turbo- or super-charger ahead of the intake manifold, effectively increasing the power-to-weight ratio of the engine. It is important to note that even though this process does not change the volumetric compression ratio of the engine, it does increase the maximum pressures and temperatures in the cylinder, which will increase engine-out NO_X emissions and the likelihood of engine knock.

- *Stoichiometric gasoline direct injection*: Applying direct-injection strategies to spark-ignition engines allows for increased compression ratios (and hence, increased efficiency as per Equation 1.3) due to charge cooling. Overall stoichiometry of combustion will remain at $\phi = 1$ so that existing three-way catalytic converter technology will continue to eliminate engine-out pollutants at maximum possible efficiency (Figure 1.6).

- *Increased Exhaust Gas Recirculation*: Further diluting the fuel air charge with more EGR in the boosted, higher-compression ratio SI engines of the future will reduce

engine-out NO_X emissions and increase the ignition delay time of the fuel-air mixture, which lowers the likelihood of engine knock. However, increased EGR lowers flame speeds, which increases the duration of the combustion event in the cylinder and can result in unreliable ignition and unstable engine operation.

- *Reduced combustion duration*: Reducing the combustion duration with strategies such as increasing the turbulent mixing in the cylinder or enhanced ignition strategies will mitigate the aforementioned stability problems associated with high-dilution combustion. Additionally, these strategies also apply to lean-burn engines and will facilitate their deployment once suitable aftertreatment strategies are developed.

- *Increased hybridization*: Over the next 10–15 years, hybrid vehicles will increase their presence and their costs will come down. In hybrid vehicles, the SI engines are often downsized and operate most often at loads and speeds that correspond to their peak efficiencies. All of the aforementioned strategies outlined here will increase the efficiency of these hybrid vehicles and further reduce overall CO_2 emissions in the process.

This dissertation specifically focuses on simultaneously advancing three of these five thrusts: reduced combustion duration in high dilution and boosted conditions. By advancing these three fronts, this research accomplishes the goals of increasing fuel efficiency and reducing harmful emissions, with particular attention to implementation of these conclusions within 10–15 years in production automobiles.

1.4 Advanced ignition to reduce combustion duration

For spark ignition engines, the time it takes for an initial flame kernel to develop into a rapidly burning flame is often greater than 25% of the entire combustion duration (Heywood, 1988). During lean or high EGR operation, more ignition energy is often necessary to overcome heat losses to the spark plug electrodes, and these flames develop more slowly than in undiluted operation (Pischinger and Heywood, 1991). More detailed explanations of these limiting combustion phenomena are presented in Chapter 2. Various technologies have been proposed over the last 30 years to address these problems, including multiple spark plugs per cylinder, longer duration sparks, plasma jet ignitors, rail plugs, lasers, and others, with mixed success (Dale et al., 1997). None of these techniques have been implemented in production engines, and, as mentioned, recent fuel economy gains in automobiles are largely attributed to several non-ignition technological enhancements (Splitter et al., 2016). The recent trend of downsizing and boosting spark ignition engines, however, has renewed interest and opportunity in advanced ignition techniques, especially since EGR can be intelligently used to mitigate engine knock at high loads (Lavoie et al., 2013).

As discussed in Chapter 2, traditional spark ignition is more difficult or impractical at high pressures—when the charge gas density increases, spark plug voltage and current must

also increase to arc in the denser gas, resulting in higher rates of electrode ablation. Decreasing the spark plug gap can mitigate the increased voltage/current requirements, but this has the effect of increasing heat losses to the developing flame kernel, which can increase the number of misfires and increase cycle-to-cycle variability to an unacceptable level (Pischinger and Heywood, 1991). Thus, traditional inductive spark ignition systems will face challenges in the downsized, boosted, high-dilution SI engines of the future, and advanced ignition strategies must be explored (Dale et al., 1997). Recently, some advanced ignition strategies for engines have progressed to the point where they demonstrate potential as drop-in replacements for existing spark ignition technologies, but they are still not well characterized enough for confident use in commercial automotive engines. These include microwave assisted spark ignition, corona discharge ignition, and pulsed nanosecond discharge ignition (Zheng and Yu, 2015; Tropina et al., 2016). The theories behind these techniques and their specific relevance to the ignition of fuel-air mixtures is the subject of Chapter 2.

Chapter 2

Plasma-Assisted Ignition: Theory and applications

This chapter provides a brief background on ignition chemistry of fuels, followed by a discussion of how both traditional and advanced ignition techniques exploit this chemistry. Specifically, a distinction between thermal (equilibrium) plasma and non-thermal (non-equilibrium) plasma is made, and a background for each is presented. Two advanced ignition techniques utilizing non-thermal plasma are singled out for further investigation. Finally, previous experiments in the literature which use advanced ignition techniques to extend the dilute limits of internal combustion engine operation are discussed and compared.

2.1 Oxidation of fuel-air mixtures

Combustion reactions are distinct from other exothermic chemical reactions because they are oxidative processes proceeding at relatively fast rates (reactions completing in ∼1–100 ms). In this context, "oxidation" refers to the combination and subsequent decomposition of fuel molecules ($C_\alpha H_\beta O_\gamma$) and oxygen molecules ($O_2$). A stoichiometric equation for such an overall reaction follows in Equation 2.1 (McAllister et al., 2011).

$$C_\alpha H_\beta O_\gamma + (\alpha + \beta/4 - \gamma/2)\, O_2 \longrightarrow \alpha CO_2 + (\beta/2)\, H_2O \tag{2.1}$$

Equation 1.6 in Chapter 1 is an example of Equation 2.1 applied to the fuel methane, CH_4. Though descriptive, Equation 2.1 gives no information on the rate of reaction, or how the reaction is affected by the presence of other species. Combustion reactions proceed in many intermediate steps not shown in Equation 2.1, each at different temperature- and pressure-dependent rates, and are henceforth referred to as *elementary* reactions. Collections of elementary reactions that describe an overall reaction such as in Equation 2.1 are referred to as *chemical kinetic mechanisms*. Importantly, these mechanisms include *chain reactions*, elementary reactions that depend on other elementary reactions in order to complete the reaction. A key class of chain reactions distinguishing combustion reactions from other

chemical reactions is that of radical *chain-branching* reactions, in which a chemical reaction that has a radical (a species with an unpaired electron) as one of the reactants produces products that include two or more radicals. Gas-phase reaction rates are, in general, proportional to the concentrations of each of N reactants and proportionately exponential with temperature T (Steinfeld et al., 1998), as in Equation 2.2.

$$\hat{r} \propto k_{rxn} \cdot \left(\prod_{i=1}^{N} [C_i] \right) \propto A \cdot \exp\left(\frac{E_a}{\hat{R}_u T} \right) \left(\prod_{i=1}^{N} [C_i] \right) \tag{2.2}$$

In Equation 2.2, $[C_i]$ are the concentrations of the reactants and k_{rxn} is the reaction rate coefficient, which has been expanded to show its dependence on A, E_a, and T. A is a coefficient often associated with the collision frequency of the gas molecules, E_a is the activation energy (in units of energy/mole) required to initiate the reaction, and $\hat{R}_u$ is the universal molar gas constant (in units of energy/mole/temperature). As exothermic *chain propagating* and *chain termination* reactions occur and increase the local T, all of the chain reactions proceed more rapidly, highlighting the explosive nature of combustion chemistry. A good review of the oxidation mechanisms of fuels is given by Law (2006), and a more recent review of the oxidation of alcohols is given by Sarathy et al. (2014). A brief discussion of the different classes of chain reactions follows, using CH_4 as an illustrative example fuel.

Chain initiation reactions

At low temperatures ($<\sim$400 K) and near-atmospheric pressures, a stoichiometric mixture of fuel and air usually does not react on short timescales ($<\sim$1 year) (McAllister et al., 2011), because the collisional energies of molecules are not high enough for *chain initiation* reactions to occur with sufficient frequency, such as the reactions in Equations 2.3 and 2.4 (Law, 2006).

$$CH_4 + M \longrightarrow \cdot CH_3 + \cdot H + M \tag{2.3}$$

$$O_2 + M \longrightarrow \cdot O + \cdot O + M \tag{2.4}$$

In Equations 2.3 and 2.4, the dots on species indicate unpaired electrons, and they are often termed *radical* species. M is *any* molecule that is involved in a collision but does not react, and so M could be, in this case, O_2, N_2, or even CH_4. In Equation 2.3, the energy from the collision is large enough to break a C−H bond in CH_4, creating $\cdot H$ and $\cdot CH_3$ radicals, and in Equation 2.4, the energy is large enough to break the O=O bond in O_2 to make two $\cdot O$ radicals. In general, the activation energy, E_a, required to break these bonds is often closely related to the strength of the bond (Law, 2006); the O=O double bond in O_2 has a bond energy of 494 kJ/mol (McQuarrie and Simon, 1997), while the C−H single bond in CH_4 has a bond energy of 439.3 kJ/mol (Anslyn and Dougherty, 2006). Thus, the radical-generating reaction in Equation 2.3 is more likely to happen than the radical-generating reaction in Equation 2.4 at a given temperature. These radicals are much more reactive than their parent molecules and will initiate subsequent reactions with other species.

Many reactions other than the ones depicted in Equations 2.3 and 2.4 are possible, and different chain initiation reactions will dominate depending on the temperature and pressure of the system (Law, 2006). The important point, however, is that for reactions like those in Equations 2.3 and 2.4 to occur, the molecules must have sufficient energy before colliding. In general, the molecules are more likely to have this energy at higher temperatures, and local high temperature regions are easily provided with spark plugs, as discussed in Section 2.3.

Chain branching reactions

Once radicals are present in a mixture, they can react with other molecules to generate additional radicals in chain branching reactions, like those in Equations 2.5 and 2.6. The products of these reactions greatly increase the overall reactivity of the mixture and contribute to the explosive nature of combustion reactions, and this is why chain branching reactions distinguish combustion from other kinds of exothermic chemical reactions.

$$\cdot H + O_2 \rightleftharpoons \cdot OH + \cdot O \tag{2.5}$$

The reaction in Equation 2.5 is often considered the most important reaction in combustion (Warnatz et al., 2006) and has a large influence on flame speed (Law, 2006; Pineda, Shi, Casey and Chen, 2017) because $\cdot OH$ and $\cdot O$ are both critical to other key reactions, such as the one in Equation 2.6.

$$CH_4 + \cdot O \rightleftharpoons \cdot CH_3 + \cdot OH \tag{2.6}$$

$\cdot O$ is particularly important in the breakdown of fuel molecules, such as in the hydrogen abstraction (H-abstraction) that takes place in Equation 2.6, which is itself also a chain branching reaction producing $\cdot OH$. As mentioned in Section 1.1, the structure of the fuel molecule plays a large role in its propensity to auto-ignition. This is because the molecular structure directly controls the frequency of H-abstraction reactions—the $\cdot O$ radical must attack a C−H bond and break it to form $\cdot OH$. Thus, molecules with fewer "exposed" C−H bonds, like iso-octane, are more resistant to auto-ignition. External production of $\cdot O$ radicals is relevant in the discussion of non-thermal plasma ignition techniques in Section 2.4.

Chain propagating reactions

Once initial radicals have been generated, they can attack the bonds of other molecules in H-abstraction reactions such as those in Equations 2.7 and 2.8.

$$CH_4 + \cdot H \rightleftharpoons \cdot CH_3 + H_2 \tag{2.7}$$

$$CH_4 + \cdot OH \rightleftharpoons \cdot CH_3 + H_2O \tag{2.8}$$

Chain propagation reactions also include reactions like the one depicted in Equation 2.9, which serve as the effective end of the combustion reaction for the C atom. Despite its

apparent simplicity, the intermediate step in the reaction has only recently been observed under thermal reaction conditions (Bjork et al., 2016).

$$\mathrm{CO} + \cdot\mathrm{OH} \longrightarrow \cdot\mathrm{HOCO} \longrightarrow \cdot\mathrm{H} + \mathrm{CO_2} \tag{2.9}$$

Reactions like those described by Equations 2.8 and 2.9 are particularly important, because the generation of H_2O and CO_2—two very stable molecules—releases substantial amounts of energy (Law, 2006; Bjork et al., 2016). This released heat increases the local gas temperature, increasing many other reaction rates and allowing the overall combustion reaction to proceed exponentially with the temperature increase.

Chain terminating or recombination reactions

Often, radical species recombine with one another or other radicals to produce stable products, releasing different amounts of energy depending on their collision partner. For example, the reaction in Equation 2.10, in which M carries away energy in the form of heat, is just the reverse of the reaction in Equation 2.3.

$$\cdot\mathrm{CH_3} + \cdot\mathrm{H} + \mathrm{M} \longrightarrow \mathrm{CH_4} + \mathrm{M} \tag{2.10}$$

However, the reaction in Equation 2.10 has three species in the reactant side instead of two. For gas-phase chemistry, this requires the *simultaneous* collision of three molecules, which is favored at high densities relative to low densities. Many termination reactions, much like the propagation reactions in Equations 2.8 and 2.9, create H_2O and thus generate significant amounts of heat. This is the case for the reactions in Equations 2.11 and 2.12.

$$\cdot\mathrm{CH_3} + \cdot\mathrm{OH} \rightleftharpoons \mathrm{CH_2} + \mathrm{H_2O} \tag{2.11}$$

$$\cdot\mathrm{H} + \cdot\mathrm{OH} + \mathrm{M} \longrightarrow \mathrm{H_2O} + \mathrm{M} \tag{2.12}$$

Some chain terminating reactions produce radicals but generally inhibit the overall rate of heat release, like the reaction in Equation 2.13.

$$\cdot\mathrm{H} + \mathrm{O_2} + \mathrm{M} \rightleftharpoons \cdot\mathrm{HO_2} + \mathrm{M} \tag{2.13}$$

Though the reaction in Equation 2.13 is technically a chain propagating reaction, $\cdot HO_2$ is a relatively stable radical compared to $\cdot O$, $\cdot H$, and $\cdot OH$. Thus, it is often classified as a chain termination step (Law, 2006; Warnatz et al., 2006).

NO_X chemistry

In Chapter 1, it was frequently mentioned that higher combustion temperatures result in greater production of harmful nitrogen oxides (NO_X). Here, a brief discussion on the chemistry of *thermal* NO_X formation is presented, with an aim to clarify the temperature dependence of the process. There are many paths to generate NO_X in combustion, but only the

thermal route is relevant to this dissertation. The first two elementary reactions of thermal NO_X formation were proposed by Zel'dovich (1946), and are given in Equations 2.14 and 2.15, while the third reaction in Equation 2.16 was later added by Lavoie et al. (1970).

$$N_2 + \cdot O \xrightarrow{k_{NOx,1}} \cdot NO + \cdot N \tag{2.14}$$

$$\cdot N + O_2 \xrightarrow{k_{NOx,2}} \cdot NO + \cdot O \tag{2.15}$$

$$\cdot N + \cdot OH \xrightarrow{k_{NOx,3}} \cdot NO + \cdot H \tag{2.16}$$

The first step in Equation 2.14 requires a high activation energy $E_{a,NOx,1} = 318$ kJ/mol to break the N≡N triple bond (McQuarrie and Simon, 1997), and, referring to Equation 2.2, predominantly explains the strong link between NO_X production and temperature T. Once $\cdot$N is present, it will quickly oxidize with available species, as in the reactions in Equations 2.15 and 2.16. By making a quasi-steady state approximation that $\cdot$N is consumed at the same rate that it is produced ($d[\cdot N]/dt \approx 0$) among the reactions in Equations 2.14, 2.15, and 2.16, the following relation in Equation 2.17 can be obtained (Warnatz et al., 2006):

$$\frac{d[\cdot NO]}{dt} \approx k_{NOx,1} \cdot [\cdot O][N_2] \propto [\cdot O][N_2] \cdot \exp\left(-\frac{E_{a,NOx,1}}{\hat{R}_u T}\right) \tag{2.17}$$

A 100 K increase in T results in an approximate doubling of $\cdot$NO production (McAllister et al., 2011). Though not applicable in all conditions, the quasi-steady state assumption in Equation 2.17 explicitly illustrates the temperature dependence of NO_X production in combustion environments.

Flammability limits

A brief overview is given here emphasizing the role of temperature and chemistry near the lean and dilute *flammability limits*—limits of ϕ and exhaust gas recirculation (EGR) rates, beyond which ignition is slow or difficult.

Lean flammability limit

Figure 2.1 shows the laminar flame speed, adiabatic flame temperature, and Minimum Ignition Energy (MIE) of CH_4-air mixtures as a function of equivalence ratio, ϕ. In Figure 2.1, MIE is an experimentally determined amount of energy required to obtain successful ignition of a fuel-oxidizer mixture. As ϕ decreases, the flame speed decreases substantially due to lower heat release rates, which also result in lower flame temperatures. Additionally, the MIE required for successful ignition increases for leaner mixtures. This is because the heat released from the initial chemical reactions is simply not large enough to increase the local gas temperature T enough for sustaining chain initiation and chain branching reactions like those in Equations 2.3 and 2.4 and in Equations 2.5 and 2.6, respectively. This phenomenon

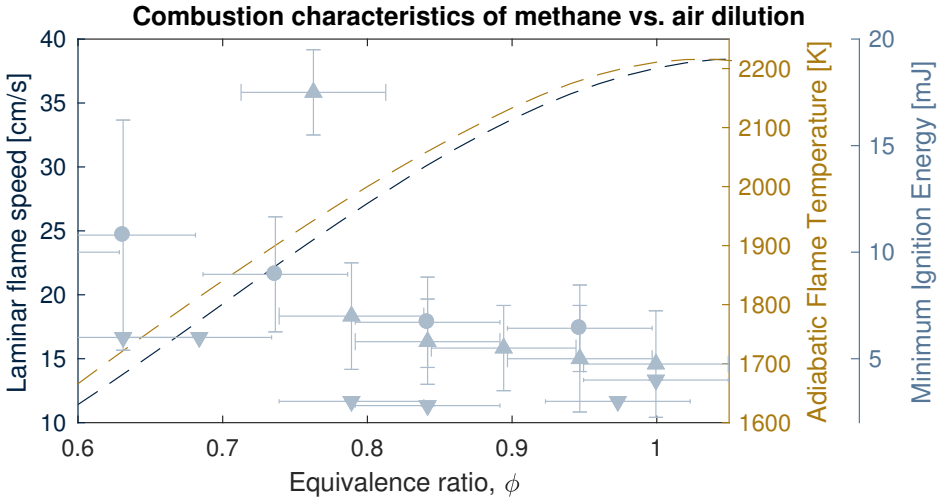

Figure 2.1: Laminar flame speed, adiabatic flame temperature, and Minimum Ignition Energy (MIE) as a function of ϕ for methane-air mixtures. As in Chapter 1, the laminar flame speeds and adiabatic flame temperatures are calculated using CANTERA (Goodwin et al., 2014) assuming an initial temperature of 300 K and initial pressure of 1 atm. Experimental MIE values are sourced from Phuoc and White (1999) (Δ), Ronney et al. (2001) via Kopecek et al. (2003) (∇), and data taken at University of California, Berkeley (McAllister et al., 2011) ($\circ$).

is directly related to Equation 2.2—reactions with high activation energies E_a are very sensitive to changes in T. From a thermal perspective, ignition can be viewed as a competition between heat generation from reactions and heat losses to the environment (McAllister et al., 2011), though this concept is not unique to the lean flammability limit. Applying more energy from the ignition source will increase the local gas temperature long enough for chain branching reactions to begin and lead to successful ignition. Once ignition is obtained, the developing flame must generate enough heat to continue the reactions. In general, mixtures without an adiabatic flame temperature of at least 1450 K are not able to successfully propagate on their own (Law, 2006). From a chemical kinetic perspective, ignition and flame propagation at the lean limit can be viewed as a competition between the chain branching reaction in Equation 2.5 and the chain termination reaction in Equation 2.13.

For internal combustion engines, the lean limits of operation are typically much richer than the lean flammability limits, because engines must operate in a stable manner. Mixtures near the lean limits present two main problems in this context—(1) a lean mixture can fail to ignite, resulting in a misfire, or (2) the lean mixture can ignite, but the flame propagates too slowly to consume all of the fuel during the cycle (Quader, 1976). Even during normal engine operation, flow fields, fuel-air ratios, and temperatures change from cycle to cycle and cylinder to cylinder. Since MIE and flame speed are steeper functions of ϕ in lean mixtures than in stoichiometric mixtures (Figure 2.1), these variations have significant impacts on the frequency of misfires or unfinished burn cycles (Heywood, 1988).

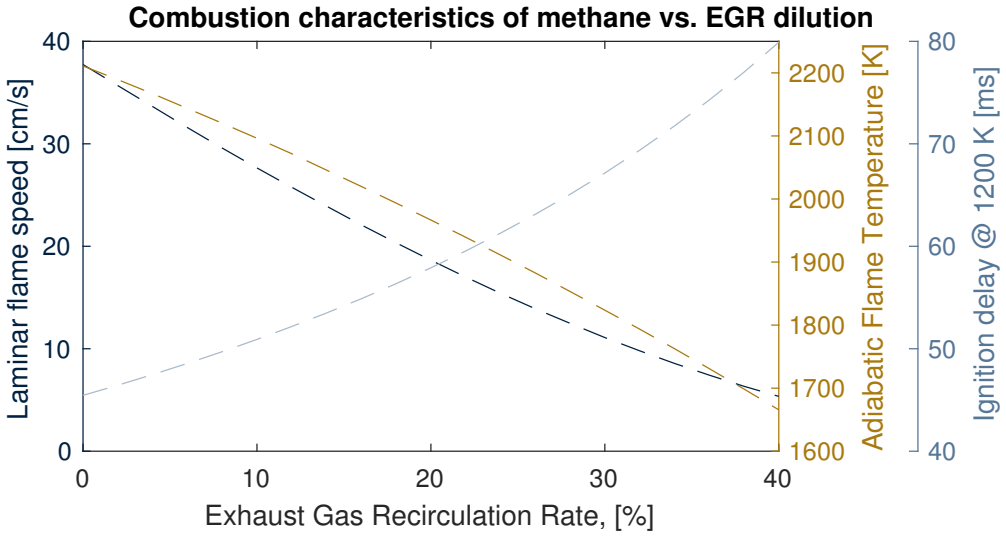

Figure 2.2: Laminar flame speed, adiabatic flame temperature, and ignition delay time as a function of EGR rate for methane-air mixtures. As in Chapter 1, the laminar flame speeds, adiabatic flame temperatures, and ignition delay times are calculated using CANTERA (Goodwin et al., 2014).

EGR or dilute limit

Similarly to the lean flammability limits, the exhaust gas recirculation (EGR) limits of ignition and flame propagation are controlled by a competition between heat losses and heat generation, as well as a competition between chain branching and chain terminating reactions. A plot of laminar flame speed, adiabatic flame temperature, and ignition delay time as a function of EGR rate for methane-air mixtures at $\phi = 1$ is shown in Figure 2.2. In Figure 2.2 and throughout this dissertation, the EGR rate is defined by Equation 2.18, where X_i is the molar fraction of species i.

$$\text{EGR } [\%] = \frac{X_{\text{CO}_2,\text{intake}} - X_{\text{CO}_2,\text{ambient}}}{X_{\text{CO}_2,\text{exhaust}} - X_{\text{CO}_2,\text{ambient}}} \tag{2.18}$$

When the rate of EGR increases, more "inert" CO_2 and N_2 are present in the mixture, and the concentrations of both O_2 and fuel—though in stoichiometric ratio with one another—decrease relative to the inert gases, which absorb heat and lower peak flame temperatures. This, in turn, lowers the overall rate of reaction, though the rate of reaction is also lowered because the fuel and oxidizer molecules simply have a more difficult time locating each other due to their low concentrations, as per Equation 2.2. As an additional consequence, the ignition delay time increases as the rate of EGR increases. Eventually, chain termination reactions exceed the chain branching reactions, and the heat losses to the mixture are too great to sustain ignition.

2.2 Plasma background

Selectively depositing energy to encourage specific chemical reactions can shift the balance between chain branching and chain terminating reactions at the flammability limits. This dissertation focuses on ignition of combustible mixtures via plasma chemistry, rather than by auto-ignition chemistry. For the purposes of this dissertation, a *plasma* is an ionized or partially ionized gas, in which enough electrons are separated from molecules to display collective behavior in response to electromagnetic fields (Chen, 2010). One of these behaviors key to this dissertation is the ability of plasma to conduct electrical current. The electrons and ions are subject to a force from an electric field $\vec{F}_E$, given by Equation 2.19.

$$\vec{F}_E = m\vec{a} = q\vec{E} \tag{2.19}$$

In Equation 2.19, q is the particle charge, $\vec{E}$ is the electric field generated by a charge separation across some distance, m is the particle mass and $\vec{a}$ is the particle acceleration. The energy potential associated with the charge separation is termed the *voltage*, and a greater amount of charge separated across a given distance is associated with a higher voltage and thus a higher electric field (Griffiths, 1999). The arrows over the variables indicate that they are vectors and possess both a magnitude and a direction. Since electrons are much less massive than ions, they accelerate much more readily in the presence of an electric field. With enough energy, these electrons can impact other molecules and activate chemical reactions otherwise not possible at low electron energies. This has important implications for plasmas, discussed in the following sections.

Plasma is the most common form of matter in the universe, and can be classified into different regimes by the concentration and energy of the electrons comprising it. Figure 2.3 shows different regimes of plasma sorted by these parameters. In this dissertation and in the literature, *electron energy* and *electron temperature* are often used interchangeably. Electron temperature, T_e, is here expressed in units of *electronvolts* (eV) for convenience (and because it is the unit that the plasma community largely uses), since the corresponding value of temperature in Kelvin is 1 eV = 11604.5 K and the corresponding value of energy in Joules is 1 eV = $1.602 \cdot 10^{-19}$ J, both of which are cumbersome to use at these energy scales. When converted to a molar quantity, 1 eV = 96.5 kJ/mol, and both of these units are given throughout the text of this dissertation for better reader comprehension. Electron number density, n_e, in these plots is expressed in m^{-3}. For reference, the number density n of air at standard conditions is on the order of 10^{25} m^{-3}. A key distinction is that for partially ionized plasmas, n_e is typically orders of magnitude smaller than n. On the far left of Figure 2.3, the volumetric concentration, or *number density*, of charged particles is quite low—lower than in the lowest pressures achievable on Earth. Plasmas in this regime are found in interplanetary space, such as in the solar wind, and are influenced by the Sun's magnetic field. At the other end of the spectrum lie the high-n_e, high-energy plasmas found in experimental nuclear fusion reactors, with high-pressure arcs found in lightning, welding applications, and automotive spark plugs positioned lower on the electron energy scale.

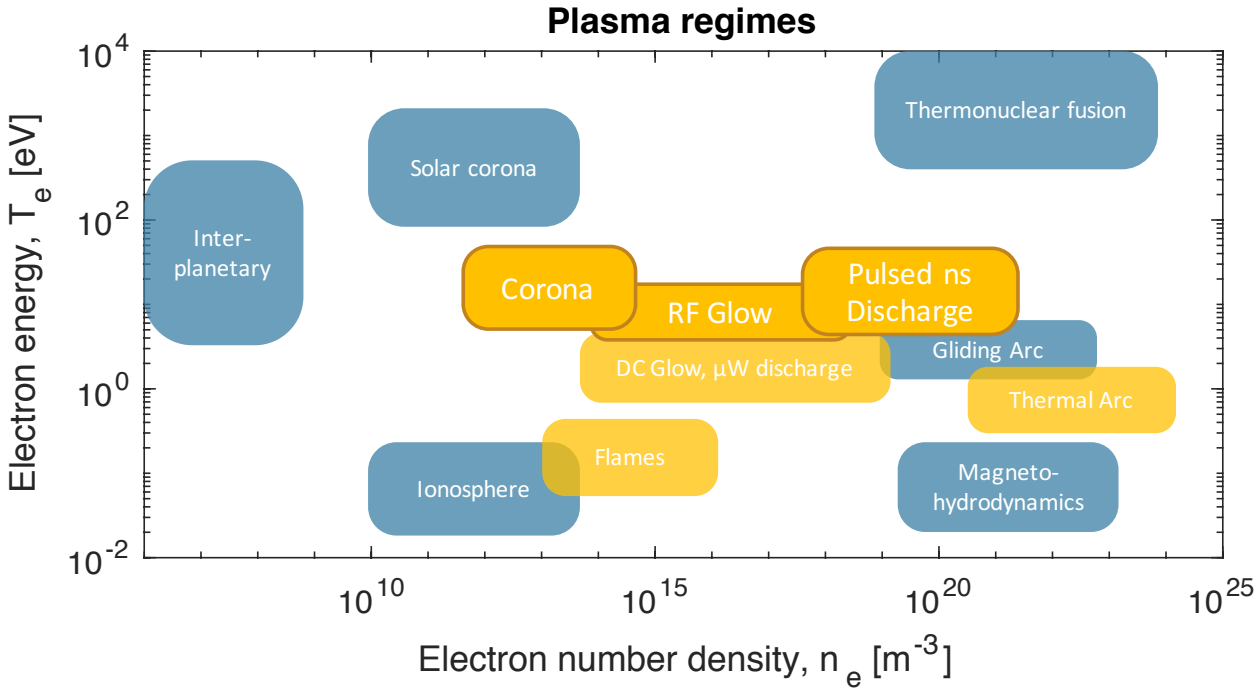

Figure 2.3: Different categories of plasmas, adapted from Fridman (2008c) and Ju and Sun (2015). Categories include interplanetary plasma, solar coronas, atmospheric coronas, the ionosphere, flames, radio frequency (RF) glow discharges, pulsed nanosecond discharges (PND), direct-current (DC) glow discharges, microwave (μW) dischages, gliding arcs, thermonuclear fusion plasma, magnetohydrodynamic plasma, and thermal arcs. The regimes of plasmas referenced in this dissertation are highlighted in gold, and the regimes specifically experimentally investigated are bolded.

Between these two extremes are a variety of different plasmas with different applications, and those referenced this dissertation are highlighted in gold, with those specifically experimentally investigated in this dissertation bolded. Particularly noteworthy is the inclusion of flames in the middle of the n_e range, and the low end of the T_e range—it has been known for some time that hydrocarbon flames can be manipulated by electric fields (Lawton and Weinberg, 1969). This is because many hydrocarbon flames are naturally partially ionized via the chemi-ionization pathway listed in the reactions in Equations 2.20 and 2.21.

$$\cdot\mathrm{CH} + \cdot\mathrm{O} \longrightarrow \mathrm{HCO^+} + \mathrm{e^-} \tag{2.20}$$

$$\mathrm{HCO^+} + \mathrm{H_2O} \longrightarrow \mathrm{H_3O^+} + \mathrm{CO} \tag{2.21}$$

Although the most common ion in flames is H_3O^+, hydrogen flames do not typically have ions because there is no pathway through HCO^+. The manipulation of ions and electrons in already-propagating flames is the subject of other research (DeFilippo, 2013; Han, 2016; Casey, 2016; Casey et al., 2017; Murphy et al., 2017) and is not discussed in further detail here.

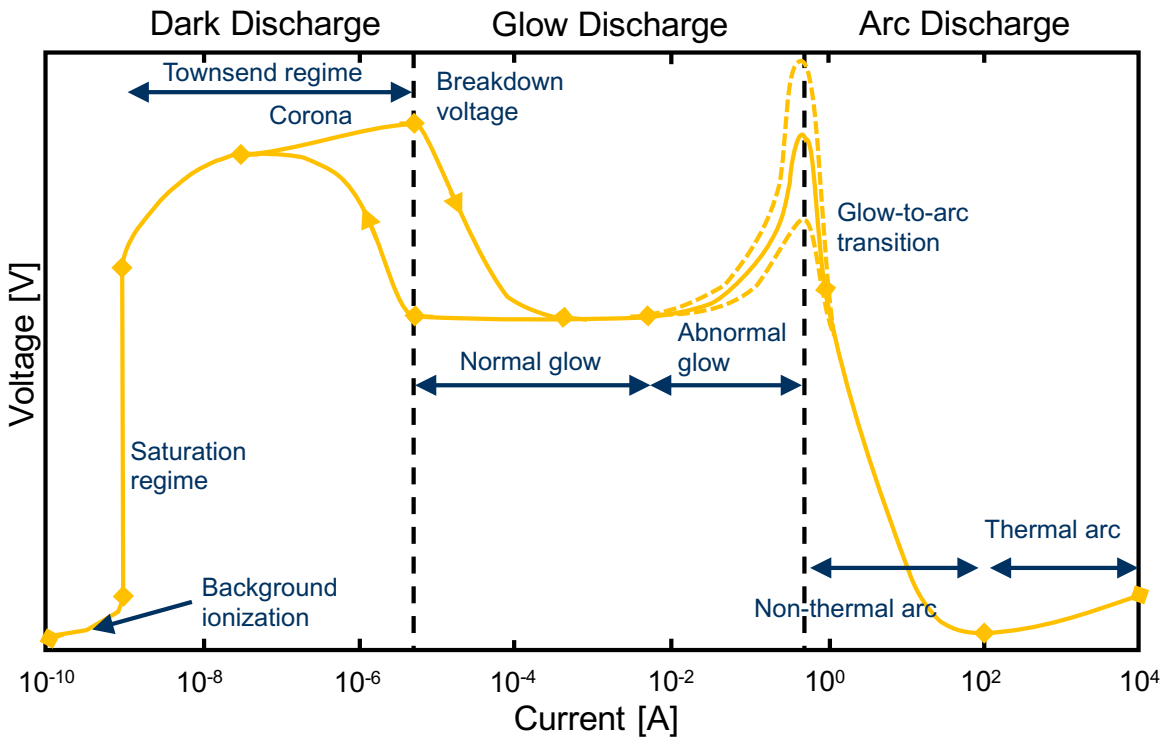

Figure 2.4: Current-Voltage curves separating the different discharge regimes, adapted from Llewellyn-Jones (1966), Fridman (2008a), and Casey (2016). The dashed lines around the glow-to-arc transition indicate variation in transition voltage due to dependence on electrode geometry.

Electric discharges and plasma generation

The discussion regarding Figure 2.3 only concerns naturally occurring plasmas, and only a few of them involve the generation of plasma due to a significant voltage potential, as is the case with two oppositely charged electrodes. Most human-made plasmas involve a flow of charge from one region to another, or oscillating regions of charge, in both cases controlled by an applied electric field $\vec{E}$. At any given moment, small numbers of electrons and ions exist in a gas due to their production via naturally occurring background radiation (Fridman, 2008c). These electrons and ions can be manipulated via applied electric fields to generate electrical discharges, and this is generally done via the application of a voltage potential through the gas. As the charged species accelerate according to Equation 2.19, they impact other species, ultimately creating discharges. Figure 2.4 shows an illustrative current-voltage curve for discharges between two electrodes, separated into different discharge regimes discussed in the following subsections.

Dark discharge regime

As voltage is first applied, charged particles migrate along the electric field toward the oppositely charged electrode, generating a small amount of current. The current flow stagnates in the saturation regime (the vertical line on the left of Figure 2.4) once the removal of charged species balances their generation via background ionization. As the voltage increases further, the electrons in the gas pick up enough collision energy to activate chemical processes, some of which are *electron-impact ionization reactions* that generate new ions and electrons. These newly created charged species then migrate to the electrodes, increasing the current flow and participating in additional ionization reactions (Llewellyn-Jones, 1966). This process taking place in the townsend regime (peak of voltage in the left of Figure 2.4) is termed an *electron avalanche* and is a similar concept to the combustion chain reactions discussed in Section 2.1. For most of this regime, there is no appreciable visible indication of these events, hence the term *dark discharge*. Additionally, the electrons are moving much more rapidly than the other species, and this is referred to as *non-thermal plasma* because the electrons are not in thermal equilibrium with the other species. As the strength of the electric field increases, the collisions of electrons with neutral molecules result in some *electron-impact excitation reactions*, in which a neutral molecule transitions to a higher energy state. For discharges in monotonic gases (such as helium, neon, argon, and the other noble gases), these are electronically-excited states, in which an electron moves to a higher energy orbital for a molecule (Lieberman and Lichtenberg, 2005a). Depending on the orbital configurations, the electrons later relax to the ground state, and the molecule releases the energy in the form of a photon, often in the visible or ultraviolet spectrum of light (Fridman, 2008b). These events typically concentrate in regions of high electric field, and the regions often form near sharp points of the electrodes (Griffiths, 1999). This visible phenomena is referred to as a *corona*. For discharges in other gases, such as air or fuel-air mixtures, the types of possible excitation increase (Lieberman and Lichtenberg, 2005b), since molecules with multiple atoms have multiple modes of energy storage (McQuarrie and Simon, 1997). Relevant electron impact excitation reactions are discussed in more detail in the plasma kinetics subsection after this one.

Glow discharge regime

As the voltage increases further, electrical breakdown occurs, in which the electrical resistance of the gas between the electrodes drops significantly (Llewellyn-Jones, 1966). As indicated in the middle of Figure 2.4, this increases the current, which then decreases the voltage potential across the electrodes as the charged particles migrate through the gas. At this point, there is a sufficient number density of electrons n_e such that electron-impact excitation reactions are sustained, and photonic emission is frequent enough to produce a visible 'glow' in some plasmas, hence the term *glow discharge regime*. In the *normal glow* regime, the plasma is located near the negatively charged electrode, and the production of additional electrons causes the region to grow at constant voltage. The growth of the plasma—and thus

number of electrons—results in a current rise as indicated in the flat region of Figure 2.4. After the plasma covers the negative electrode, then further current increase requires an increase in voltage in the *abnormal glow* regime (Fridman, 2008a). Since this process is influenced by the geometry of the electrode, variation exists in the curve of Figure 2.4 around the glow-to-arc transition.

Arc discharge regime

Once the voltage potential is high enough to strip electrons from the surfaces of the negatively charged electrode, an arc is generated. At this stage, the conductivity of the gas increases, reducing the voltage potential and increasing the current substantially, as shown in the right of Figure 2.4. New electrons are generated by thermionic emission in the solid electrodes and contribute to the current moving across the voltage potential (Fridman, 2008a). This plasma is now a *thermal plasma*; termed as such because the ions and neutral molecules in the gas are in thermal equilibrium with the electrons (Chen, 2010).

Reduced electric field and plasma kinetics in combustible mixtures

With the discharge regimes in mind, a more informative way to group plasmas from an engineering perspective is to categorize them by the kinds of chemical reactions present, since these typically govern the engineering application. The chemistry of these plasmas is, in turn, largely governed by the ability of electrons to gain momentum in an applied electric field. A major contributor to this ability is the density of the gas. In a denser gas, electrons collide with other molecules more frequently, and so they are unable to gain sufficient energy in a given electric field. Additionally, the strength of the electric field $E = |\vec{E}|$ is a function of both the electrode geometry (Perhaps parameterized by some inter-electrode distance L_{el}) and the applied voltage across the electrodes (V_{appl}), rendering comparisons among different systems difficult without some normalization. As such, the *reduced electric field*, E/n, which is the electric field $E = |\vec{E}|$ normalized by the overall number density n of the gas, is often used to characterize the intensity of the electric field. The unit of E/n used in this dissertation and in the literature is the *Townsend* (Td), and 1 Td $= 10^{-21}$ V·m^2. As with the electronvolt, this unit is used for convenience. When mapping the plasma regimes according to E/n, as in Figure 2.5, the relative positions of the regimes do not change, indicating that E/n is generally coupled with T_e. Noteworthy, also, is that the bolded groups in Figure 2.5 appear in similar positions as in Figure 2.4, highlighting that the amount of current flow is directly related to the number density of electrons n_e.

However, the chemical kinetic behavior is not so simple to characterize—non-thermal plasmas (and chemical kinetics) are inherently transient, and the kinetics cannot be determined by the E/n and n_e alone. The rate of change of E/n, n_e, and the response by species in the plasma can largely influence the overall chemistry and the ability of the plasma to transition from one regime to another (Fridman, 2008a). For example, if the electric field E/n is increased sufficiently slowly, electrons will not accelerate appreciably before collid-

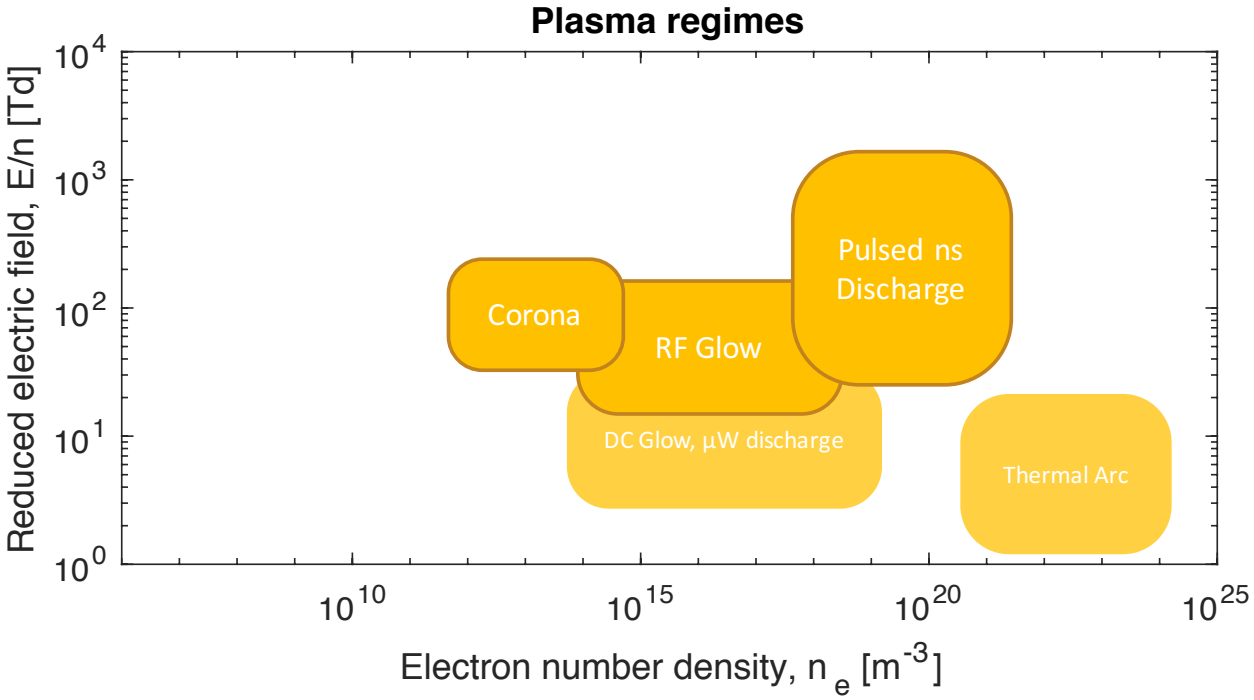

Figure 2.5: Different categories of plasmas arranged by electron number density n_e and reduced electric field E/n, adapted from Starikovskiy and Aleksandrov (2013) and Ju and Sun (2015). Categories include corona discharges, radio frequency (RF) glow discharges, pulsed nanosecond discharges (PND), direct-current (DC) glow discharges, microwave (μW) dischages, and thermal arcs. The regimes specifically experimentally investigated in this dissertation are bolded.

ing with other species. These low-energy collisions will generate excited state molecules different from those that would be generated in high-energy collisions, and these different excited state species will participate in different chemical reactions. The plasma dynamics of the different discharge regimes described in Figure 2.4 also influence the outcome—if E/n (and hence, V_{appl}) is large enough for long enough, a plasma will eventually transition to a thermal arc, which converts electrical energy into heat instead of desired products. Simultaneously achieving high voltage (via E/n) and high current (via n_e) to produce desired reactions (described shortly) while avoiding transition to arc requires the use of short-duration high-voltage pulses (Starikovskiy and Aleksandrov, 2013). This is the principle of pulsed nanosecond discharges (PND), which have a much higher E/n than the other categories of discharges shown. An example of the fractional energy deposition as a function of E/n for a simulated PND system in a CH_4-air mixture is shown in Figure 2.6, and some selected reaction types shown are discussed in the following subsubsections.

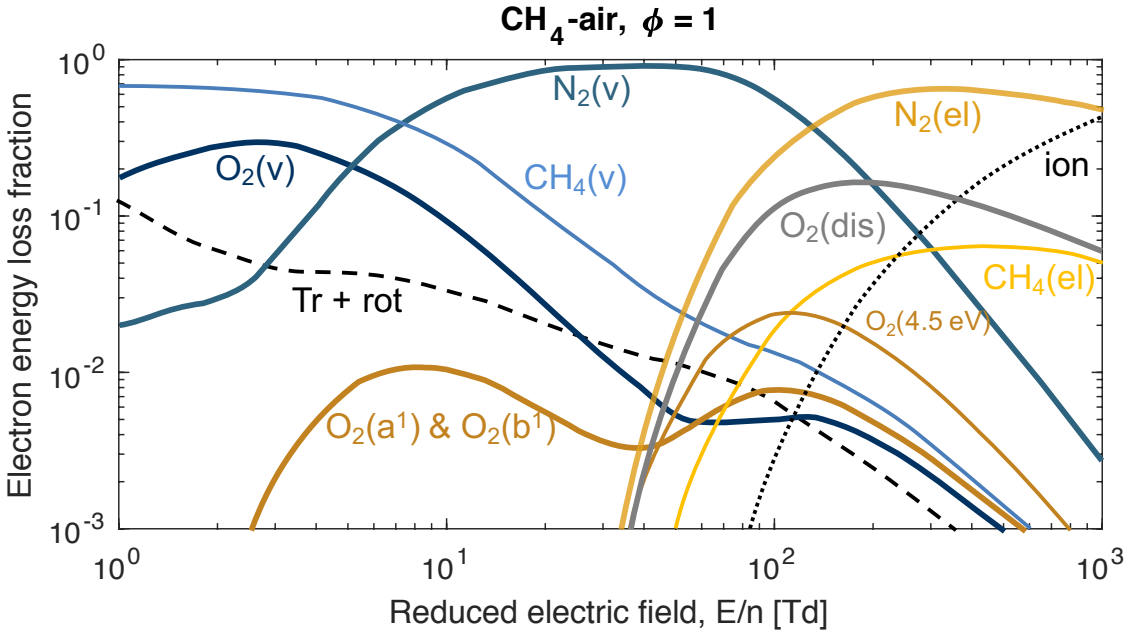

Figure 2.6: Diagram of electron energy deposition in a stoichiometric CH_4-air mixture calculated by solving the Boltzmann equation (Hagelaar and Pitchford, 2005). Adapted from Starikovskiy and Aleksandrov (2013).

Electron-impact ionization reactions

As mentioned, electron-impact ionization reactions are critical to self-sustaining electrical discharges, because they produce additional electrons and ions that can be manipulated by an applied electric field. Examples of electron-impact ionization reactions relevant to this dissertation are given in Equation 2.22 and Equation 2.23.

$$e^- + O_2 \longrightarrow O_2^+ + 2\,e^- \tag{2.22}$$

$$e^- + CH_4 \longrightarrow CH_4^+ + 2\,e^- \tag{2.23}$$

As shown in Figure 2.6, energy loss of electrons to ionizations in atmospheric CH_4-air mixtures for $\phi = 1$ typically occurs at $E/n > \sim$100 Td. The energy associated with the ionization of O_2 is approximately 12.14 eV, (1170 kJ/mol), which is much larger than the energy associated with dissociation alluded to earlier, 5.12 eV (494 kJ/mol) (Lieberman and Lichtenberg, 2005b).

Electron-impact excitation reactions

As discussed, electron collisions can impact neutral molecules and excite them, but the nature of the excitation depends both on the neutral molecule and the energy of the collision. As mentioned, multi-atom species have more modes of energy storage than single-atom species. A generalized electron-excitation reaction is given in Equation 2.24 for a collision with the

diatomic molecule O_2.

$$e^- + O_2 \longrightarrow O_2^* + e^- \tag{2.24}$$

O_2^* can be rotationally-excited O_2, vibrationally-excited O_2, or electronically-excited O_2. As shown in the left half of Figure 2.6, vibrational excitation dominates the plasma chemistry in typical fuel-air mixtures at atmospheric pressures for $E/n < \sim$100 Td, above which electronic excitation and dissociation reactions dominate. The distinctions between these states for diatomic species are outlined in the following paragraphs.

Rotational excitation: The energy differences between rotational states in molecules are generally small (McQuarrie and Simon, 1997); for O_2 they are roughly 0.02 eV (1.93 kJ/mol) (Lieberman and Lichtenberg, 2005b), and so even low-energy electron collisions activate these excited states. As indicated in Figure 2.6, approximately 10% of the energy of the electrons is lost to translational (an electron impacts a molecule and simply increases the speed of that molecule) and rotational excitation across all species in atmospheric CH_4-air mixtures for $\phi = 1$ at lower levels of E/n. This fraction decreases for higher E/n as various vibrationally- and electronically- excited states become more likely. The presence of rotationally-excited species does not significantly alter combustion chemical kinetic pathways in temperature and pressure conditions relevant to internal combustion engines (DeFilippo, 2013), and so these states are not detailed extensively in this dissertation.

Vibrational excitation: The energy differences between vibrational states in diatomic molecules are typically larger than those between rotational states (McQuarrie and Simon, 1997), and low-energy electron-neutral collisions frequently vibrationally excite the molecules. Relevant reactions are those such as in Equations 2.25 and 2.26.

$$e^- + O_2 \longrightarrow O_2(\mathrm{vib}_1) + e^- \tag{2.25}$$

$$e^- + N_2 \longrightarrow N_2(\mathrm{vib}_1) + e^- \tag{2.26}$$

The example reactions in Equations 2.25 and 2.26 require a collision energy of 0.19 eV (18.3 kJ/mol) (Lieberman and Lichtenberg, 2005b) and ∼1.7–3.5 eV (163.8–337.2 kJ/mol) (Fridman, 2008b), respectively. Though these reactions only display the first vibrationally-excited state of each O_2 and N_2, the other vibrationally-excited states of these molecules are accessible as well. Vibrationally-excited species in sufficient quantities beyond those typical in thermal equilibrium conditions can have a substantial influence on combustion chemistry (Starikovskaia, 2014), and this is discussed further in Section 2.4.

Electronic excitation: The energy differences between different electronic states in diatomic molecules vary according to the molecular orbital configuration of the molecule. For example, ground state N_2, $N_2(X^1\Sigma_g^+)$, is in a singlet electronic state, and this is the case with most ground state molecules (McQuarrie and Simon, 1997). The electron energies required for electronic excitation reactions in Equations 2.27 and 2.28 are about ∼11 eV

(1059 kJ/mol) (Fridman, 2008b), and these excitations typically only occur in stoichiometric fuel-air mixtures for $E/n > \sim$40 Td as shown in Figure 2.6.

$$e^- + N_2(X^1\Sigma_g^+) \longrightarrow N_2(A^3\Sigma_u^+) + e^- \tag{2.27}$$

$$e^- + N_2(X^1\Sigma_g^+) \longrightarrow N_2(B^3\Pi_g) + e^- \tag{2.28}$$

In contrast, ground-state O_2, $O_2(X^3\Sigma_g^-)$, is in a triplet electronic state, which means that two of its electrons are unpaired in separate orbitals and have the same spin (McQuarrie and Simon, 1997). This unusual circumstance has unusual consequences; the energies required for the electronic excitation reactions in Equations 2.29 and 2.30 are 0.977 eV (94.2 kJ/mol) and 1.627 eV (156.7 kJ/mol), respectively (Lieberman and Lichtenberg, 2005b), and these excitations can occur at lower E/n as shown in Figure 2.6 (Starikovskiy and Aleksandrov, 2013). As such, these particular excited forms of O_2 are relatively unique and have attracted much attention in the plasma community (Ionin et al., 2007).

$$e^- + O_2(X^3\Sigma_g^-) \longrightarrow O_2(a^1\Delta_g) + e^- \tag{2.29}$$

$$e^- + O_2(X^3\Sigma_g^-) \longrightarrow O_2(b^1\Sigma_g^+) + e^- \tag{2.30}$$

Electronically-excited species—even in small quantities—can dramatically influence ignition and flame propagation (Starik et al., 2015), and this is discussed further in Section 2.4.

Electron-impact dissociation reactions

At sufficient electron energies, electrons can impact neutral molecules and they can subsequently dissociate, but this path is not necessarily direct; the process can take multiple collisions. An *indirect method* of electron-impact dissociation relevant to this dissertation is a pathway in which a vibrationally-excited molecule impacts a second molecule, causing that second molecule to dissociate (Fridman, 2008b). For example, the vibrationally-excited N_2 produced in the reaction in Equation 2.25 can participate in a reaction like that in Equation 2.31 (Popov, 2011).

$$N_2(vib_1) + O_2 \longrightarrow \cdot O + \cdot O + N_2 \tag{2.31}$$

Because N_2 possesses more vibrational energy than it would in the ground state, the dissociation of O_2 by a collision requires less translational energy than the dissociation reaction in Equation 2.4 in Section 2.1. In contrast, a *direct method* of electron-impact dissociation relevant to this dissertation is a pathway in which a molecule is electronically excited in a single collision into an unstable state that subsequently dissociates. Relevant examples are given in Equations 2.32 and 2.33:

$$e^- + O_2 \longrightarrow O_2^{**} + e^- \longrightarrow \cdot O + \cdot O + e^- \tag{2.32}$$

$$e^- + CH_4 \longrightarrow CH_4^{**} + e^- \longrightarrow CH_3 + \cdot H + e^- \tag{2.33}$$

In the reactions shown in Equations 2.32 and 2.33, the ** indicates an unstable state that lasts for less than one molecular vibration before the molecule dissociates (Lieberman and Lichtenberg, 2005b). Regardless of the specific mechanism of dissociation, these reactions in Equations 2.31, 2.32, 2.33, and others like them generate radicals such as $\cdot$O and $\cdot$H. As such, these reactions are of particular interest for plasma-assisted ignition (Starikovskaia, 2006; Starikovskiy and Aleksandrov, 2013; Ju and Sun, 2015; Aleksandrov et al., 2009) and their consequences are discussed in more detail in Section 2.4.

2.3 Thermal plasma ignition

In traditional ignition technologies, the third body collisions that lead to radical chain branching reactions are initiated by high temperatures in a *thermal* plasma, a gas that has been ionized and whose electrons are in thermal equilibrium with the other ions and molecules. This is typically provided by a capacitative or inductive spark (Heywood, 1988), occurring in the thermal arc regime of Figures 2.3, 2.4, and 2.5 between two electrodes when the voltage across them is large enough. As indicated in Figures 2.3, 2.4, and 2.5, thermal arcs are characterized by high n_e, low E/n and T_e, and high current and low voltage after the glow-to-arc transition (Heywood, 1988). In automotive spark plugs, the total amount of potential energy is fixed for each engine cycle (either in the inductive coil or a capacitor), and so the voltage and current rapidly drop as the energy is depleted. The large number of collisions in this discharge results in high local gas temperatures ($\sim$6000 K) during the arc (Heywood, 1988), promoting chain initiation reactions that lead to ignition as discussed in Section 2.1. The required voltage for a successful spark (or *arc*) depends on the distance between the electrodes, the density of the gas, and the ionization energy of the gas (which depends on its constituent molecules). In general, the voltage required for a successful thermal arc increases with the neutral number density n (and the pressure), while the inter-electrode distance L_{el} required decreases (Fridman, 2008a).

The mechanism of spark generation is relevant for both traditional and advanced ignition techniques; all of the discharges considered in this dissertation fall in the regimes outlined in Figure 2.4, and thermal arc discharges must transition through the dark and glow discharge regimes before occurring. When an electric field is applied to a gas between electrodes, the initial wave of electrons propagates across the gap towards the cathode, generating more electrons and ions via electron-impact ionization reactions described previously (Sher et al., 1992). The path these electrons create is referred to as a *streamer*, and the electrons leave behind a trail of positive ions (and other reactive species (Ono, 2016)) as the streamer propagates from the anode to the cathode. As the electrons in the head of the streamer reach the cathode, they generate additional electrons from the cathode surface which flow toward the positively charged ion region, creating an ionized channel through which more current can readily flow. This greatly increases the conductivity of the gas and ultimately additional ionization processes transition the discharge to a thermal arc (Fridman, 2008a). If the electric field is switched off before the streamers reach the cathode, the transition to

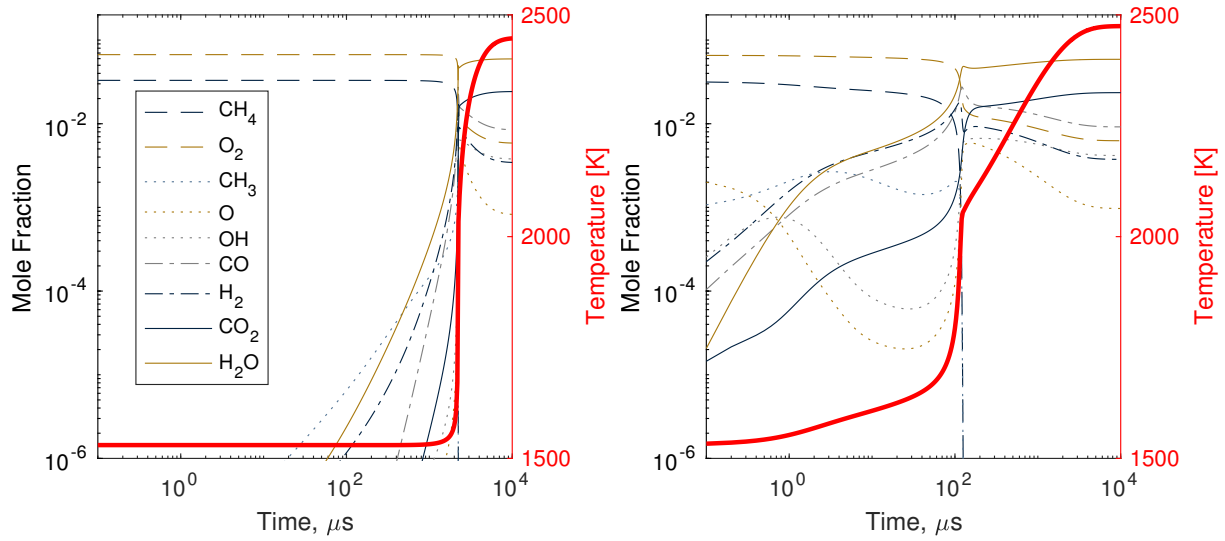

Figure 2.7: Comparison of CH_4-O_2-Ar ignition via autoignition as described in Section 2.1 (left) and via ignition by radical species produced from a pulsed nanosecond discharge (right). Constant-pressure ignition simulations conducted with Cantera (Goodwin et al., 2014) using the GRI-MECH 3.0 mechanism (Smith et al., 1999) and initial conditions originally determined by Kosarev et al. (2008).

thermal arc can be delayed, and this is the principle behind non-thermal plasma ignition.

2.4 Non-thermal plasma ignition

In principle, the transition to thermal arc can be stopped by pulsing the electric field applied between the electrodes, leaving ions and reactive species previously discussed in Section 2.2 that can ignite a fuel-air mixture chemically rather than thermally. In this regime, the electrons are at a much higher temperature than the ions and neutral molecules, making this process a *non-thermal plasma*. More comprehensive reviews of the alternate ignition pathways are given by Starikovskaia (2014) and Ju and Sun (2015), but key processes are described in this section.

Reactions with radical species

The radicals produced by the electron-impact dissociation reactions like the kind in Equations 2.31 through 2.33 generally facilitate ignition such as in the reactions in Equations 2.5, 2.6, 2.7, 2.10, 2.12, and 2.13 discussed in Section 2.1. Though these reactions are not unique to non-thermal plasma ignition, these species are produced in significant quantities at lower temperatures than they would otherwise occur, as shown in Figure 2.7 (Kosarev et al., 2008).

Reactions with excited molecules

The vibrationally- and electronically-excited species produced in the electron-impact excitation reactions described in Section 2.2 can directly react with fuel and oxygen molecules, typically with lower activation energies than their ground-state counterparts described in Section 2.1. One particularly relevant example is the reaction of $O_2(a^1\Delta_g)$ with $\cdot H$ as shown in Equation 2.34, which is an "excited" analog to the critical chain-branching reaction in Equation 2.5.

$$\cdot H + O_2(a^1\Delta_g) \rightleftharpoons \cdot OH + \cdot O \tag{2.34}$$

This reaction has a much lower activation energy than the reaction in Equation 2.5, which means chain-branching can occur at lower temperatures than would otherwise be possible (Starik et al., 2015). As with the chain-branching reaction in Equation 2.5, there is a competing chain-terminating reaction (Chukalovsky et al., 2016), listed in Equation 2.35.

$$\cdot H + O_2(a^1\Delta_g) + M \rightleftharpoons \cdot HO_2^*(^2A';\nu') \tag{2.35}$$

Although the kinetics of all of these reactions are still not completely understood (Chukalovsky et al., 2016), reactions with excited species like $O_2(a^1\Delta_g)$ open up kinetic pathways that can enhance ignition in harsh combustion environments (Ju and Sun, 2015).

Fast gas heating processes

Many of the excited species produced in non-thermal plasma discharges can lose their energy in collisions and drop back to their ground states. This energy frequently manifests itself in the form of increased translational energy of molecules, locally increasing the temperature of the fuel-air mixture and promoting ignition through the traditional thermal pathways outlined in Section 2.1. These processes are referred to in this dissertation and in the literature as *fast gas heating processes*, and have been suspected as a significant contributor to experimentally observed combustion enhancement in non-thermal plasma ignition technologies (Wolk and Ekoto, 2017). Some of the relevant processes are discussed in this subsection, in order of fastest to slowest processes.

Rotational-to-translational relaxation

As mentioned in Section 2.2, rotational excitation of species occurs at relatively low E/n. These species are very short-lived, because the additional rotational energy is given up to translational energy in a very small number of collisions (Vincenti and Kruger, 1967; Brau and Jonkman, 1970). Thus, this process is classified as a fast gas heating process; however, due to the small amounts of energy associated with rotational excitation, the amount of heating is not readily apparent at engine-relevant pressures and temperatures.

Quenching of electronically-excited state species

Electronically-excited molecules such as $N_2(A^3\Sigma_u^+)$ and $N_2(B^3\Pi_g)$ possess sufficient energy to impart substantial energy to a collision partner, such as to the ground state N_2 in the reactions in Equations 2.36 and 2.37 (Tholin et al., 2014; Shkurenkov and Adamovich, 2016):

$$N_2 + N_2(A^3\Sigma_u^+) \longrightarrow N_2 + N_2 \tag{2.36}$$

$$N_2 + N_2(B^3\Pi_g) \longrightarrow N_2 + N_2(A^3\Sigma_u^+) \tag{2.37}$$

In these cases, the products have more translational energy than the reactants, and the local temperature of the fuel-air mixture increases. These reactions are termed *quenching* reactions. Thus, the reactions in Equations 2.36 and 2.37 are significant energy transfer pathways even though they possess neither a fuel nor an oxidizer (Shkurenkov et al., 2014). Often, however, an electronically-excited O_2 molecule undergoes quenching as in Equation 2.38 in addition to the chain branching and terminating reactions in Equations 2.34 and 2.35 (Chukalovsky et al., 2016):

$$\cdot H + O_2(a^1\Delta_g) + M \longrightarrow \cdot H + O_2(X^3\Sigma_g^-) + M \tag{2.38}$$

Reactions like this do not alter the radical population but do increase the temperature of the mixture, and so can facilitate ignition in a thermal manner (Xu et al., 2014).

Vibrational-to-translational relaxation

The vibrationally-excited species generated in non-thermal plasma discharges are generally long-lived compared to the other kinds of excited species (Vincenti and Kruger, 1967), but they contribute substantially to gas heating as they collide with other molecules (Popov, 2011; Mintoussov et al., 2011; Pintassilgo and Guerra, 2015). Additionally, as mentioned, they also contribute to increased radical population by dissociating other molecules on impact, such as in the reaction in Equation 2.31.

2.5 Non-thermal plasma ignition applications

There is much ongoing research examining the chemical kinetic mechanisms of these discharges in combustion environments (Kosarev et al., 2008; Starikovskaia, 2014; Ju and Sun, 2015; Popov, 2016; Rousso et al., 2017), and fundamental investigations like these supplement the automotive engine-related work detailed in this dissertation. All of the chemical reaction classes discussed in Sections 2.1, 2.2, 2.3, and 2.4 have important implications when applied to practical ignition systems, which often must operate in harsh environments and are constrained by automotive engine design considerations. As frequently mentioned in Section 1.1, uncontrolled auto-ignition (colloquially known as engine knock) constrains automotive engine efficiency and intake pressure, and significant quantities of radical species

such as $\cdot$H. $\cdot$O, and $\cdot$OH homogeneously distributed in a combustion chamber will result in this undesirable phenomenon (Law, 2006). As discussed in Sections 2.2 and 2.4, some of these radical species are produced in non-thermal plasmas, so care must be taken to localize their production in a combustion chamber so as to yield a controlled ignition event. Depending on the geometry of the electrode used in an automotive engine combustion chamber, the volume of a non-thermal plasma discharge can be many orders of magnitude larger than the discharge volume of a traditional inductive spark plug. For this reason, ignition can occur more quickly and more robustly due to the increased radical population in the larger volume (Bonazza et al., 1992; VanVoorhies et al., 1992). In principle, this phenomenon can reduce the combustion duration in boosted dilute-operation engines, which is one of the main thrusts for reducing fuel consumption and harmful emissions as identified in Chapter 1.

Engine load-speed paradigms

Automotive engine operation is often characterized by the engine load and speed, and this characterization is important to note because of its impact on the effectiveness of different ignition strategies in engines. While speed is given in a familiar revolutions-per-minute (rpm), load is typically parameterized by Mean Effective Pressure (MEP), that is, the average in-cylinder pressure during the cycle. This value is useful because, when multiplied by the displacement and speed of the engine, an average power output can be calculated; the MEP serves as a measure of a heat engine's ability to do work independent of its size (Heywood, 1988). Indicated MEP (IMEP) refers to the average recorded in-cylinder pressure, while Brake MEP (BMEP) refers to the "brake" work available after accounting for all frictional and heat losses. The BMEP of a typical naturally-aspirated (no turbo- or super-charging) at full load is around 8–10 bar BMEP (Heywood, 1988), while boosted engines operate above this MEP. Higher engine loads mean higher pressures, and higher pressures translate to higher number densities and lower E/n for non-thermal plasma ignition technologies. This limits access to some of the plasma chemistry discussed in Section 2.2 and 2.4. Thus, high-load operation has historically been a limitation on the use of these advanced ignition technologies in automotive engines (VanVoorhies et al., 1992; Sher et al., 1992) due to not only the increased frequency of radical recombination reactions as mentioned in Section 2.1, but also the reduced E/n as is discussed in the following subsection.

Development of advanced ignition for automotive engines

Advanced ignition strategies have been tested in internal combustion engines for many decades (Dale et al., 1997), though only in the last 20 years has there been significant investigation into non-thermal plasma ignition techniques (Tropina et al., 2016; Zheng and Yu, 2015). During the energy crises of the 1970s, research on advanced ignition strategies centered on multiple spark events in one cycle (Harrington et al., 1974; Asik and Bates, 1976), higher-energy ignition (Johnston et al., 1975), laser ignition (Dale et al., 1978), plasma torch ignition (Dale and Oppenheim, 1981), and multiple spark plugs (Nakamura et al.,

1985), among others. Recent advances have been made in microwave-assisted spark plugs (μWASP) (Wolk et al., 2013; DeFilippo et al., 2011, 2015). These μWASP systems do not initiate ignition with a non-thermal plasma; rather, a traditional spark plug generates a thermal plasma, and then microwaves are used to manipulate and sustain the plasma. As such, these advanced ignition strategies are not discussed at length in this dissertation. Likewise, laser ignition and high-energy ignition in engines remain topics of research (Peters and Akih-Kumgeh, 2017; Hayashi et al., 2017), but are also not discussed for the same reason.

Ignition in the glow regime has been investigated for some time, and two main methods to generate and/or sustain a glow discharge have emerged: (1) using high voltage direct current (DC) to the electrode and (2) using radio frequencies (RF) generated by resonant circuitry that includes the electrode (henceforth referred to as "RF corona discharge" ignition). The ionization processes in these different discharge methods are similar (Fridman, 2008a), but the techniques to modulate and prevent transition to thermal arc are different, and their potentials for implementation have varied depending on technological advancements throughout their historical development. Early experiments utilizing high voltage DC corona discharges showed promise, but power limitations of available technology restricted any significant improvements in engine performance to low loads (Sher et al., 1992). Much progress has subsequently been made in the RF corona discharge technology (VanVoorhies et al., 1992; Bonazza et al., 1992; Stiles et al., 1997; Mcintyre et al., 2001; Varma and Thomas, 2013), with the concept finally demonstrating an improvement in engine performance (Hampe et al., 2015, 2013; Mariani and Foucher, 2014; Schenk et al., 2015). High voltage DC corona discharge ignition technologies have also advanced, a notable technology being in the form of "pulsed corona" discharge (Cathey et al., 2007; Fridman, 2008a). These concepts are implemented in current pulsed nanosecond discharge ignition technologies that also demonstrate improvement in gasoline direct-injection (GDI) engine performance (Sevik et al., 2016). Thus, regardless of how a corona discharge is generated, the technology has matured to the point where ignition via non-thermal plasma in engines at high loads can be examined more thoroughly to characterize its potential for implementation in production automotive engines.

State-of-the-art advanced ignition in automotive engines

A list of recent engine experiments examining the use of advanced ignition strategies to extend the lean limits of stable engine operation is given in Table 2.1 and a similar list of recent engine experiments examining the extension of EGR limits is shown in Table 2.2. In the interest of relevance for near-term implementation in production automotive engines—the details of which are discussed in Chapter 1—only studies with 4-stroke engines using gasoline as the fuel are listed. The values of load and speed of each engine experiment are also listed in Tables 2.1 and 2.2. If no additional boosting of intake pressure takes place, engines operating in leaner regimes produce lower loads simply because there is less fuel. A plot of the experiments highlighting the lean limit extension as a function of power density (average power produced divided by engine displacement) is given in the left of Figure 2.8,

Table 2.1: List of recent 4-stroke gasoline engine experiments in the literature utilizing advanced ignition techniques to extend the lean limits of stable operation, as shown in the left of Figure 2.8. Shown in the table are the authors, the advanced ignition technology (AI tech), the engine speed, SI engine load (mean effective pressure), the SI lean limit ($\phi_{LL,SI}$), the AI engine load, and the AI lean limit ($\phi_{LL,AI}$). Technologies include Microwave-Assisted Spark Ignition (μWASP), Radio-Frequency Corona Discharge Ignition (RFCDI), Pulsed Nanosecond Discharge Ignition (PND), and High-Energy Ignition (HEI).

Authors	AI tech.	Speed [rpm]	SI load [kPa]	$\phi_{LL,SI}$	AI load [kPa]	$\phi_{LL,AI}$
Shiraishi et al. (2009)	PND	1200	1400	0.70	1400	0.65
Ikeda et al. (2009)	μWASP	2000	275	0.76	275	0.61
Ikeda et al. (2009)	μWASP	2000	500	0.74	500	0.59
DeFilippo et al. (2011)	μWASP	1200	780	0.79	720	0.75
DeFilippo et al. (2011)	μWASP	1200	740	0.70	700	0.67
Lefkowitz et al. (2012)	μWASP	2000	900	0.87	800	0.70
Lefkowitz et al. (2012)	μWASP	5000	900	0.87	750	0.68
Hampe et al. (2013)	RFCDI	2000	200	0.74	200	0.63
Mariani and Foucher (2014)	RFCDI	1400	400	0.66	400	0.64
Mariani and Foucher (2014)	RFCDI	1400	800	0.65	800	0.60
Schenk et al. (2014)	RFCDI	1100	300	0.63	300	0.56
Schenk et al. (2015)	RFCDI	2000	200	0.86	200	0.77
Schenk et al. (2015)	RFCDI	2000	600	0.74	600	0.67
Schenk et al. (2015)	RFCDI	2000	1400	0.67	1400	0.61
Schenk et al. (2015)	RFCDI	4000	600	0.74	600	0.68
Sevik et al. (2016)	PND	1500	560	0.67	560	0.59
Hayashi et al. (2017)	HEI	1200	500	0.57	500	0.56
Hayashi et al. (2017)	HEI	3000	900	0.63	900	0.56

Table 2.2: List of recent 4-stroke gasoline engine experiments in the literature that utilized advanced ignition techniques to extend the EGR limits of stable operation, as shown in the right of Figure 2.8. Shown in the table are the authors, the advanced ignition technology (AI tech), the engine speed, SI engine load (mean effective pressure), the SI EGR limit ($\text{EGR}_{max,SI}$), the AI engine load, and the AI lean limit ($\text{EGR}_{max,AI}$). Technologies include Radio-Frequency Corona Discharge Ignition (RFCDI), and Pulsed Nanosecond Discharge Ignition (PND).

Authors	AI tech.	Speed [rpm]	Load [kPa]	$\text{EGR}_{max,SI}$ [%]	$\text{EGR}_{max,AI}$ [%]
Schenk et al. (2015)	RFCDI	2000	200	2.0	14.0
Schenk et al. (2015)	RFCDI	2000	600	15.0	22.0
Schenk et al. (2015)	RFCDI	2000	1400	22.0	24.0
Schenk et al. (2015)	RFCDI	4000	600	10.0	21.0
Sevik et al. (2016)	PND	1500	560	21.0	27.0
Pineda, Wolk, Chen and Dibble (2016)	RFCDI	2000	870	16.0	25.0
Pineda, Wolk, Chen and Dibble (2016)	RFCDI	2000	2041	10.0	15.0

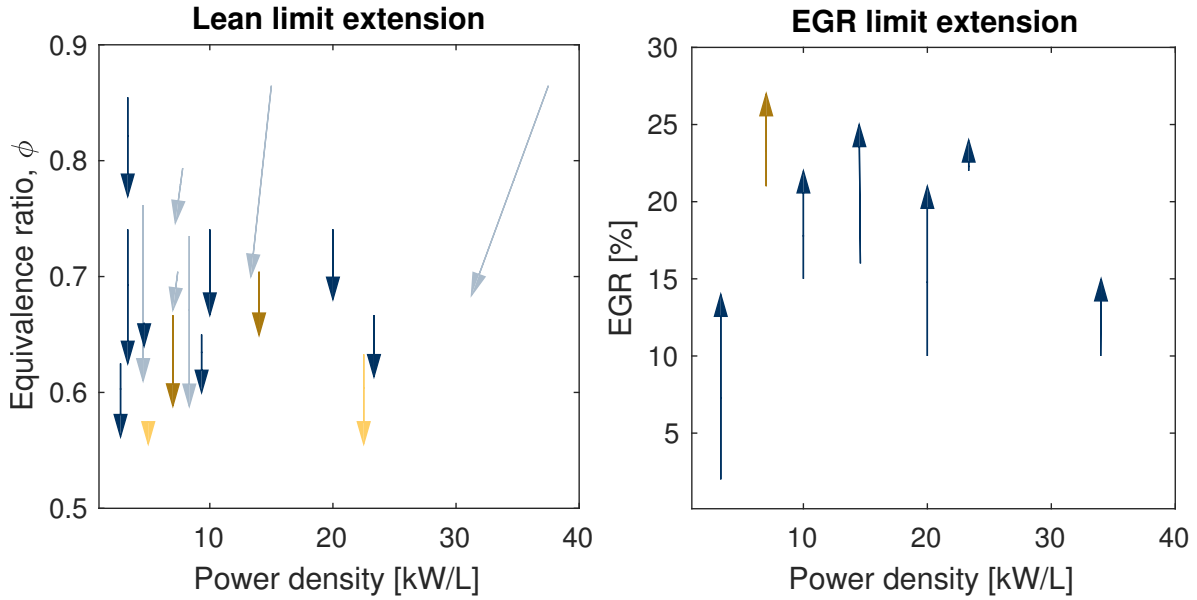

Figure 2.8: Extension of lean limits of stable operation for 4-stroke gasoline engines (left), extension of EGR limits of stable operation for 4-stroke gasoline engines (right), both plotted as a function of engine power density (power output divided by engine displacement). Microwave-assisted spark ignition in light blue, corona discharge ignition in dark blue, pulsed nanosecond discharge ignition in dark gold, and high energy ignition in light gold. Original experiments referenced in Tables 2.1 and 2.2.

while a similar plot highlighting the EGR limit extension is given in the right of Figure 2.8. This metric of normalizing the results across different engines has some caveats—there are significant variations in engine geometry, speed, compression, and operation; for example, the use of direct-injection and variable valve timing is not consistent across the experiments in Tables 2.1 and 2.2, and in Figure 2.8. Additionally, high-speed and low-load engines still provide substantial power output; even though there is less time for combustion per cycle, more ignition events occur in a given time period and thus skew the power density to high values. As such, the comparisons should be interpreted cautiously; however, some trends are apparent in Figure 2.8. In general, it is more difficult to extend the lean or EGR limits of operation at high loads and power densities, and a variety of different techniques have been investigated to do so, such as Pulsed Nanosecond Discharge (PND), microwave-assisted spark plugs (μWASP), RF Corona Discharge Ignition (RFCDI), and high-energy ignition (HEI) systems. Unlike the lean operation experiments, there are no experiments readily available in which the load or power was sacrificed to extend the EGR limit. Maximum possible EGR through the use of advanced ignition techniques generally decreases as the power density of the engine increases. Additionally, it seems from the available literature that only RFCDI and PND systems have been successfully used to extend the EGR limits of stable operation, and the literature regarding the use of μWASP techniques for this purpose is scarce. Nominally, the EGR limits of operation are their greatest when using PND ignition technologies, but experiments detailing operation at boosted loads are not currently available in the literature.

Techniques addressed in this dissertation

Of the advanced ignition techniques mentioned in this section, some of the most significant benefits in *both* lean and EGR limit extension in boosted 4-stroke gasoline engines have been observed using RFCDI and PND ignition systems. Furthermore, many of the recent experiments involving industrial collaborations examine RFCDI systems (Hampe et al., 2013; Schenk et al., 2015; Pineda, Wolk, Chen and Dibble, 2016), indicating that this particular ignition technique is a promising candidate for near-term implementation in automotive engines. In Chapter 3, an investigation of RFCDI in a research engine is presented, with specific attention paid to practical outcomes, such as fuel consumption and emissions reductions. In Chapter 4, an investigation of PND ignition in a constant volume chamber is presented, with specific attention paid to outcomes useful for the engine community.

Chapter 3

Corona discharge ignition

This chapter is based on research previously published in the *SAE International Journal of Engines* (Pineda, Wolk, Chen and Dibble, 2016) and presented at the *2016 Spring Technical Meeting of the Western States Section of the Combustion Institute* (Pineda, Chen and Dibble, 2016). The study is a highly applied investigation in a single cylinder research engine and thus focuses on practical outcomes, such as fuel consumption and emissions decreases relative to an established state-of-the-art baseline.

3.1 Introduction

The non-equilibrium plasma-assisted ignition (PAI) technique explored in this chapter is corona discharge ignition, in which a single negative electrode in the combustion chamber receives a very large and very fast negative voltage pulse or series of pulses controlled by an alternating current (AC) field. As mentioned in Section 2.5, researchers have investigated RF corona discharge ignition in different engine experiments. Some additional experiments include those with two-stroke SI engines (Hampe et al., 2015) as well as GDI four-stroke engines at loads associated with naturally aspirated (Hampe et al., 2013; Briggs et al., 2014; Mariani and Foucher, 2014; Schenk et al., 2015) and boosted (Hampe et al., 2013; Schenk et al., 2015) conditions, in the latter case (Schenk et al., 2015) with the ability to extend the EGR limits to around 24% at the most boosted conditions (1400 kPa BMEP, 2000 rpm), though the EGR limit extension had the greatest effect at loads corresponding to naturally aspirated conditions (200 kPa BMEP, 2000 rpm). In both of the studies examining boosted conditions (Hampe et al., 2013; Schenk et al., 2015), the lean limit for gasoline combustion was extended from $\phi \approx 0.74$ to $\phi \approx 0.63$.

In this chapter, we examine the extension of practical operating EGR limits in boosted and high speed conditions using RF corona discharge ignition, focusing on the changes in brake-specific fuel consumption (bsfc) and changes in brake-specific emissions relative to the optimum EGR conditions for which inductive spark ignition engine operation is practical. Specific attention is paid to changes in brake-specific fuel consumption (BSFC) and changes

Table 3.1: Engine specifications for Ricardo "Hydra" SCRE.

Displaced volume	500 cc
Stroke	90 mm
Bore	84 mm
Compression ratio	10.3:1
Number of valves	4 (Dual, Variable Valve Timing)

in brake-specific emissions. These metrics are usually reported in mass of fuel used or mass of pollutant created per amount of useful energy produced (Heywood, 1988), respectively. For this investigation, "optimum baseline spark ignition operation" for a given engine speed and load is a specific set of valve, injection, and ignition timing at a specific EGR rate that minimizes specific fuel consumption. BSFC and emission data are presented as relative changes from this optimum SI baseline because a proprietary engine and fuel architecture were used for the tests in this study.

First, the setup of the experiment and the operating procedure are outlined. Then, the results are presented, followed by a discussion. The results are divided into two separate sections for different "key test points" corresponding to the engine speed and loading: Moderate speeds with naturally aspirated loads (2000 rpm, 800 kPa BMEP) and moderate speeds with boosted loads (2000 rpm, 2000 kPa BMEP). An additional high speed and boosted load test point (4000 rpm, 2000 kPa) was also conducted but is not discussed here, since the stoichiometry of that operating point was $\phi > 1$ and is not relevant to the near-term implementation in automotive engines as discussed at the end of Chapter 1. Further information on this testing point can be found in the paper by Pineda, Wolk, Chen and Dibble (2016). Within each of these conditions, the results are further divided into three sections. The first of these briefly overviews the operating parameters for an EGR sweep conducted for the specified speed and loading. The second of these discusses and compares the combustion phasing of some operating points selected from the overview for both inductive SI operation and RFCDI operation. The last section compares processes summary data including cycle-to-cycle variation, brake-specific fuel consumption and brake-specific emissions for the same selected operating points.

3.2 Experimental setup and procedure

Equipment and measurement

Piston-cylinder assembly and manifolds

For this investigation, a 4-stroke direct injection single cylinder research engine (SCRE, Ricardo "Hydra" crankcase) was used. Table 3.1 lists the engine specifications. This piston had a bowl to aid in fuel-air mixing, and both the fuel injector and ignitor (both traditional inductive spark or corona ignitor) were located near the center of the top of the cylinder

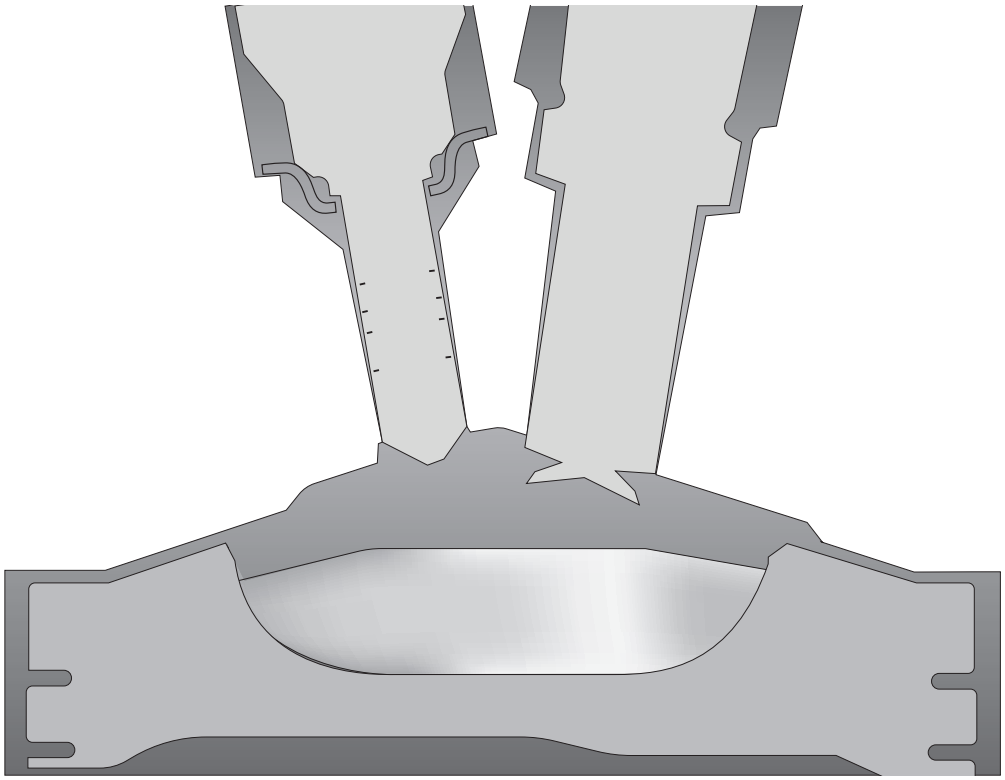

Figure 3.1: Representative cross section of piston / cylinder assembly through fuel injector (left) and four-pronged corona ignitor (right) adapted from Osborne et al. (2014) and King and Böcker (2013).

angled toward one another, between the four overhead valves (two inlet, two exhaust) with variable valve timing. Figure 3.1 shows a representative diagram of the piston-cylinder assembly with the RF corona ignitor and fuel injector, adapted from Osborne et al. (2014) and King and Böcker (2013). A Kistler 6043Asp pressure transducer recorded the instantaneous in-cylinder pressure and corresponding crank angle degree (0.5 °CA resolution) with an uncertainty of 0.2 bar (specified by the manufacturer) and an A& D Phoenix RT combustion analysis system encoded the signals. Thermocouples placed immediately ahead of and after the intake and exhaust valves recorded the mean intake and exhaust manifold temperatures, respectively, with a manufacturer-specified accuracy of 3 °C. Mean fuel flow to the fuel injector was controlled by an AVL 733S Fuel Balance and measured with a Micro Motion Coriolis meter with a specified accuracy of 0.8% of the flow rate. Mean air and exhaust flow to and from the manifolds was measured using an 8" H_2O differential pressure transducer, with a specified accuracy of 0.5% of the flow rate.

Dynamometer assembly

The engine was connected to an AC dynamometer (McClure HS255) via a drive shaft (Bailey Morris), and the torque was measured (HBM T40B) with an accuracy of 0.05% of the measured value. Corrected brake torque, brake power, and BMEP were calculated according to SAE J1349 (SAE International Surface Vehicle Standard, 2011).

Emissions

Mean emissions were measured with a Horiba MEXA-7100 DEGR Raw Gas Bench and sampled after the exhaust split for EGR. The uncertainties in the emissions measurements are calculated based on the manufacturer's error estimate as a percentage of the full scale of the range used for measurement, and the details for the individual species uncertainties are provided in Appendix C. As mentioned, the brake-specific emissions data are presented as relative changes because a proprietary engine and fueling architecture was used in these tests.

Ignition system

A traditional inductive spark ignition system was used for the baseline tests presented in this study to provide a basis of comparison for the RFCDI system. The inductive spark ignition system comprised a standard J-hook spark plug with a gap of 0.7 mm and a coil-on-plug type ignition coil. The electrode of the RF corona ignitor (Federal Mogul, Inc.) had four sharp points symmetrically spaced about its principal axis. Figure 3.2 provides a representative diagram. These four points generated the corona discharge in the chamber.

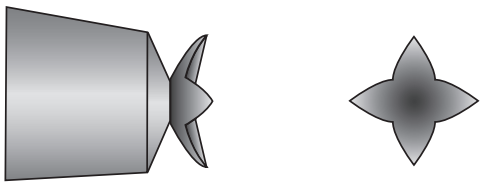

Figure 3.2: Representative diagram of the four-pronged corona ignitor used in this investigation.

The RFCDI system functioned similarly to others that have been developed (Heise et al., 2011; Hampe et al., 2013; Mariani and Foucher, 2014), both in using radio frequency waves to drive electrons in the charge and in that the circuitry of the system limits the overall current to the electrode, inhibiting the generation of an arc (spark). Instantaneous voltage

Table 3.2: Baseline key testing points with which to compare the corona discharge ignition results. The °CA convention assumed in this chapter uses TDC at 0 °CA

Key Test Point		1	2
EGR_{opt}	[%]	16 ± 1	10 ± 1
Speed	[rpm]	2000 ± 2	2000 ± 2
BMEP	[bar]	8.03 ± 0.5	19.78 ± 1.2
NMEP	[bar]	8.76 ± 0.5	20.39 ± 1.2
$\theta_{cam,intake}$	°CA	-241.2 ± 0.5	-271.4 ± 0.5
$\theta_{cam,exhaust}$	°CA	283 ± 0.5	255 ± 0.5
$\theta_{injection}$	°CA	334 ± 0.5	280 ± 0.5
Fuel Pressure	[bar]	140 ± 2	200 ± 1
$\theta_{ignition}$	°CA ATDC	-18.11 ± 0.5	1.98 ± 0.5
Equivalence Ratio	ϕ	1.01 ± 0.05	1.00 ± 0.05
CA50	°CA	6.85 ± 0.51	24.25 ± 0.51

and current measurements (0.5 °CA resolution) were recorded between the DC power supply of the corona ignitor and the DC-to-AC transformer that generated the RF electric field. We use these voltage and current measurements to estimate the total primary energy ("from the wall") required for the ignitor to generate and sustain the discharge for each cycle. While the resolution of these measurements is not sufficient for highly accurate calculations, it is good enough for comparing the energy requirements for different engine operating conditions.

Testing conditions

All experiments were performed using certification gasoline with a Research Octane Number (RON) of 98. For all the tests, the oil temperature was regulated to 90 ± 3 °C, the fuel temperature was regulated to 30 ± 3 °C, and the intake manifold temperature was regulated to 45 ± 3 °C. The intake air came from a temperature and pressure controlled air supply drawn from outdoors of the laboratory. The pressure was regulated with a compressor to meet boosting requirements, the temperature was regulated to 25 ± 3 °C, and the relative humidity was regulated to 30 ± 3%.

Experimental procedure

A series of baseline experiments with traditional inductive SI was completed such that a fair comparison to the RFCDI system performance could be made. We selected three "key test points" at both moderate and high speeds with low and high loading. Table 3.2 shows the operating parameters for these points. These three operating points represent the minimum specific fuel consumption practically possible with SI operation for the three engine speeds and loadings considered in this investigation. For each operating point, the valve, injection, and ignition timings were optimized successively with regards to specific fuel consumption: first, five different intake cam timings were tested to determine the optimum timing while holding exhaust valve timing, injection timing, and ignition timing constant. Then, five

different exhaust cam timings were tested with the optimum intake cam timing and other timings constant. After the optimization of the exhaust cam timing, these optimum settings were used similarly to determine the optimum injection timing, and then again this optimization procedure informed the optimization of the ignition timing. Table 3.2 shows these timings. For the naturally aspirated load EGR sweep, the ignition timings correspond to the maximum brake torque (MBT). For the boosted load EGR sweep, the ignition timings were advanced to the knock limit.

The net heat release rate (HRR) is calculated using Equation 3.1 (Heywood, 1988),

$$\text{HRR} = \frac{dQ_{net}}{d\theta} = \frac{\gamma}{\gamma - 1} P \frac{dV}{d\theta} + \frac{1}{\gamma - 1} V \frac{dP}{d\theta} \tag{3.1}$$

where crevice and other heat transfer terms are neglected, and all variables are functions of θ. The ratio of specific heats γ is calculated as a function of θ for each cycle (once for compression, γ_{comp}, and once for expansion, γ_{exp}) by calculating a least-squares linear fit of the natural log of P versus the natural log of V for the regions in which $\ln(P)$ vs. $\ln(V)$ is linear. For the part of the cycle during combustion with nonlinear behavior, a linear interpolation is made between γ_{comp} and γ_{exp}. The total net cumulative heat release is then obtained by integrating HRR over θ.

The resulting CA50 values from these operating parameters are given at the bottom of Table 3.2. In this chapter, CA50 is defined as the crank angle location in the cycle where 50% of the cumulative net heat release over the cycle is achieved (Heywood, 1988). Likewise, CA10 and CA90 are defined as the crank angle locations where 10% and 90% of the total cumulative heat release is achieved, respectively. Additionally, in this chapter, the flame development angle $\Delta\theta_d$ is defined as the number of crank angles between ignition and CA10, and the burning angle $\Delta\theta_b$ is defined as the number of crank angles between CA10 and CA90. The sum of these is referred to as the overall burning angle, $\Delta\theta_o$. These values are discussed in more detail in the combustion phasing part of Section 3.3.

The peak in-cylinder temperature for each cycle through the ideal gas relation is estimated using Equation 3.2:

$$T_{peak,est} = \frac{PV}{m_{ch} R} \tag{3.2}$$

where m_{ch} is the mass of the charge in the cylinder calculated from the measured air, fuel, and EGR mass flow rates and R is the specific gas constant for the mixture. This estimation does not factor in any crevice mass losses through blow-by and so the primary usefulness of this calculation is for comparison only.

For the RFCDI tests, corona ignitor parameters were also optimized for each engine operating condition; these parameters consisted of the corona duration and base voltage supply. Typically, the duration is longer at higher EGR rates, and the supply voltage is higher for higher loading. The optimization resulted in effectively increasing the ignition energy as much as possible without excessive arcing—that is, the percentage of cycles with arc events detected was limited to below 10%. Each experiment consisted of recording the data described for 300 consecutive engine cycles at steady-state.

The definition of EGR rate given in Equation 2.18 in Chapter 2 is reproduced here in Equation 3.3 for reader convenience, and provides the cooled EGR rate in this study.

$$\text{EGR } (\%) = \frac{X_{\text{CO}_2,\text{ intake}} - X_{\text{CO}_2,\text{ ambient}}}{X_{\text{CO}_2,\text{ exhaust}} - X_{\text{CO}_2,\text{ ambient}}} \tag{3.3}$$

As before, in Equation 3.3, $X_{\text{CO}_2,i}$ represents the mole fraction of CO_2 in the intake and exhaust mixtures, and the ambient CO_2 concentration outside of the laboratory was recorded as 330 ppm. The EGR rate in Table 3.2 corresponds to the optimum EGR rate for that engine speed and loading—that is, the EGR rate (with optimized timings) which minimizes fuel consumption for inductive SI operation, and for which the coefficient of variation of indicated mean effective pressure (COV_{IMEP}) is less than 3% during engine operation (Heywood, 1988):

$$\text{COV}_{\text{IMEP}} = 100 \times \frac{\sigma_{\text{IMEP}}}{\mu_{\text{IMEP}}} < 3\% \tag{3.4}$$

For this investigation, in Equation 3.4, μ_{IMEP} is the mean IMEP over 300 cycles, and σ_{IMEP} is the standard deviation of IMEP over the same 300 cycles. A high COV_{IMEP} is indicative of unstable operation and is undesirable in automotive engine applications.

3.3 Results

In these results, the combustion phasing of certain baseline SI and RFCDI operating points is discussed in more detail. In the tables and plots that follow, these points are highlighted with specific colors for clarity. The black open markers/lines correspond to the optimum baseline SI operating points shown in Table 3.2. The red open markers/ lines correspond to RFCDI operation at the same EGR rate as that optimum baseline SI operation. The blue open markers and lines correspond to the optimum RFCDI operating point determined in this study. The optimum RFCDI operating point is defined as the EGR rate which minimizes specific fuel consumption while keeping COV_{IMEP} lower than 3%.

Additionally, plots of brake-specific fuel consumption, estimated peak in-cylinder pressure, and brake-specific emissions are presented alongside each other. While some cursory explanation is provided to relate the three in this section for facilitating reading and drawing attention to the plots, the bulk of the analysis for all of the results is presented in Section 3.4.

The BSFC and emissions results for the RFCDI operation are reported as percentage change from the optimum baseline SI operating point:

$$\Delta\%(\text{EGR}) = 100 \times \frac{\text{RFCDI}(\text{EGR}) - \text{SI}(\text{EGR}_{opt})}{\text{SI}(\text{EGR}_{opt})} \tag{3.5}$$

where the SI operation at EGR_{opt} corresponds to the operating point in Table 3.2. For all reported values with uncertainties, the details of the uncertainty calculations are given in Appendix C.

Table 3.3: Operating parameters for the 2000 rpm / 800 kPa BMEP RFCDI tests for different EGR rates examined. Uncertainties are the same for Key Test Point 1 in Table 3.2 but are omitted to save space, except for the CA50 values. Selected points that are discussed in more detail throughout this chapter are highlighted with color: 16% EGR (blue) and 25% EGR (gold).

EGR	[%]	**16.3**	19.6	**24.9**	28.0
Speed	[rpm]	**2000**	2000	**2000**	2000
BMEP	[bar]	**7.86**	7.82	**7.84**	7.75
NMEP	[bar]	**8.75**	8.71	**8.79**	8.70
$\theta_{cam,intake}$	°CA	**−241.3**	−241.3	**−241.4**	−241.3
$\theta_{cam,exhaust}$	°CA	**283.6**	283.6	**283.5**	283.5
$\theta_{injection}$	°CA	**334**	334	**334**	334
Fuel Pressure	[bar]	**140**	140	**140**	140
Intake Pressure	[bar]	**1.07**	1.11	**1.13**	1.16
$\theta_{ignition}$	°CA ATDC	**−16.58**	−19.66	**−26.50**	−34.54
Equivalence Ratio	ϕ	**1.01**	1.01	**1.01**	1.02
CA50	°CA	**7.0 ± 0.5**	6.5 ± 0.5	**6.1 ± 0.5**	6.6 ± 0.6
$\dot{m}_{fuel}$	[%]	**−0.97%**	−1.81%	**−3.27%**	−3.60%

Moderate speeds and naturally aspirated loading conditions

This subsection presents results for moderate engine speeds and loads associated with naturally aspirated operation.

Overview of operating parameters for EGR sweep

Table 3.3 shows an overview of the operating parameters similar to those in Table 3.2 for the EGR sweep of the moderate speed and naturally aspirated loading tests. To facilitate understanding of results that follow, the percentage change in fuel mass flow relative to Key Test Point 1 (2000 rpm / 800 kPa BMEP / 16% EGR) is also provided in Table 3.3. Most of the parameters were unchanged across EGR rates, with the significant exceptions being the ignition timing θ_{ign}, intake pressure P_{int}, and fuel mass flow, $\dot{m}_{fuel}$. For an EGR rate of 16%, the ignition timing was retarded slightly (by 2.2 ± 1.0 °CA) from the 16% EGR baseline SI operation in Table 3.2 to obtain MBT. At higher EGR rates, the ignition timing required advancement (by 7.8 ± 1.0 °CA) from the 16% EGR baseline SI operation to obtain MBT. The CA50 values remained relatively unchanged for most of the EGR rates relative to the baseline optimum SI case.

Combustion phasing

For moderate speeds and naturally aspirated loads (2000 rpm / 800 kPa BMEP), the RFCDI system enabled high EGR (up to 25%) operation with an earlier pressure rise, shown in Figure 3.3 alongside the net HRR and cumulative net heat release. Lower HRR is observed for the 25% EGR condition in part due to the reduced fueling shown in Table 3.3, and on average this led to less cumulative net heat release, though uncertainties preclude a

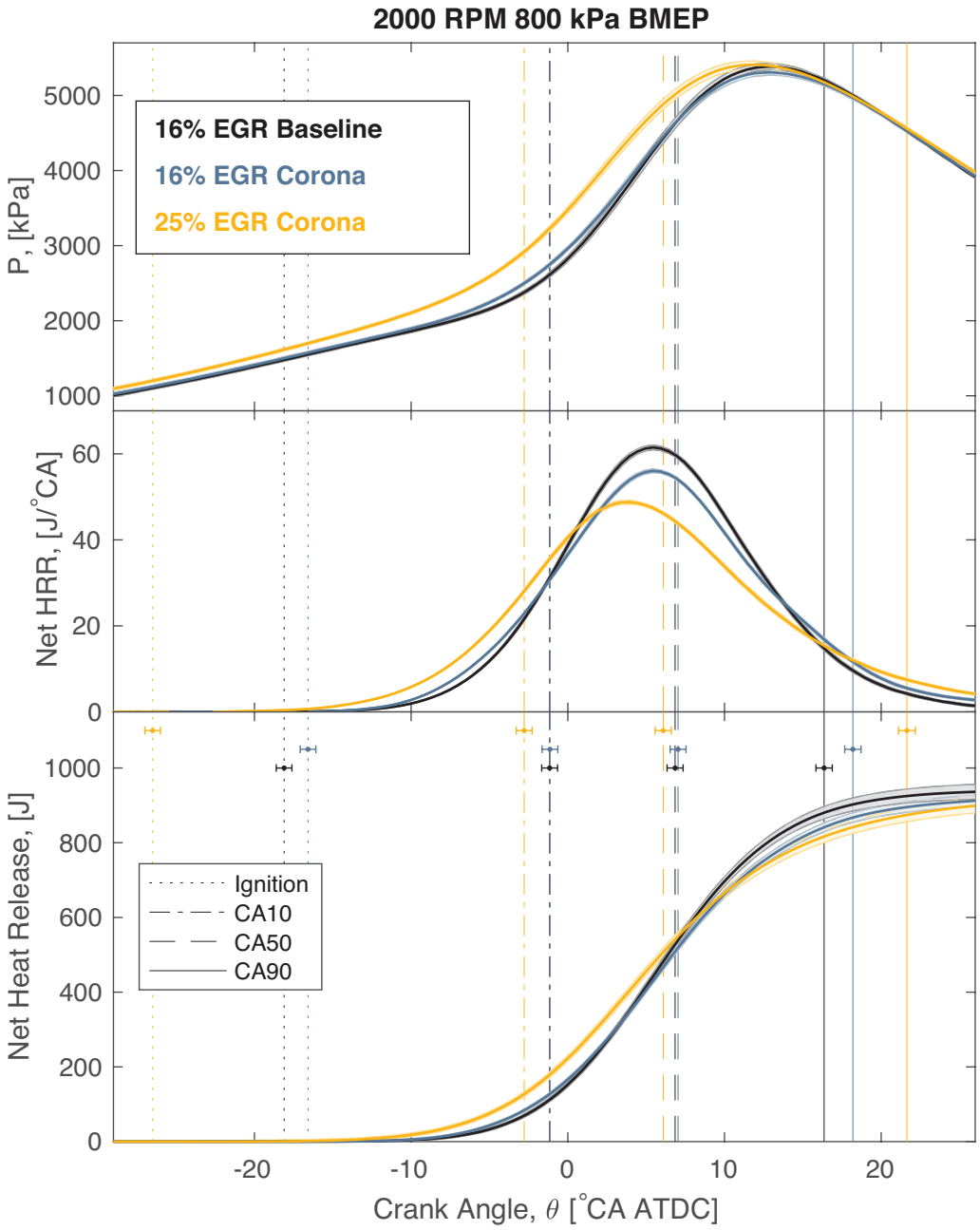

Figure 3.3: Combustion phasing plots shown for selected EGR conditions for the 2000 rpm / 800 kPa BMEP tests as a function of crank angle degree: Pressure (top), net HRR (middle), and cumulative net heat release (bottom). $\phi = 1 \pm 0.05$ for all operating points shown. The shaded regions depict the uncertainty in the values plotted. EGR conditions shown are: 16% EGR with traditional inductive SI (black), 16% EGR with RFCDI (blue), and 25% EGR with RFCDI (gold). Crank angle locations of both ignition and fractional net heat release are the vertical lines in the figure, with uncertainties as shown as horizontal error bars.

definitive conclusion based on these data alone. Though the RFCDI system lowered the flame development angle $\Delta\theta_d$ for the 16% EGR operating point, the ignition timing required substantial advancement at 25% EGR. The CA50 did not significantly advance (by 0.7 ± 1.0 °CA) relative to the 16% EGR baseline SI case.

Figure 3.4 plots burn duration angles against EGR rate for the 2000 rpm / 800 kPa BMEP tests for RFCDI operation and baseline SI operation. In general, the RFCDI system reduced the overall burning angle $\Delta\theta_o$ for each EGR rate, but more significantly in the flame development angle $\Delta\theta_d$ than the burning angle $\Delta\theta_b$. At 16% EGR, $\Delta\theta_b$ from the RFCDI system was actually larger than $\Delta\theta_b$ from the optimum baseline spark ignition operation, but this was the exception rather than the rule for the 2000 rpm / 800 kPa BMEP tests. For the optimum RFCDI operating point at 25% EGR, $\Delta\theta_d$ reduced by 5.6 ± 1.0 °CA compared to traditional SI, and $\Delta\theta_b$ reduced by 2.7 ± 1.0 °CA.

Cycle-to-cycle variability, brake-specific fuel consumption, and emissions

Figure 3.5 shows a plot of $\mathrm{COV_{IMEP}}$ for RFCDI operation across the range of EGR rates for the 2000 rpm / 800 kPa BMEP tests along with the values for the corresponding baseline inductive SI operation, shown with open markers for comparison. Overall, using the RFCDI system did not have a significant effect on the $\mathrm{COV_{IMEP}}$ for all EGR rates tested except for the highest EGR rate (28%), indicating that any combustion stabilization resulting from using the RFCDI system is more nuanced than can be determined from $\mathrm{COV_{IMEP}}$ alone. More detail for this is provided in Section 3.4. Figure 3.6 shows plots of changes in BSFC, averages of estimated peak in-cylinder temperatures $T_{peak,est}$, and changes in brake-specific emissions (relative to the 16% EGR baseline SI test) for the RFCDI 2000 rpm / 800 kPa BMEP tests. The RFCDI system extended the maximum practical EGR rate and slightly reduced BSFC (up to 2.1 ± 0.7 % lower than the optimum SI baseline 16% EGR operation) for some of the higher EGR conditions. Brake-specific emissions generally either decreased or stayed the same as the EGR rate increased, with the notable exception being the HC and the CO emissions for the 28% EGR rate. At this EGR rate, the overall burning angle $\Delta\theta_o$ was much larger than in the baseline 16% EGR SI case (56.8 ± 1.0 °CA vs. 34.5 ± 1.0 °CA); combustion was likely so slow in this case that the reactions could not completely oxidize the fuel to CO_2 before the cycle exhausted the gases. A small decrease in the brake-specific CO_2 emissions at this operating point supports that explanation. For the 16% and 20% EGR cases, however, brake-specific CO emissions decreased (by 20.0 ± 1.6% and 21.7 ± 1.6%, respectively) while CO_2 emissions increased a small amount (by 0.6 ± 0.2% and 0.3 ± 0.2%, respectively), suggesting more complete combustion.

At 25% EGR, a 73.3 ± 0.1% reduction in brake-specific $\mathrm{NO_X}$ relative to the optimum baseline SI operation at 16% EGR is observed, without significant change in brake-specific CO and HC emissions. An examination of the average of estimated peak in-cylinder temperatures $T_{peak,est}$ in Figure 3.6 reveals a 165 ± 98 K reduction in $T_{peak,est}$ relative to the optimum baseline SI operation (outlined in black), this reduction in peak in-cylinder temperatures likely drove the reduction in $\mathrm{NO_X}$ emissions.

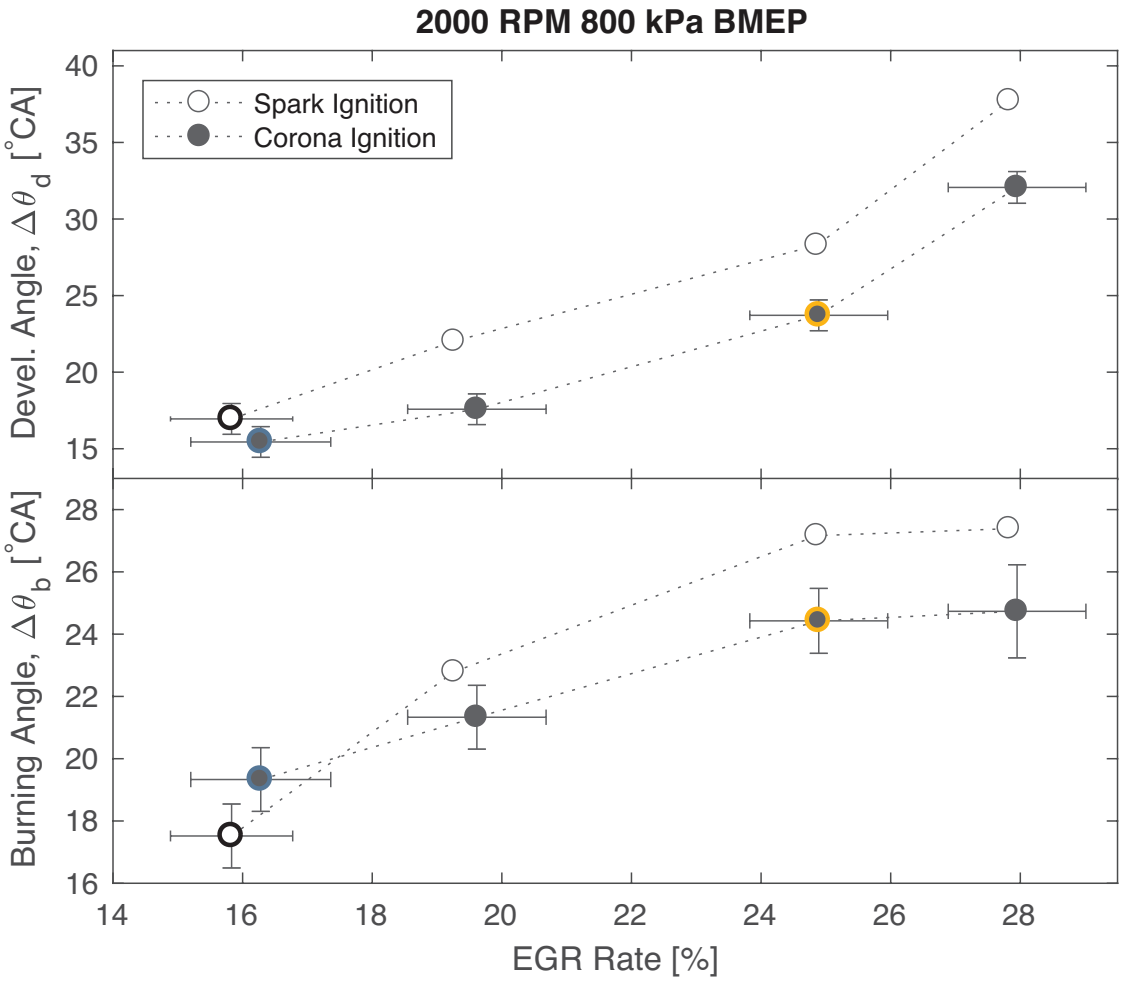

Figure 3.4: Plots of burn duration for the 2000 rpm / 800 kPa BMEP tests. Baseline SI operation is shown with open markers and RFCDI operation is shown with filled markers. $\phi = 1 \pm 0.05$ for all operating points shown. Flame development angle $\Delta\theta_d$ (top) and burning angle $\Delta\theta_b$ (bottom). The operating points shown in Figure 3.3 are highlighted with colored outlines: 16% EGR inductive SI (black), 16% EGR RFCDI (blue), and 25% EGR RFCDI (gold).

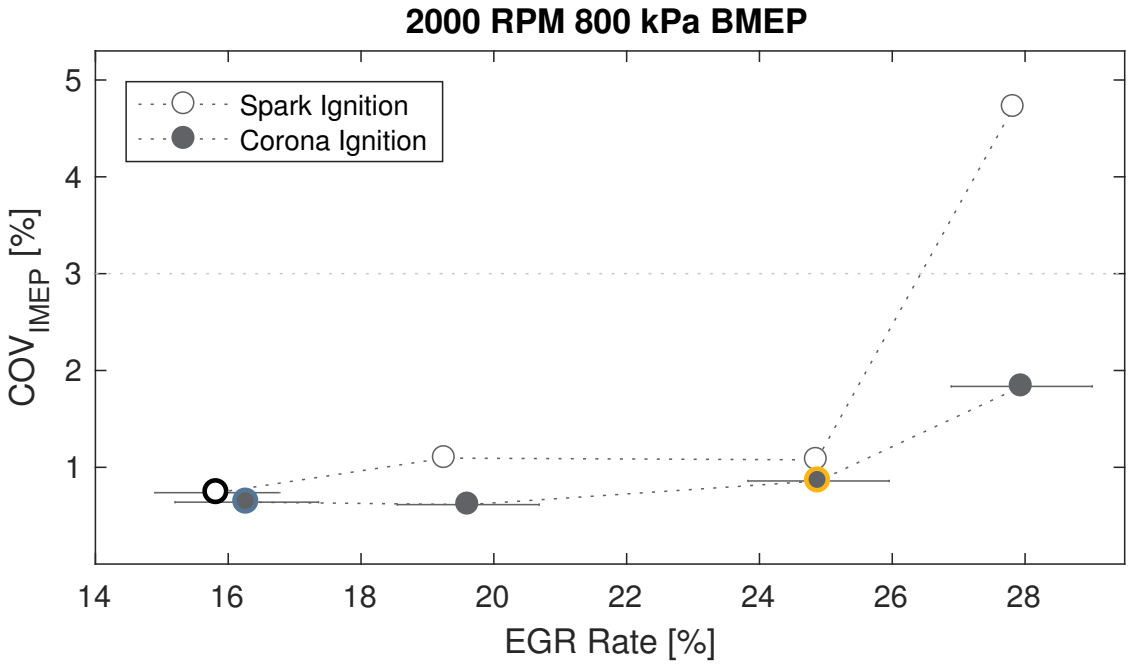

Figure 3.5: Plot of COV_{IMEP} for the 2000 rpm / 800 kPa BMEP tests. $\phi = 1 \pm 0.05$ for all operating points shown. The operating points shown in Figure 3.3 are highlighted with colored circles: 16% EGR inductive SI operation (black), 16% EGR RFCDI operation (blue), and 25% EGR RFCDI operation (gold).

Moderate speeds and boosted loading conditions

This section presents results for moderate engine speeds and loads associated with boosted or turbocharged operation.

Overview of operating parameters for EGR sweep

Table 3.4 gives an overview of the operating parameters for the EGR sweep of the moderate speed and boosted loading tests. As with the 2000 rpm / 800 kPa BEMP tests, most of the parameters remain unchanged across the EGR rates; the significant exceptions being the ignition timing θ_{ign} and change in fuel mass flow $\dot{m}_{fuel}$. In conjunction with the decreased likelihood of knock that typically occurs with increased EGR (Hoepke et al., 2012), it was observed that the RFCDI system reduced the occurrence of engine knock for the tested EGR rates of 10% to 15%, allowing for a small advancement of the ignition timing to extract more work from each cycle. Table 3.5 shows the ignition timing in more detail across all EGR rates in Table 3.4 for both SI operation and RFCDI operation. The benefits of advancing the combustion phasing are more substantial under the boosted conditions of the 2000 rpm / 2000 kPa BEMP tests than under the naturally aspirated conditions of the 2000 rpm / 800 kPa BMEP tests, where the ignition timing was already near-optimal. Overall, the RFCDI system extended the maximum practical EGR rate from 10% to 15%.

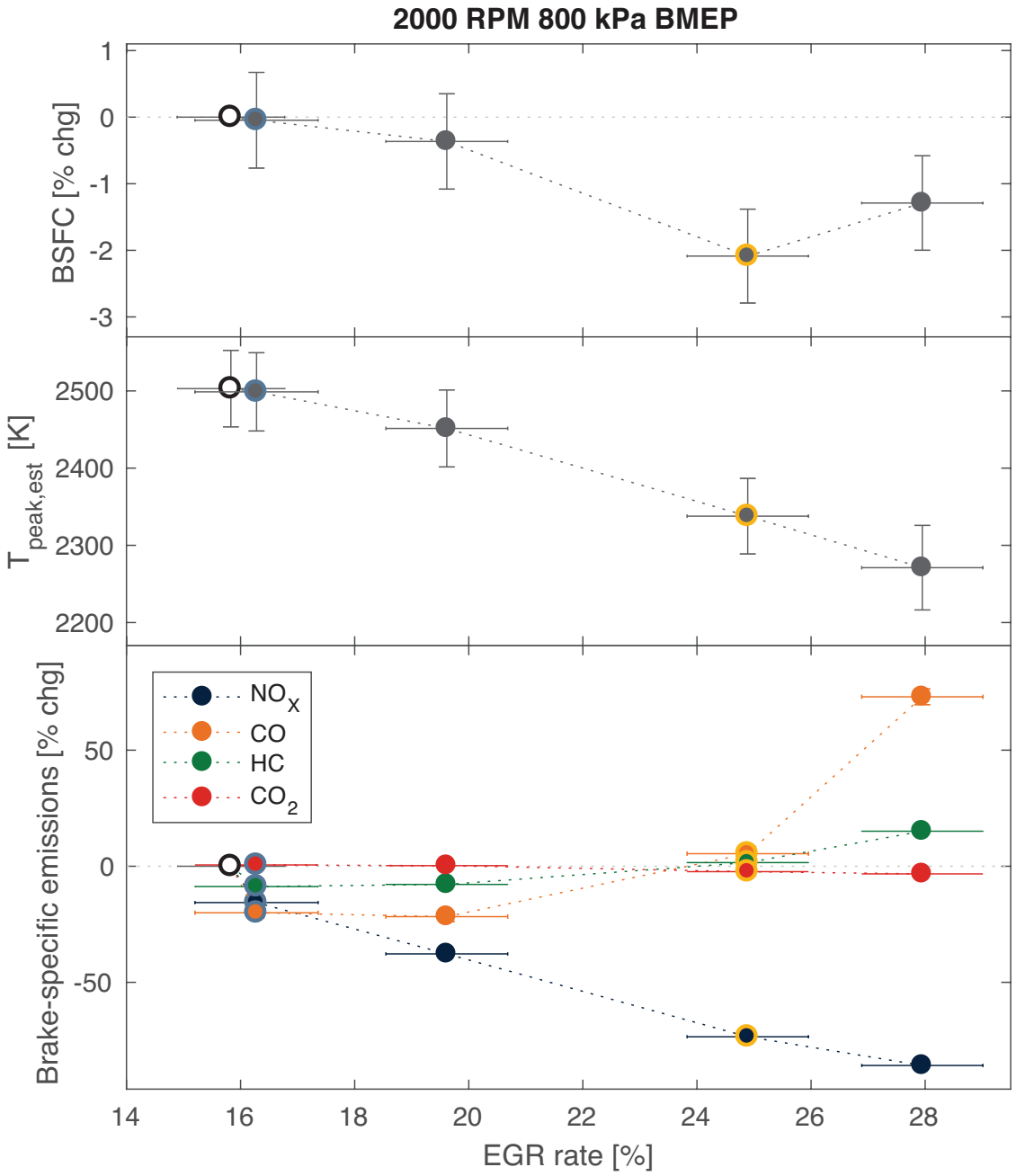

Figure 3.6: Changes in brake-specific fuel consumption (top), average of estimated peak in-cylinder temperatures (middle), and changes in brake- specific emissions (bottom) for the 2000 rpm / 800 kPa BMEP tests. $\phi = 1 \pm 0.05$ for all operating points shown. For BSFC and emissions, all RFCDI points are plotted as percentage change from the optimum baseline SI operation marked with black circles. The operating points shown in Figure 3.3 are highlighted with colored circles: 16% EGR RFCDI operation (blue), and 25% EGR RFCDI operation (gold).

Table 3.4: Operating parameters for the 2000 rpm / 2000 kPa BMEP RFCDI tests for different EGR rates examined. Uncertainties are the same for Key Test Point 2 in Table 3.2 but are omitted to save space, except for the CA50 values. Selected points that are discussed in more detail throughout this chapter are highlighted with color: 10% EGR (blue) and 15% EGR (gold).

EGR	[%]	**10.2**	11.8	**14.9**	19.6
Speed	[rpm]	**2000**	2000	**2000**	2000
BMEP	[bar]	**19.30**	19.44	**18.19**	17.78
NMEP	[bar]	**20.44**	20.36	**20.41**	20.17
$\theta_{cam,intake}$	°CA	**−271.1**	−271.0	**−270.4**	−270.5
$\theta_{cam,exhaust}$	°CA	**255.7**	255.8	**255.6**	255.7
$\theta_{injection}$	°CA	**280.0**	280.0	**280.0**	280.0
Fuel Pressure	[bar]	**200**	200	**200**	200
Intake Pressure	[bar]	**1.94**	1.96	**1.94**	1.98
$\theta_{ignition}$	°CA ATDC	**1.00**	0.00	**−3.50**	−5.49
Equivalence Ratio	ϕ	**1.01**	0.99	**1.00**	1.00
CA50	°CA	**22.7 ± 0.5**	23.8 ± 0.5	**20.6 ± 0.5**	23.1 ± 0.9
$\dot{m}_{fuel}$	[%]	**−2.56%**	−2.58%	**−9.93%**	−8.95%

Table 3.5: Ignition timings for the 2000 rpm / 2000 kPa BMEP tests for different EGR rates examined for both RFCDI and SI operation.

EGR	[%]	10 ± 1	12 ± 1	15 ± 1	20 ± 1
SI θ_{ign}	°CA	**1.98**	1.37	−2.37	−6.37
RFCDI θ_{ign}	°CA	**1.00**	0.00	**−3.50**	−5.49

Combustion phasing

For the 2000 rpm / 2000 kPa BMEP tests, the RFCDI system enabled higher EGR operation with earlier average pressure rise, shown in Figure 3.7. From the baseline SI 10% EGR case to the RFCDI 10% EGR case, this resulted from an advance in the location of the net HRR (which advanced the CA50 by 1.6 ± 1.0 °CA), though the peak net HRR remained similar. Achieving the same loading required a lower net HRR (and subsequently less cumulative net heat release) for the RFCDI 25% EGR case, likely partly due to the reduced fuel mass flow (-9.93%) shown in Table 3.4. The CA50 advanced farther (by 3.6 ± 1.0 °CA) from the baseline SI 10% EGR case. Additionally, as the combustion phasing advanced, the required intake pressure to achieve 2000 kPa BMEP decreased, evident in the lower initial pressures in both Figure 3.7 and Table 3.4. Figure 3.8 plots the burn duration angles for the 2000 rpm / 2000 kPa BMEP tests for both RFCDI operation and baseline SI operation as functions of EGR rate. Like the 2000 rpm / 800 kPa BMEP tests, the RFCDI system reduced the flame development angles $\Delta\theta_d$, although not as much and less definitely due to greater cycle-to-cycle variation at boosted loads. Conversely, the system generally increased burning angles $\Delta\theta_b$ relative to baseline spark ignition operation, erasing the gains made from decreasing $\Delta\theta_d$. For the optimum RFCDI operation at 15% EGR, $\Delta\theta_d$ reduced by 1.8 ± 1.0 °CA, and $\Delta\theta_b$ increased by 1.3 ± 1.1 °CA. Regardless, the combustion phasing still advanced enough

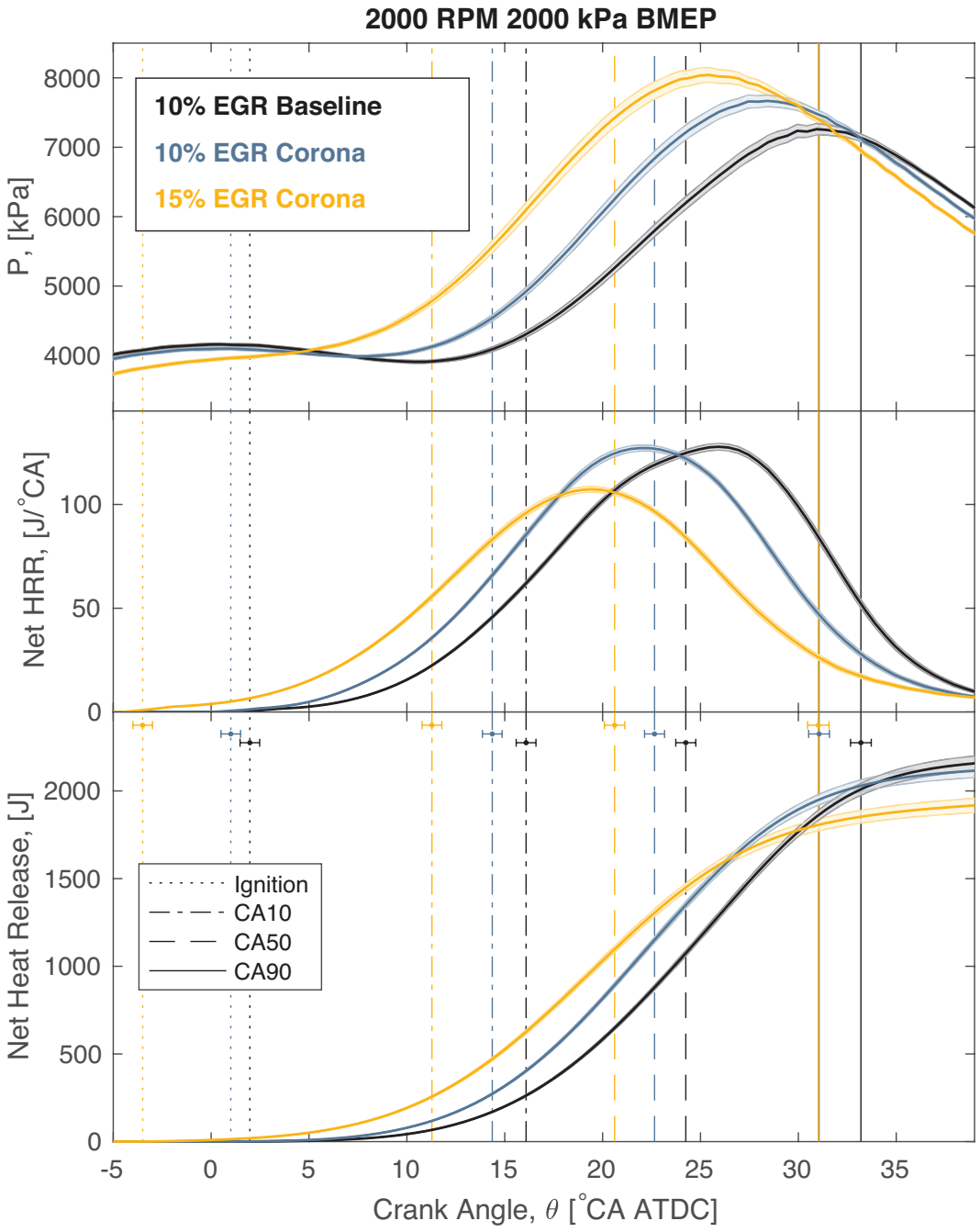

Figure 3.7: Combustion phasing plots shown for selected EGR conditions for the 2000 rpm / 2000 kPa BMEP tests as a function of crank angle degree: Pressure (top), net HRR (middle), and total cumulative net heat release (bottom). $\phi = 1 \pm 0.05$ for all operating points shown. The shaded regions depict the uncertainty in the values plotted. EGR conditions shown are: 10% EGR with traditional inductive SI (black), 10% EGR with RFCDI (blue), and 15% EGR with RFCDI (gold). Crank angle locations of both ignition and fractional charge burn are shown as vertical lines throughout the figure, with uncertainties shown as horizontal error bars.

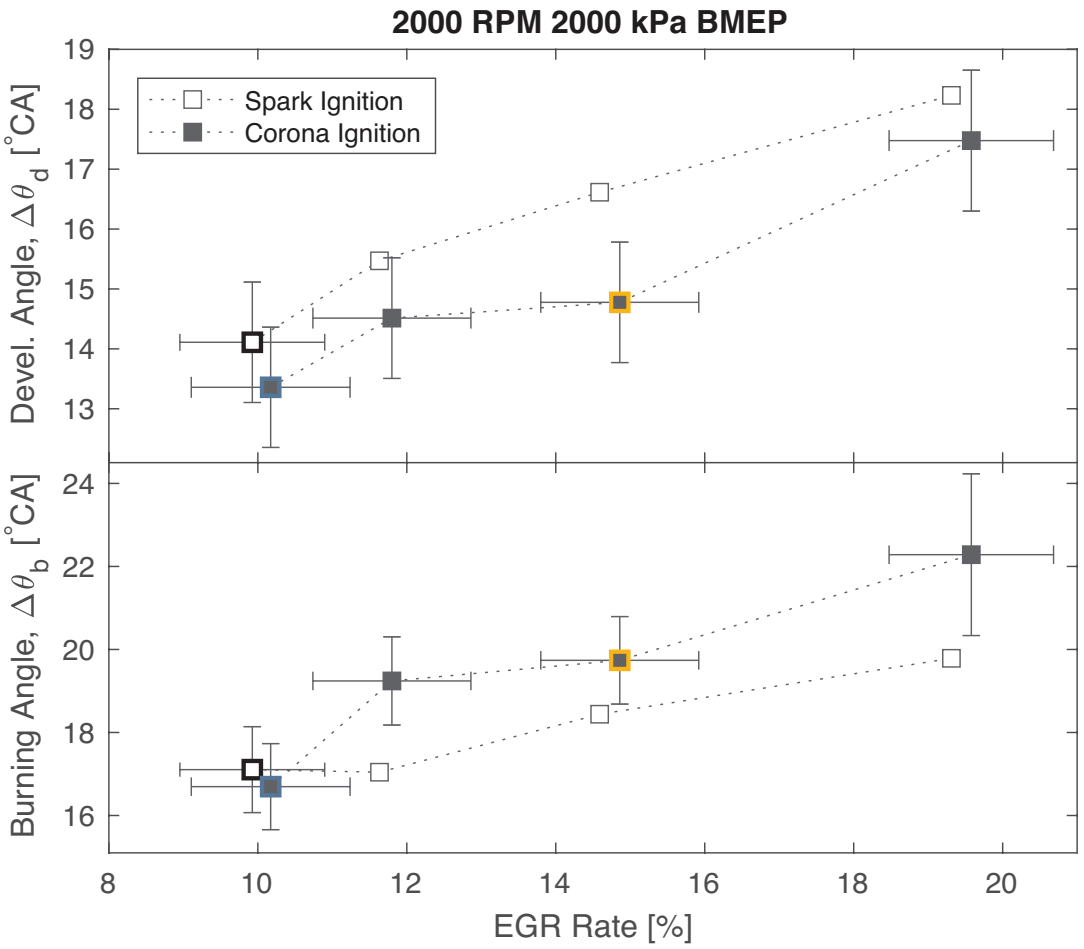

Figure 3.8: Plots of burn duration for the 2000 rpm / 2000 kPa BMEP tests. Baseline SI operation is shown with open markers and RFCDI operation is shown with filled markers. Flame development angle $\Delta\theta_d$ (top) and burning angle $\Delta\theta_b$ (bottom). $\phi = 1 \pm 0.05$ for all operating points shown. For clarity, the operating points discussed in Figure 3.7 are highlighted with colors: 10% EGR inductive SI operation (black), 10% EGR RFCDI operation (blue), and 15% EGR RFCDI operation (gold).

such that the average CA10, CA50, and CA90 all advanced relative to the optimum baseline SI operation at 10% EGR, as shown in Figure 3.7.

Cycle-to-cycle variability, brake-specific fuel consumption, and emissions

Figure 3.9 shows a plot of COV_{IMEP} for several operating points across the range of EGR rates for the 2000 rpm / 2000 kPa BMEP tests for both baseline SI operation and RFCDI operation. Like in the 2000 rpm / 800 kPa BMEP tests, the RFCDI did not definitely reduce COV_{IMEP} in the 2000 rpm / 2000 kPa BMEP tests. Additionally, for the highest EGR rate tested (20%), the COV_{IMEP} increased relative to the baseline SI condition. As with the 2000 rpm / 800 kPa BMEP tests, we present a more nuanced explanation of

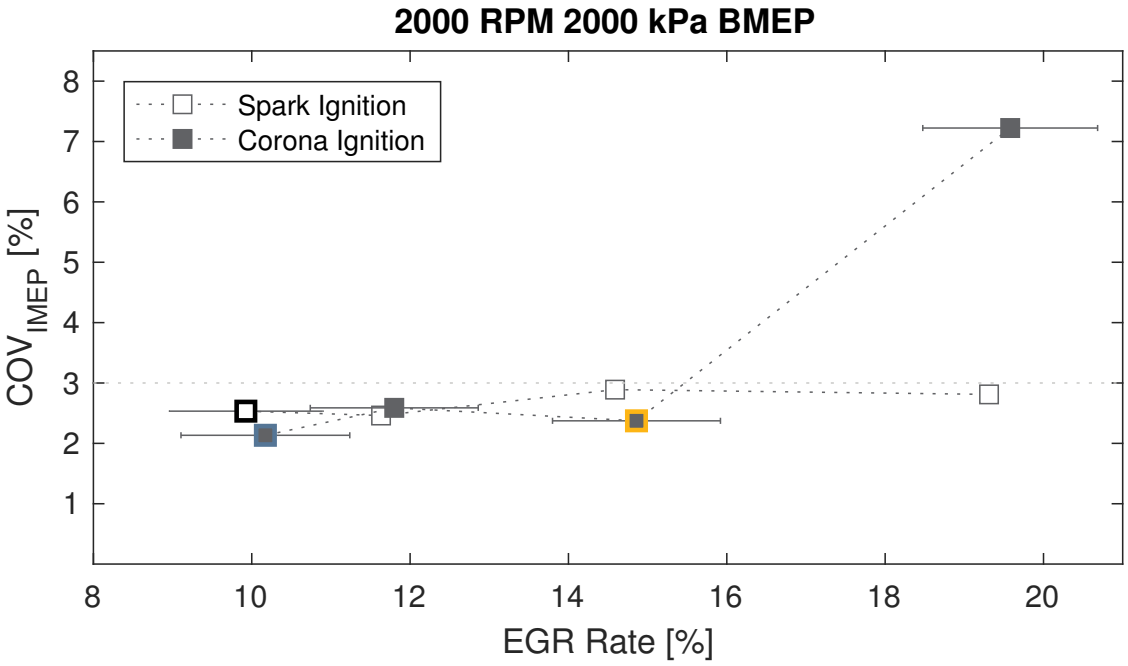

Figure 3.9: Plot of COV_{IMEP} for the 2000 rpm / 2000 kPa BMEP tests. $\phi = 1 \pm 0.05$ for all operating points shown. The operating points shown in Figure 3.7 are highlighted with colored squares: 10% EGR inductive SI operation (black), 10% EGR RFCDI operation (blue), and 15% EGR RFCDI operation (gold).

the cycle to cycle variability in Section 3.4. Figure 3.10 shows plots of changes in BSFC, average of estimated peak temperatures, and changes in brake-specific emissions for the 2000 rpm / 2000 kPa BMEP tests. Definite decreases in BSFC (up to $4.4 \pm 0.7\%$ for the 15% EGR RFCDI case) were observed for all EGR rates examined. Unlike in the 2000 rpm / 800 kPa BMEP tests, there is no definitive trend for the average estimated peak in-cylinder temperature $T_{peak,est}$ across EGR rate, though the overall combustion phasing advancement that generated the higher average pressures seen in Figure 3.7 was likely a compounding factor in keeping $T_{peak,est}$ from decreasing even though the EGR rate was increasing. Despite the lack of a definite decrease in $T_{peak,est}$, we observed a substantial (though less substantial than in the 2000 rpm / 800 kPa BMEP tests) decrease in brake-specific NO_X emissions ($29.0 \pm 0.1\%$) relative to the optimum baseline SI operation for the optimum RFCDI case with an EGR rate of 15%. Likewise, CO emissions reduced by up to $36.4 \pm 1.5\%$ (for the EGR rate of 12%), and HC emissions reduced by up to $9.9 \pm 0.2\%$ (for the EGR rate of 10%). Brake-specific CO_2 emissions decreased across all EGR rates, most significantly at an EGR rate of 15%, where the decrease was $4 \pm 0.2\%$. At this EGR rate, both CO and HC emissions also decreased relative to the baseline SI condition, and so this decrease in brake-specific CO_2 was likely due to an overall increase in fuel efficiency, evident by the changes in BSFC.

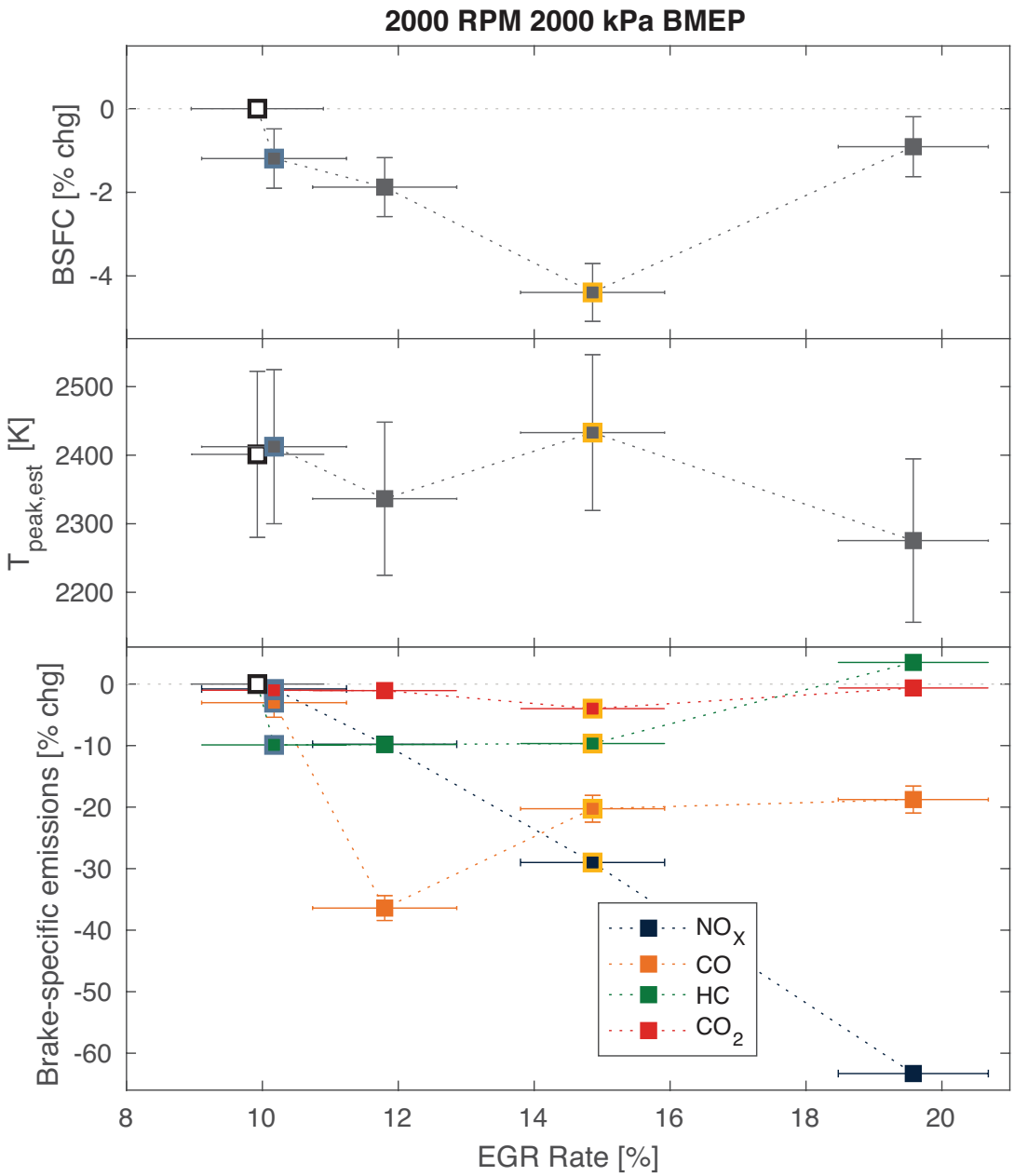

Figure 3.10: Changes in brake-specific fuel consumption (top), average of estimated peak in-cylinder temperatures (middle), and changes in brake- specific emissions (bottom) for the 2000 rpm / 2000 kPa BMEP tests. $\phi = 1 \pm 0.05$ for all operating points shown. For BSFC and emissions, all RFCDI points are plotted as percentage change from the optimum baseline SI operation marked with black squares. The operating points shown in Figure 3.3 are highlighted with colored squares: 10% EGR RFCDI operation (blue), and 15% EGR RFCDI operation (gold).

3.4 Discussion

The purpose of alternative ignition strategies in engines is to beneficially alter the early behavior of the developing flame kernel so that more robust combustion occurs. The RFCDI system largely achieved this purpose, through distinct but beneficial pathways at each of the different engine speed and loading combinations we examined. The ramifications of this are discussed for the individual operating points in the subsections that follow.

Moderate speeds and naturally aspirated loads

The RFCDI system stabilized combustion at high EGR rates for the 2000 rpm / 800 kPa BMEP tests, keeping the COV_{IMEP} below 3% up to 28% EGR, with the minimum BSFC observed at an EGR rate of 25%. However, for EGR rates of 25% and below, the RFCDI system did not strongly affect the COV_{IMEP}, but this does not mean that there was no effect on cycle-to-cycle variability. To better understand the impact of the RFCDI system on the cycle-to-cycle variability, a scatterplot was generated along with associated histograms comparing the maximum pressure for each cycle and crank angle for that maximum pressure, shown in Figure 3.11 for both of the 16% EGR operating points. Figure 3.11 depicts the SI operation in black and the RFCDI operation in blue. A darker blue color indicates where the data overlap. The histograms on the y-axis show the relative frequency of maximum pressures P_{max} across all 300 cycles with bin widths of 200 kPa, while the histograms on the x-axis show the relative frequency of crank angle where P_{max} occurred, $\theta_{P_{max}}$, with bin widths of 0.5 °CA. As is typical (Heywood, 1988), there is a correlation between $\theta_{P_{max}}$ and P_{max}. However, it is clear that using the RF corona discharge ignition system reduced the variability in $\theta_{P_{max}}$ (though the mean value does not significantly change), and generally reduced P_{max}, though a slight decrease in variability of P_{max} is not immediately apparent. This reduced variability coincides with the lower (but not significantly lower) values of COV_{IMEP} observed in Figure 3.5, and demonstrates greater control over the combustion process. As such, there were fewer slower-than-average burning cycles and fewer faster-than-average burning cycles, achieving MBT to a greater capacity from cycle to cycle. The decrease in BSFC at the optimum (minimum BSFC) 25% EGR RFCDI operating point was approximately 2.1 ± 0.7% relative to the optimum 16% baseline SI operating point, but the uncertainties preclude a definite decrease in BSFC at the lower EGR rates (16% and 20%). An examination of the pressure data (Figure 3.3) comparing the 16% EGR baseline condition to the 25% EGR corona-ignited condition reveals a slightly faster pressure rise rate during earlier crank angles, but again, the error bounds preclude any definitive conclusion regarding the total work output per cycle. While no strong conclusions can be drawn about the brake-specific fuel efficiency gains at the lower EGR rates, the emissions results were more definite. The estimated peak temperatures in the cylinder were lower for the high-EGR RFCDI operating conditions. This principally drove the observed reduction in brake-specific NO_X. At EGR rates of 16–20%, we also observed reductions in in CO and HC, which were not necessarily driven by reductions in peak temperatures, and were con-

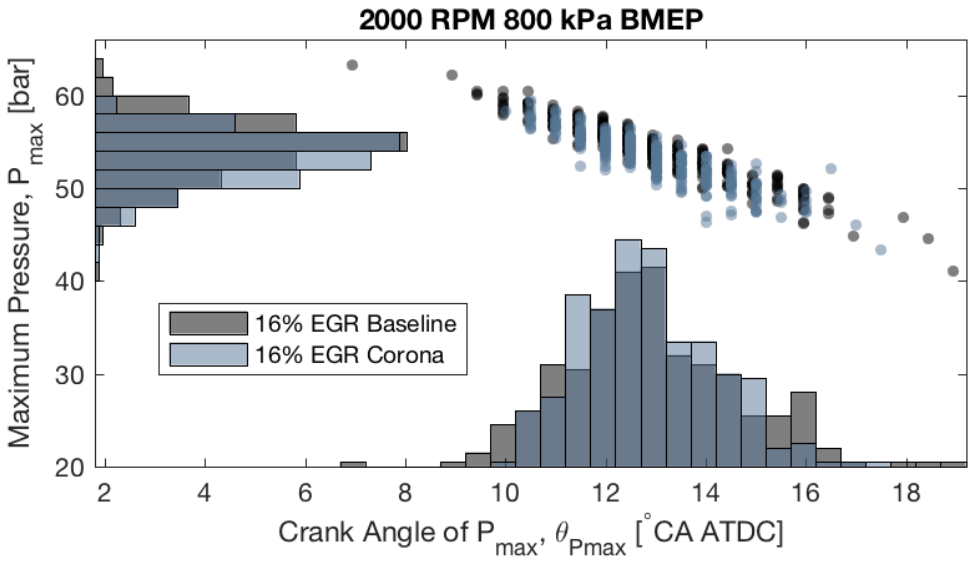

Figure 3.11: Scatterplot and histograms for selected 2000 rpm / 800 kPa BMEP tests comparing maximum pressure with maximum pressure crank angle location for baseline SI (black) and RFCDI (blue) operation, both with an EGR rate of 16%. Regions where the histograms overlap are shown in dark blue.

sistent with more complete combustion in the absence of any definite decrease in BSFC. The RFCDI consistently reduced flame development angles more than the burning angles, and this is evidence that the benefits of the RFCDI system primarily came from its ability to initiate combustion-after an initial growth period, the RF corona ignitor did not affect the flame kernel as strongly, though definite reductions in the burning angles were observed. This corroborates a reduction in burning duration angles observed by Hampe et al. (2013), Mariani and Foucher (2014), Schenk et al. (2015), and Thelen et al. (2013) using similar ignition systems in direct injection gasoline engines. The collective evidence of the lower $\mathrm{COV_{IMEP}}$ at the highest EGR rate tested (Figure 3.5), and lower flame development and burning angles (Figure 3.4), and lower variability in $\theta_{P_{max}}$ (Figure 3.11) suggest that the RF corona ignitor generated a much larger ignition volume than the traditional spark ignition system, corroborating the optical engine imaging results reported by Thelen et al. (2013). The emissions results suggest this leads to more complete combustion for EGR rates of 16%–20%, promoting greater combustion stability. Beyond EGR rates of 20%, the reduced temperature possibly resulted in reduced oxidation of both CO and HC, increasing their relative brake-specific emissions.

Moderate speeds and boosted loads

At boosted conditions, the RFCDI system did not significantly stabilize combustion in comparison to baseline SI operation, keeping $\mathrm{COV_{IMEP}}$ to acceptable values only up to 15% EGR. The greatest benefit came from the ability to advance the ignition timing (from

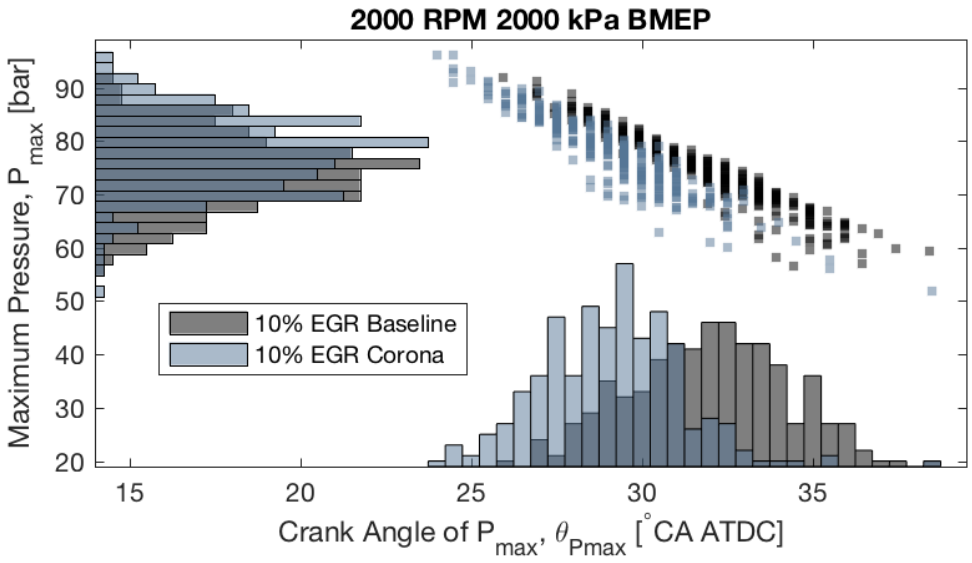

Figure 3.12: Scatterplot and histograms for selected 2000 rpm / 2000 kPa BMEP tests comparing maximum pressure with maximum pressure crank angle location for baseline SI (black) and RFCDI (blue) operation, both with an EGR rate of 10%. Regions where the histograms overlap are shown in dark blue.

2.0 ± 0.5 °CA to -3.5 ± 0.5 °CA) and hence overall combustion phasing due to an extended knock limit. This allowed the same work output for a decreased amount of both fuel and air in the charge (maintaining constant ϕ), reducing BSFC significantly. While this ability to maintain work output at lower fueling was the dominant factor in the decreased BSFC, an examination of a scatterplot comparing P_{max} and $\theta_{P_{max}}$ in Figure 3.12 reveals that there was also a slight reduction in variability of $\theta_{P_{max}}$, though there was not a reduction in the variability of P_{max}. As with the 2000 rpm / 800 kPa BMEP tests, this means that there were fewer slower-than-average burning cycles and fewer faster-than- average burning cycles, and there was some more control over the combustion process. The fact that there were fewer slower-than-average burning cycles than with baseline SI operation likely contributed to a small reduction in incomplete combustion, thereby contributing to the reduced BSFC and reduced CO emissions.

As with the 2000 rpm / 800 kPa BMEP tests, there was a decrease in the brake-specific NO_X emissions (Figure 3.10), but unlike in those tests there was no definite decrease in peak in-cylinder temperatures, to which NO_X production is extremely sensitive (Heywood, 1988). This suggests that a significant factor in the reductions in these brake-specific emissions was simply an overall increase in efficiency, evidenced by the reductions in all other brake-specific pollutant emissions and BSFC. Though using the RFCDI system achieved these reductions principally by enabling advanced combustion phasing, boosted operation inhibited its effectiveness at promoting faster burn times (Figure 3.8). The RFCDI system reduced the flame development angles less significantly than in the naturally aspirated tests, and the burning angles were unchanged or increased. Constant volume chamber experiments

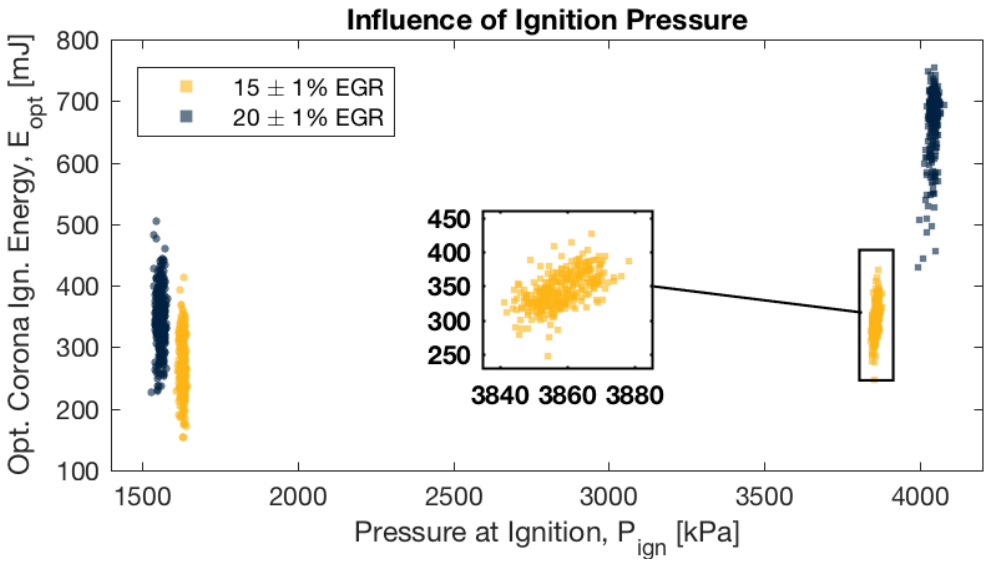

Figure 3.13: Scatterplot for 800 kPa BMEP (circles on the left) tests and 2000 kPa BMEP (squares on the right) tests comparing pressure at ignition with total measured energy input to the RF corona ignitor during operation with $15 \pm 1\%$ EGR (gold) and $20 \pm 1\%$ EGR (blue). All 300 cycles for each operating point are shown. A figure magnifying the 2000 rpm 2000 kPa BMEP operation at 15% EGR is shown in the center.

by Hampe et al. (2013) using a similar RFCDI system show that corona ignition volume decreases significantly as both temperature and pressure increase, so the increased burning angles may have been the result of a more localized radical pool (produced by the corona discharge) in the region of the RF corona ignitor, resulting in more time required to burn the rest of charge. It is important to recognize that even though the RFCDI system initiated combustion more quickly than SI, higher pressures reduced this effect for a given discharge energy, an observation that has been the case for corona discharge ignition technologies for many years (Sher et al., 1992; VanVoorhies et al., 1992).

RF corona ignition energy input

As discussed, higher pressures reduced the ability of the RFCDI system to reduce burn duration angles, in part because a greater number of collisions generally occur in non-thermal plasma in these environments, limiting the electron mobility and reducing the volume of the discharge (Fridman, 2008a). Supplying more energy to non-thermal plasmas can mitigate this reduced effectiveness, but for combustion applications the increased input energy usually results in diminishing returns with regards to ignition delay (Wolk et al., 2013; Pineda et al., 2015). Nonetheless, the energy input, E_{opt}, was optimized for these engine experiments along with the ignition timing, which typically correlates to the pressure during ignition, P_{ign}, for each operating condition. Figure 3.13 shows a series of scatterplots comparing P_{ign} with E_{opt} for four of the EGR conditions. Of all the experiments conducted in this investigation,

these four had overlapping or nearly overlapping EGR rates, the same charge stoichiometry $\phi = 1 \pm 0.05$, the same engine speed (2000 rpm), and span ignition pressures associated with both naturally aspirated loads (800 kPa BMEP, on the left with circles) and boosted loads (2000 kPa BMEP, on the right with squares). For these operating points, the average optimum ignition energy spanned from 265 mJ to 670 mJ, about an order of magnitude larger than the energy input to a traditional inductive coil fired spark plug. These values agree with a ∼1 J estimate reported by Hampe et al. (2013) and a ∼400 mJ estimate reported by Thelen et al. (2013) using similar ignition systems. In comparison, traditional ignition systems deliver about 30–50 mJ to a thermal spark (Heywood, 1988). In general, operation with higher EGR and higher loading required greater ignition energy input. As seen in the inset of Figure 3.13, a slight correlation of E_{opt} with P_{ign} is visible within the same sample of 300 cycles. As mentioned previously, the RFCDI system has circuitry that limits the current flow to prevent the discharge from transitioning to an arc, so it is not surprising that less energy would be deposited during cycles with slightly lower pressure during compression. Similar cycle-to-cycle correlations for the lower loads were not observed, likely because there was lower variability in pressure during compression during naturally aspirated operation. Regardless, for all of the operating points, the variations in measured energy were quite large.

3.5 Summary

In this chapter, the implications of using an RF corona discharge ignition system in a single cylinder direct-injection gasoline engine under both naturally aspirated and boosted loading conditions were documented, and distinct combustion improvement was found for each of the operation conditions tested: Moderate speeds with naturally aspirated loads (2000 rpm / 800 kPa BMEP) and moderate speeds with boosted loads (2000 rpm / 2000 kPa BMEP).

For loads associated with naturally aspirated operation at moderate engine speeds, the RF corona discharge ignition system subtly reduced cycle-to-cycle variability and generally decreased both the flame development angles and burning angles for a given EGR rate. This allowed for acceptable engine operation with higher EGR that drove down brake-specific NO_X emissions while maintaining brake-specific CO and HC emissions and BSFC to values similar to the optimum operation achievable with the same engine using traditional inductive spark ignition.

For loads associated with boosted (i.e. turbo- or super-charged) operation at moderate engine speeds, the RF corona discharge ignition system extended the knock limit, allowing for an overall advancement of the combustion phasing which was not practical with the inductive spark ignition system in regards to fuel consumption. This, in turn, led to a decreased amount of fuel and air required to maintain the same work output. Some decrease in cycle-to-cycle variability was observed, but to an even lesser extent than we saw with naturally aspirated loads. Flame development angles decreased for a given EGR rate, while burning angles remained unchanged or increased, demonstrating that higher pressures reduce

the benefits of the ignition system. Like Schenk et al. (2015), the EGR limit extension we obtained at boosted loads (10% to 15%) was not as significant as the extension obtained at naturally aspirated loads (16% to 25%). Nonetheless, definite decreases in BSFC and brake-specific emissions were observed.

The RF corona discharge ignition system required energy that is an order of magnitude larger than traditional inductive spark ignition (with larger energy input required for higher ignition pressure and higher EGR), and this may be a challenge for some current automotive electrical systems. However, even the largest values of energy recorded are still about three orders of magnitude less than the net heat released by the fuel. While this investigation adds to the growing body of work studying RF corona discharge ignition in boosted internal combustion engine applications, work remains to be done to establish and subsequently improve the lifetime durability of these systems before they can be incorporated in production automotive engines.

Acknowledgments

This research conducted at the Ricardo Detroit Technical Campus is the result of an industry/university collaboration supported by the NSF/DOE Partnership on Advanced Combustion Engines, Award No. CBET-1258653. I would like to acknowledge the professional and technical support of James Kezerle, Gregory Beauprez, Jeffrey Brueckheimer, Shiva Aher, Nick Fortino, and Eric Klos of Ricardo North America for the experiment coordination and test cell operation, as well as the acquisition and management of the data. The ignition system utilized in this work was graciously provided and serviced by Federal Mogul, Inc, and I would particularly like to thank Kris Mixell for the assistance. I thank Alex Jordan and Michael Neufer of the Mechanical Engineering Department Technical & Instructional Support Group staff at UC Berkeley for their helpful insight in emissions uncertainties. Considerable gratitude is owed to Benjamin Wolk for helpful and insightful comments during the preparation of the manuscript version of this chapter. Finally, I wish to thank Jordan Yvette Nerison for her helpful instruction regarding the assembly of Encapsulated PostScript files for Figures 3.3, 3.4, 3.6, 3.7, 3.8, and 3.10 and for illustrating the piston-cylinder assembly and corona ignitor in Figures 3.1 and 3.2.

Chapter 4

Pulsed nanosecond discharge ignition

This chapter is based on research completed for a manuscript currently under revision for *Combustion Science and Technology* (Pineda, Wolk, Sennott, Chen, Dibble and Singleton, 2017) and presented at the *3rd Laser Ignition Conference* at Argonne National Laboratory in Lemont, IL (Pineda et al., 2015).

4.1 Introduction

In this chapter, the topic of exploration is cathode-directed pulsed nanosecond discharge (PND) ignition, in which a pair of electrodes in a combustion chamber receive a series of large and fast voltage pulses. As mentioned in Chapter 2, this increases the reduced electric field E/n between the electrodes, pushing electrons from the anode to the ground cathode through narrow ($\sim$100 μm) channels henceforth referred to as *streamers* (Ono and Oda, 2003). These electrons are at much higher temperatures than the neutral molecules and ions, forming a non-thermal plasma (Fridman, 2008c) and activating alternative kinetic pathways to facilitate the ignition of dilute fuel-air mixtures (Starikovskaia, 2006; Starikovskiy and Aleksandrov, 2013; Ju and Sun, 2015; Aleksandrov et al., 2009). As discussed in Chapter 2, the chemical kinetics of these alternative ignition pathways are a topic of active research and many mechanisms have been proposed for a variety of reduced electric field regimes (Aleksandrov et al., 2009; Kosarev et al., 2008; Uddi et al., 2009; Bisetti and El Morsli, 2012; Adamovich et al., 2015; DeFilippo and Chen, 2016). However, compounding hydrodynamic effects from a pulsed discharge in breakdown regimes poses issues for practical ignition in automotive engines, which must operate at a variety of dilution, speeds, and loads, corresponding to a large range of mixtures, residence times, and ignition pressures, respectively.

As mentioned in Chapter 2, various PND systems have been observed to improve the performance and extend the dilute operating limits of internal combustion engines (Cathey et al., 2007; Shiraishi et al., 2009; Pancheshnyi et al., 2014; Tropina et al., 2016). Recently, some of these systems—in conjunction with novel electrode geometries—have also been shown to reduce flame development times in engines using both E85 (Sjöberg et al.,

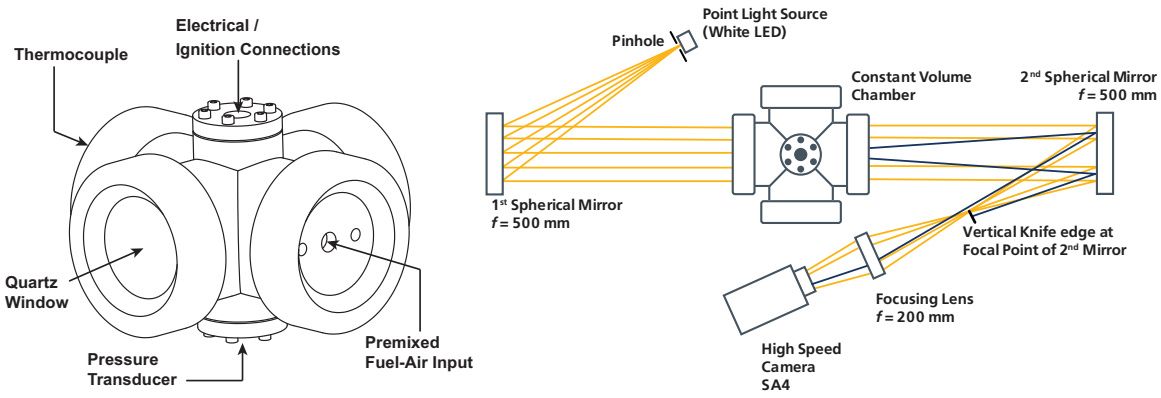

Figure 4.1: Diagram of the constant volume chamber used in this investigation (left) and a top view of its placement in the laboratory optical schlieren setup (right). The focal length of each spherical mirror is 500 mm and the focal length of the focusing lens is 200 mm.

2014) and gasoline (Sevik et al., 2016), leading to improved dilute operation performance. In the E85 investigation, high-speed (20 kHz) imaging inside of the cylinder suggests that the developing flame kernel is jettisoned into the combustion chamber. The turbulent flow field inside of the engine precludes a definite conclusion as to why this jettison effect occurs, and so more fundamental experiments are needed to explain the combustion enhancement. Though there have been many experimental investigations of PND ignition in constant volume chambers, most utilize relatively simple electrode geometries such as plate electrodes (Aleksandrov et al., 2009; Kosarev et al., 2008; Uddi et al., 2009; Kosarev et al., 2016; Nagaraja et al., 2013), concentric electrodes (Singleton et al., 2011), or pin-to-pin electrodes (Lovascio et al., 2017) with which convenient numerical model comparisons can be made (Takana et al., 2014; Castela et al., 2016). Few experiments have been carried out to characterize the physics of combustion enhancement observed in the types of electrodes expected to be used in automotive engines, for which modeling investigations are hindered by the large separation between non-thermal plasma and hydrodynamic timescales. This short study documents hydrodynamic aspects of PND ignition in lean premixed methane-air mixtures and provides an explanation for the enhancements seen in the aforementioned engine experiments.

4.2 Description of experiment

Experimental setup

To analyze the flame development associated with PND ignition, a 1.45 L stainless steel constant volume combustion chamber with optical window access for high-speed schlieren imaging was used. Diagrams of the chamber and the schlieren optical setup are shown in Figure 4.1. In this work, ignition was provided by both a traditional inductive spark (SI) and a nanosecond pulse generator (Transient Plasma Systems, Inc.) that uses a rapid

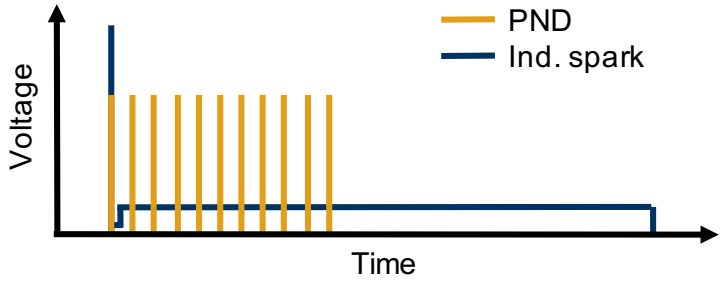

Figure 4.2: Conceptual diagram of voltage from inductive spark ignition system over 2.5 ms (adapted from Heywood (1988)) and the PND system using 10 pulses as a function of time.

Figure 4.3: Diagrams of spark plugs used in this investigation. The geometry on the left is the same as that used by Sjöberg et al. (2014) and Sevik et al. (2016) in internal combustion engine experiments, while the geometry on the right represents an attempt to achieve multi-point ignition.

voltage rise (∼10 kV) and short voltage pulse (12 ns) to induce streamer discharges at 10 kHz between the non-resistive electrodes in the chamber. A conceptual diagram comparing the voltage of a conventional inductive spark system and that of 10 pulses from the PND ignition system is shown in Figure 4.2. The electrodes used were of custom experimental geometry, shown in Figure 4.3. The geometry of the electrode in the left of Figure 4.3 with a 2.5 mm electrode gap was chosen for our tests because it is the same geometry used in the aforementioned E85 (Sjöberg et al., 2014) and gasoline (Sevik et al., 2016) internal combustion engine experiments. The effect of number of pulses n_p was investigated, varying from 2, 5, 10, to 20 pulses. Separate tests were conducted with the geometry shown in the right of Figure 4.3 with a 3.25 mm gap to qualitatively examine attempts at multi-point ignition.

For each experiment, the chamber was evacuated and then filled with methane and air mixed at an equivalence ratio (ϕ) of 0.7 ± 0.03 to an initial pressure P_{init} of 200 ± 0.5 kPa. ϕ was measured using species partial pressures in a separate premixed tank to ensure consistent fuel concentration and mixing. This value of ϕ was chosen because reliable ignition

could be obtained using both ignition techniques in this fuel-air mixture, facilitating their comparison. The initial temperature in the chamber was measured as 300 ± 5 K with a K-type thermocouple. This corresponds to a number density of approximately $n = 80$ mol/m^3, which falls just inside the range of number densities in some of the preheated E85 engine experiments by Sjöberg et al. (2014). Non-thermal plasma chemistry is a strong function of the reduced electric field, E/n (Fridman, 2008a), and so the behavior of the discharge at engine-relevant densities is expected to be similar to the behavior during engine operation, even though the subsequent flame kernel development will be different. The pressure inside the chamber during ignition and flame development was measured at 100 kHz using a piezoelectric pressure transducer (6052B Kistler) and the signals were amplified using a dual-mode charge amplifier (5010B Kistler). Schlieren imaging was performed at 50 kHz using high-speed camera (Photron FASTCAM SA4), recording the development of the flame kernel during the first few milliseconds after ignition through the quartz windows. The size of the premixed tank restricted the total number of experiments; at least nine runs per condition were possible.

For the PND experiments, the voltage and current across the electrodes during the first pulse were measured with an inline high-voltage attenuator and current probe (Transient Plasma Systems, Inc.) and recorded with a digital oscilloscope at 2.5 GHz (Tektronix TDS 3024B). The first pulse in every experiment was highly consistent, though recent pressure-rise calorimetry work by Wolk and Ekoto (2017) has shown that subsequent pulses are not necessarily the same as the first, which will be discussed later.

Experimental data analysis

The net heat release rates (HRR) of the ignition experiments are calculated based on the in-chamber pressure history using Equation 4.1, where V is the chamber volume and γ is the ratio of specific heats (Heywood, 1988). This is the same as Equation 3.1 in Chapter 3, except V is constant, and so all dV terms are zero. Heat losses through the chamber walls are not considered and so these calculations are for comparison only. γ is determined by weighting the average of the specific heats in the burned (γ_b) and unburned (γ_u) states according to Equation 4.2, in which β is a progress variable defined by Equation 4.3. γ_b and γ_u are calculated from 1-D adiabatic free flame simulations in Cantera (Goodwin et al., 2014) using mixture-averaged transport properties and the GRI-MECH 3.0 mechanism (Smith et al., 1999).

$$\frac{dQ}{dt} = \frac{V}{\gamma - 1}\frac{dP}{dt} \tag{4.1}$$

$$\gamma = (1 - \beta)\gamma_u + \beta\gamma_b \tag{4.2}$$

$$\beta(t) = \frac{P(t) - P_{init}}{P_{max} - P_{init}} \tag{4.3}$$

$$Q_{net}(t) = \int_0^t \frac{dQ}{dt} dt \tag{4.4}$$

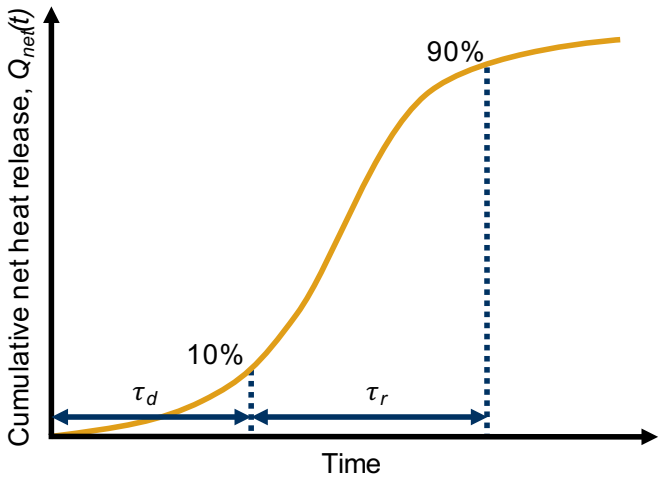

Figure 4.4: Conceptual diagram of $Q_{net}(t)$ (adapted from Wolk et al. (2013)) describing the definitions of τ_d and τ_r.

Equation 4.1 is integrated over time in Equation 4.4 to obtain the cumulative net heat release as a function of time, $Q_{net}(t)$, as well as the total net heat released, $Q_{net,tot}$. $Q_{net,tot}$ is used to calculate the *flame development time*, τ_d, and *flame rise time*, τ_r. In this study, τ_d is defined as the time between ignition and when the first 10% of $Q_{net,tot}$ has been achieved. Similarly, τ_r is defined as the time between when the first 10% and the first 90% of $Q_{net,tot}$ has been achieved. These measurements are conceptually similar to those of CA10 and CA90 in Chapter 3, and a conceptual diagram of these timescales with respect to $Q_{net}(t)$ is shown in Figure 4.4. They are typically comparable with one another (Heywood, 1988) and allow us to compare the influence of the PND system at both early and late stages of the combustion process. The sum of τ_d and τ_r is referred to as the *overall burning time*, τ_o, and this is used to compare overall combustion time.

For each experiment, the flame size L_f is calculated based on the high-speed imaging data using an edge-detection algorithm in MATLAB to track the greatest extent of the flame kernel after subtracting the first frame from every frame of the footage. This measurement is then numerically differentiated with respect to time to calculate burned flame speed s_b. Unburned flame speed s_u is calculated by multiplying s_b by the adiabatic density ratio of the burned and unburned mixture, ρ_b/ρ_u, as in Equation 4.5:

$$s_u = s_b \frac{\rho_b}{\rho_u} \tag{4.5}$$

Like the values of γ_b and γ_u, ρ_b/ρ_u is obtained from the aforementioned CANTERA (Goodwin et al., 2014) simulations. The simulation is also used to calculate a reference unburned flame speed, $s_{u,ref}$, with which to compare the experimental unburned flame speeds obtained from Equation 4.5. This method of calculating s_u is acceptable because the thermal and mass diffusivities of methane/air flames are approximately equal, and so flame stretch effects

are negligible for most of the flame kernel evolution (Law, 2006). This calculation is used primarily as a method of comparison among the different ignition conditions, and secondarily to confirm that the measured ϕ, P_{init}, and T_u are reasonably accurate. If they are accurate, then the calculated s_u of the flames will approach $s_{u,ref}$ as the flame leaves the region of the electrodes. The experimental uncertainties $\Delta\phi = 0.03$, $\Delta P_{init} = 0.5$ kPa, and $\Delta T_u = 5$ K are propagated to calculate deviations in $s_{u,ref}$, and these uncertainties are added in quadrature (Coleman and Steele, 2009) as in Equation 4.6.

$$\Delta s_u = \sqrt{\left(\frac{\partial s_u}{\partial \phi}\Delta\phi\right)^2 + \left(\frac{\partial s_u}{\partial P_i}\Delta P_i\right)^2 + \left(\frac{\partial s_u}{\partial T_u}\Delta T_u\right)^2} \tag{4.6}$$

The reference unburned flame speed is calculated as $s_{u,ref} = 13.9 \pm 2.0$ cm/s.

For tests with the disk electrode, the total schlieren image intensity is calculated as a function of time. The first frame is subtracted from every frame of footage, and so only the total intensity of the resulting differences is calculated. The intensity serves as a measure of "schlieren activity," indicating thermal events associated with the pulsed discharges, and is particularly useful for detecting events otherwise unobservable to the human eye.

4.3 Results

The ensemble-averaged peak pressure P_{peak}, calculated total cumulative net heat release $Q_{net,tot}$, flame development time τ_d, flame rise time τ_r, overall combustion time τ_o, as well as flame size L_f and unburned flame speed s_u at 3 ms after ignition are shown in Table 4.1. Each

Table 4.1: Summary of results. For P_{peak} and $Q_{net,tot}$, the uncertainty shown consists of 95% confidence intervals added in quadrature with the systematic measurement uncertainty (Coleman and Steele, 2009). For τ_d, τ_r, and τ_o, the uncertainty shown is based on 95% confidence intervals alone, and for the high-speed imaging data, the uncertainty shown is based on 90% confidence intervals alone.

n_p	P_{peak} [kPa]	$Q_{net,tot}$ [J]	τ_d [ms]	τ_r [ms]	τ_o [ms]	L_f at 3 ms [mm]	s_u at 3 ms [cm/s]
SI	935 ± 4	3252 ± 165	57.0 ± 1.0	70.3 ± 1.2	127.3 ± 1.4	12.7 ± 1.0	16.7 ± 1.0
2	932 ± 3	3260 ± 181	52.9 ± 1.6	71.1 ± 1.1	124.0 ± 1.5	10.4 ± 1.0	16.2 ± 1.0
5	934 ± 3	3274 ± 94	50.7 ± 0.6	70.1 ± 0.8	120.8 ± 1.2	11.5 ± 0.3	17.3 ± 2.1
10	947 ± 5	3332 ± 167	49.2 ± 0.7	68.8 ± 1.3	118.0 ± 1.7	14.0 ± 1.3	19.0 ± 1.7
20	948 ± 7	3344 ± 154	46.4 ± 0.8	67.9 ± 1.0	114.3 ± 0.9	18.0 ± 2.1	23.6 ± 3.2

of these results is discussed in more detail in the sections that follow. For the results in this paper, ignition was not obtained using a single pulse ($n_p = 1$), and ignition was not observed unless transient arc breakdown occurred (as opposed to ignition by streamer discharge alone, which has been shown to occur with the same pulsed system (Singleton et al., 2011)). The likelihood of arcing has been shown to increase as the number of pulses increase (Wolk and Ekoto, 2017), and its occurrence during these PND ignition experiments likely explains

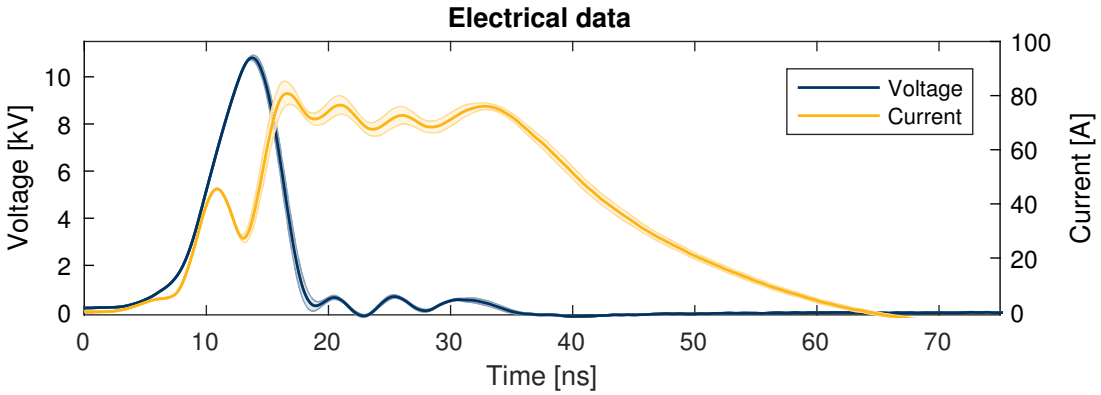

Figure 4.5: Ensemble average of all voltage and current measurements of first pulses in this experimental investigation. Shaded regions indicate 95% confidence intervals.

the beneficial hydrodynamic effects discussed throughout the rest of this paper. Strong visible light emission in the aforementioned E85-fueled engine experiments (Sjöberg et al., 2014) indicates that this phenomenon may also be occurring during PND ignition in internal combustion engine operation (Singleton et al., 2017). Thus, despite not achieving steamer-only ignition in our experiments, it is important to nonetheless quantify and characterize the effects of multiple pulses and clarify the results of the engine experiments using the same PND ignition system and electrodes (Sjöberg et al., 2014; Sevik et al., 2016).

Electrical measurements

Ensemble averages of the recorded voltage and current of the first pulses for all experiments with the castle-type electrode are shown in Figure 4.5. From these data, the peak voltage was calculated to be 10.8 ± 0.1 kV and the peak current to be 80 ± 4 A. As seen in Figure 4.5, these peaks do not occur at the same time, and the resulting average peak power is calculated to be 590 ± 60 kW with an energy deposit of 3.5 ± 0.4 mJ per pulse. This is the same order of magnitude as the pulse energies reported by others (Pendleton et al., 2013; Lefkowitz and Ombrello, 2017a) using similar PND ignition systems, and is about an order of magnitude lower than a typical inductive spark energy of ∼30–50 mJ (Heywood, 1988). The simultaneous occurrence of low voltage and high current after the 20 ns mark is indicative of a likely transition to arc.

Pressure measurements

Ensemble-averaged pressure traces and heat release rates for the inductive SI case and the PND ignition cases are presented in Figure 4.6. PND ignition resulted in slightly earlier pressure rise than inductive spark ignition. Increasing the number of pulses resulted in still faster pressure rises, with higher peak pressures. Heat release rates calculated from the in-chamber pressure history of PND ignition experiments generally peak earlier than those of

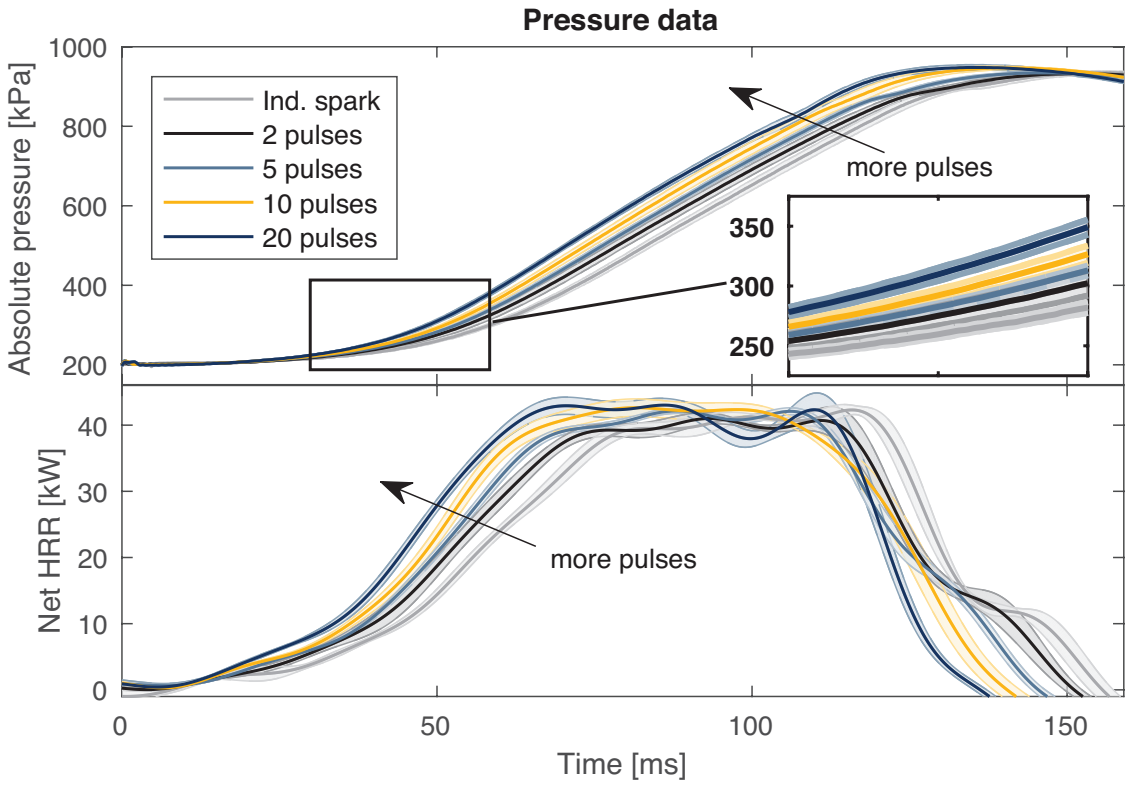

Figure 4.6: Ensemble-averaged pressure traces (top) and net heat release rate (bottom). $\phi = 0.7 \pm 0.03$ and $P_{init} = 200 \pm 0.5$ kPa for all runs. Shaded regions indicate calculated uncertainty based on both 95% confidence intervals and systematic measurement uncertainty.

traditional inductive SI experiments. The heat release curves in Figure 4.6 show several local maxima instead of just one because the walls of the constant volume chamber are impacted by the flame front at different times. This effect becomes more pronounced as the number of pulses increases in the PND cases. As combustion ends, the HRR rapidly decreases and becomes negative due to heat losses through the walls and reduction of number of moles in the gas phase caused by condensation of H_2O. As indicated in Table 4.1, the 2-pulse and 5-pulse cases yielded similar peak pressures, P_{peak}, to the inductive spark case, while the 10-pulse and 20-pulse cases yielded somewhat larger P_{peak} values. The total cumulative net heat release, $Q_{net,tot}$, of the PND experiments is greater than that of the traditional inductive SI experiments, though uncertainties preclude a definite conclusion. In all of the PND cases, τ_d is, on average, smaller than that of the inductive SI case. Increasing n_p further reduces τ_d, culminating in a total decrease of 10.6 ± 1.8 ms relative to the inductive SI case for $n_p = 20$. τ_r was also reduced, although to a lesser extent and less definitely than τ_d, culminating in a decrease of only 2.4 ± 2.2 ms relative to the inductive SI case. Consequently, overall combustion time τ_o is also reduced in the PND cases relative to the inductive SI case.

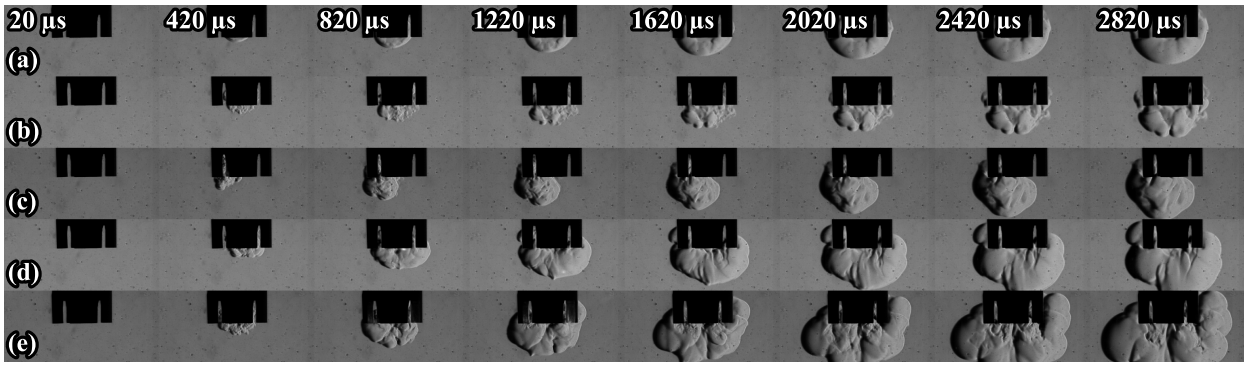

Figure 4.7: Representative schlieren images taken at 50,000 fps for (a) spark-ignited and nanosecond pulsed discharge ignition modes using (b) 2 pulses, (c) 5 pulses, (d) 10 pulses, and (e) 20 pulses.

High speed video measurements

Qualitative analysis of the videos reveals that in the PND cases, the flame kernel was often jettisoned away from the electrodes after the first couple of discharges, confirming the phenomenon observed by Sjöberg et al. (2014). Additional discharges further push the kernel away, as seen in Figure 4.7. A closer analysis of the imaging indicates that transition to arc occurred after a few pulses, suggesting that ignition by streamers alone was not possible for this particular electrode geometry at these number densities. This means that for those pulses, brief but substantial temperature rises occur in the electrode gap, rapidly reducing the density and jettisoning hot gases out of the electrode gap. Image analysis confirmed these qualitative results—for the pulsed discharge experiments, an increasing number of pulses generally resulted in faster flame kernel growth and higher initial flame speeds, shown in Figure 4.8.

For the quantitative analysis presented in Figure 4.8, the first 13 frames of every video have been omitted due to visual interference from the electrodes in the earliest moments of ignition. This corresponds to 260 μs; and for these experiments, this means that flame kernel sizes smaller than $\sim$5 mm and those between the electrode gaps are not tracked. Likewise, in some cases, flames that developed more quickly moved out of the view of the camera much earlier than other flames, making only the first few milliseconds ($\sim$4.5 ms) of footage useful for comparison. Additionally, the original definition of L_f poses complications with a wrinkled flame surface, since the "greatest extent" of the flame kernel can overpredict the flame's true location; however, analysis of the images reveals that the wrinkling adds only approximately 1 mm to the uncertainty of L_f, and this uncertainty is included in the plot in Figure 4.8. The 0.260–4.50 ms window of comparison shown in Figure 4.8 reveals some contrasts with the pressure results; high-speed imaging measurements listed in Table 4.1 show that the traditional inductive spark ignition cases demonstrate faster initial flame growth than the 2-pulse discharge cases and similar initial flame growth to the 5-pulse discharge cases 3 ms after the start of ignition. In all cases, after the discharge ceased, the flame speed for each condition was similar and the calculated unburned speeds approached

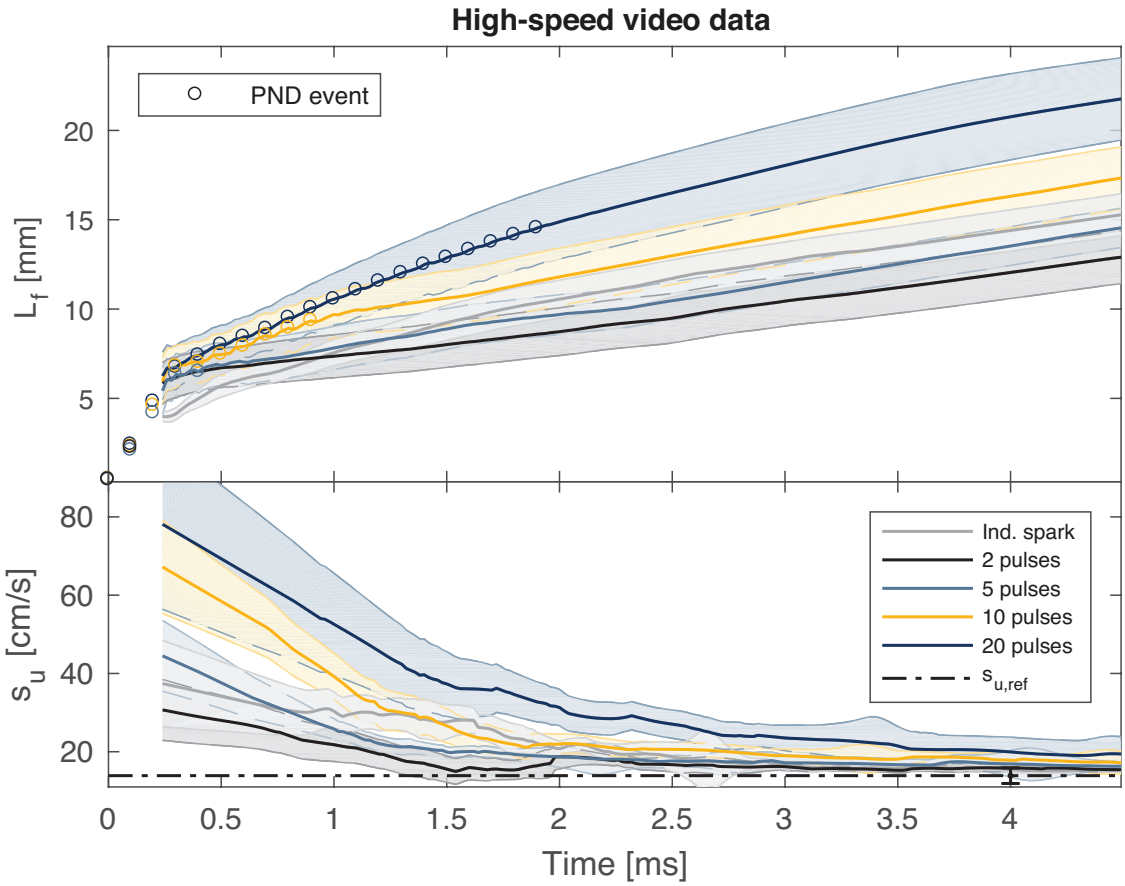

Figure 4.8: Size, L_f (top), and unburned flame speed, s_u (bottom), of flame kernels calculated from high speed schlieren imaging. The first few frames are omitted due to visual interference with the electrodes. Overlaid markers on L_f indicate the time of a PND event and have been linearly interpolated from a flame size of 0 mm at 0 ms in the omitted regions. The shaded regions indicate 90% confidence intervals.

the value reported by the 1-D simulation. Uncertainty in flame speed also decreased as the flame kernel developed after the end of discharge.

To test the feasibility of multi-point ignition, ignition with the disk electrode geometry shown in Figure 4.3 was evaluated with the same pulse generator. As with the first electrode, we found that multi-point streamer ignition was not possible without ultimately transitioning to arc. However, arcing did not occur until a number of pulses had been driven, and, in several repeated cases, evidence of the streamers was visible in the schlieren images. A representative example of this phenomenon is shown in Figure 4.9.

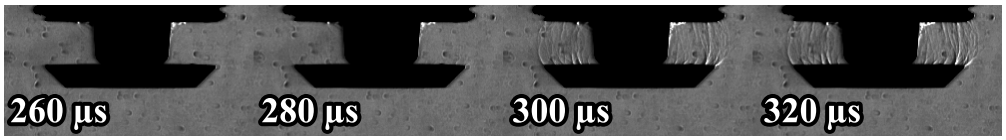

Figure 4.9: Schlieren images of local density reduction in the shapes of streamers. Images have been enhanced for clarity.

4.4 Discussion

While increasing the number of pulses generally reduces flame development time, the reduction-per-pulse relative to SI ignition reduces with each additional pulse, indicating that the benefits associated with additional pulses decreases as the flame kernel develops. As the number of pulses increases, the peak pressure increases and the peak pressure occurs earlier. This helps explains some of the efficiency gains observed in previous engine experiments (Sjöberg et al., 2014; Sevik et al., 2016).

Hydrodynamic effects

The high-speed images in Figure 4.7 show that there is a significant non-chemical component to the combustion enhancement. The flame kernel is driven away from the electrodes, reducing heat losses to the electrodes from the developing flame. While this helps explain the reduced τ_d in the pulsed cases, increased flame kernel expulsion alone does not completely explain the decreases in τ_d between the inductive spark cases and the pulsed discharge cases (a decrease of 10 ± 1.8 ms), since the flame kernel from the inductive spark discharge is initially the same size or larger than the flame kernels from the 2-pulse and 5-pulse discharges, as shown in Figure 4.8. The high-speed images in Figure 4.7 show increased flame wrinkling, a phenomenon which increases the surface area of the flame in contact with the unburned mixture and enhances the overall burning rate. This enhancement effect persists beyond the initial flame development, which is why τ_r also slightly decreases in the pulsed discharge cases.

The causes for the instabilities which increase flame wrinkling are likely rooted in local pressure changes caused by the repetitive discharges. The L_f data in the inset of Figure 4.8 show that the continued discharges are the primary factor in the divergence of the different PND ignition modes—for the first 10 pulses of the 20-pulse case, the average L_f is similar to that of the 10-pulse case, and so on. Reactive flow experiments by Lefkowitz and Ombrello (2017b) have shown evidence of pulse-to-pulse coupling, in which a moving flame kernel ignited by a nanosecond pulsed discharge is influenced by subsequent pulses. Although the gases in this experiment are initially quiescent, the pulses could induce some bulk fluid motion. 3-D Direct Numerical Simulation modeling by Castela et al. (2016) and associated experimental work by Lovascio et al. (2017) with pin-to-pin electrode geometries have shown as such. The aforementioned pressure-rise calorimetry experiments by Wolk and Ekoto

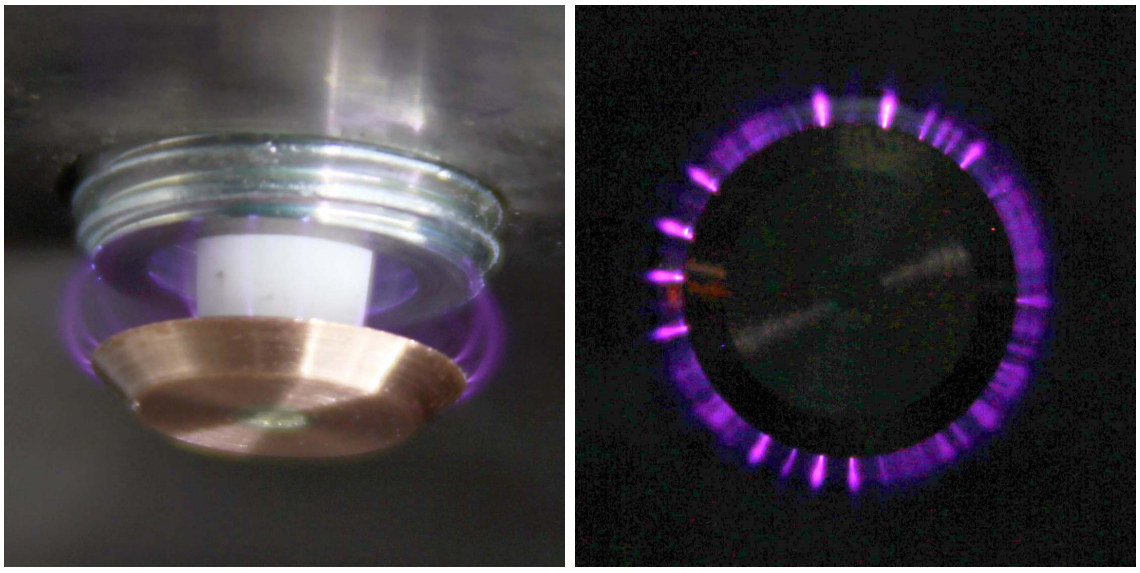

Figure 4.10: Color digital photographs of disk electrode generating distributed streamers in side view (left) and bottom view (right). Images courtesy Transient Plasma Systems, Inc.

(2017) indicate that transient arc breakdown is more likely as the number of pulses increase, and that these discharges cause more rapid local gas heating than low temperature plasma (LTP) discharges. As additional pulses are driven between the electrodes, the lower number density increases the local reduced electric field, so that the successive pulses are "thermally preconditioned" into transitioning to arc. In our study, the pressure gradients associated with this phenomenon interact with the electrode shape to drive the hot gases away from the cold metal surfaces, simultaneously reducing heat losses and increasing wrinkling of the flame kernel surface.

Chemical effects

The effect of chemistry on combustion enhancement is more difficult to discern from the presented measurements, and thus only limited conclusions can be drawn from the results. The high-speed schlieren images of the disk electrode in Figure 4.9 definitely show a decrease in local fluid density—indicating a rise in local fluid temperature, a reduction in number of molecules, or both. Visible-light photographs of the streamers for this electrode are shown in Figure 4.10. A comparison between Figure 4.9 and Figure 4.10 is highly suggestive of a link between the observed density gradients and the streamers. A plot of the schlieren activity for the experiment shown in Figure 4.9 is shown in Figure 4.11. It can be seen that each PND event is associated with a rise in schlieren activity, indicating changes in local density gradients in the image. Though the reasons for this cannot be confirmed without high-resolution species measurements in time, a survey of the plasma literature suggests that the likely culprit for these gradients is an increase in the local gas temperature caused by fast

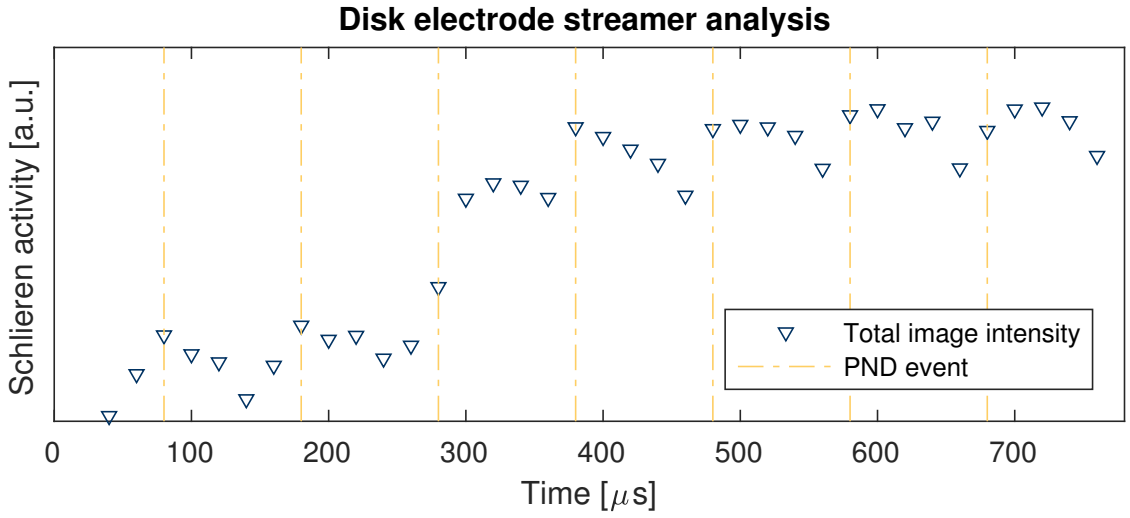

Figure 4.11: Plot of total image intensity for one of the disk electrode experiments. The sudden change in image intensity near 280–320 μs corresponds to the event shown in Figure 4.9.

gas heating processes associated with LTP discharges. These processes include electron-ion recombination, quenching of electronically-excited N_2 and O (Stancu et al., 2010; Bak et al., 2011; Lo et al., 2014a), radical recombination (Pendleton et al., 2013), and relaxation of vibrationally excited O_2 and N_2 (Ono et al., 2010; Lo et al., 2014b). In air at atmospheric pressure, these processes occur on timescales spanning ∼10 ns to ∼100 μs, and so different processes may influence the results seen in Figure 4.11 at different times.

More conclusively, the fact that ignition was not possible using a single pulsed discharge in any of the experiments suggests that although reactive species are generated, not enough are produced, and/or the local gas temperature is not high enough (>∼700 K) to sustain chain-branching reactions (Law, 2006). The decrease in schlieren activity following each pulse in Figure 4.11 is likely due to the diffusion of the density gradient into the surrounding mixture, but subsequent pulses drive the temperature and/or radical increases required for successful ignition. The gas is 'primed' for the next pulse: since the number density is lower, the reduced electric field of the next pulse is higher, approaching the threshold to arc transition, as was observed in the engine experiments using the same electrode geometry (Sjöberg et al., 2014).

4.5 Summary

In comparison with the traditional inductive spark ignition, the pulsed nanosecond discharge ignition modes were found to produce higher initial pressure rise rates and likewise higher initial net heat release rates as inferred from pressure measurements. A significant hydrodynamic contribution to the combustion enhancement was observed: High-speed schlieren imaging revealed that increased expulsion of the flame kernel away from the electrodes was

primarily responsible for the reduced flame development times. In these experiments, a small reduction in flame rise time was also observed. The ignition event was aided most significantly in the early development of the flame kernel, after which induced wrinkling continued to enhance the burning rates. Evidence of chemical contributions to the combustion enhancement is observed and discussed, but our limited measurements preclude quantitative assessments of these contributions relative to the hydrodynamic contribution. Most importantly, these data help explain the combustion enhancement observed using a similar pulsed nanosecond discharge system and electrode geometry in internal combustion engine experiments (Sjöberg et al., 2014; Sevik et al., 2016). However, the initial pressures in this study were limited to 200 kPa, far less than in engine conditions; therefore, strong conclusions cannot be drawn about the relevance of the observed ignition behavior in an absolute sense. Rather, the trends observed in these experiments are consistent with those in the engine experiments (Sevik et al., 2016). Finally, these results highlight the influence of electrode geometry and pulse behavior in practical PND ignition systems, especially in near-breakdown regimes where fast gas heating is expected.

Acknowledgments

This research at University of California, Berkeley was partially supported by the National Science Foundation, Grant No. DGE 1106400 and by NSF/DOE Award No. CBET-1258653. Gratitude is owed to Tim Sennott for arranging the collaboration with Transient Plasma Systems and to Benjamin Wolk for much of the initial experimental setup. Thanks are owed to Dan Singleton and Mark Thomas of Transient Plasma Systems for the experimental assistance, as well as Damien Eymeric for the LabVIEW and image processing assistance. I wish to thank Dr. Colin H. Smith for insightful comments during manuscript preparation and Jordan Yvette Nerison for her helpful instruction regarding the assembly of Encapsulated PostScript files in Figure 4.6 and Figure 4.8 and for the final illustration of Figure 4.1.

Chapter 5

Conclusions and the path forward

In this dissertation, advanced ignition techniques for internal combustion engines are analyzed with the aim of near-term implementation in automotive engines. This chapter discusses the accomplishments and relevance of this work, and it provides suggestions for future research directions in the field of plasma-assisted ignition.

5.1 Accomplishments

In this dissertation, historical, social, and technical contexts of automotive engines and the automotive industry are provided to best understand where advanced ignition methods can have a most significant impact. Additionally, a combustion-specific context is provided, demonstrating how non-thermal plasma can enhance combustion through chemical means to extend the lean and exhaust gas dilution operation limits of internal combustion engines. Experimental results of testing a corona discharge ignition system in a boosted gasoline research engine are presented. In these experiments, it was observed that using a corona discharge ignition system enabled extensions of the practical exhaust gas recirculation limits of stable operation, resulting in up to a $\sim$4% reduction in fuel consumption and up to a $\sim$70% reduction in harmful nitrogen oxide emissions. Alongside the engine experiments, the results of a more fundamental constant volume chamber study are presented, in which a pulsed nanosecond discharge ignition system was tested in lean methane-air mixtures. The constant volume chamber results demonstrate a reduction of up to $\sim$10% in overall combustion duration relative to traditional inductive spark ignition methods. Most importantly, it was discovered that a substantial portion of the combustion enhancement is due to hydrodynamic effects, rather than solely chemical kinetic effects. The role that this work will take in a broader research context is discussed in Sections 5.3 and 5.4. First, some more detailed analysis of the results is provided in Section 5.2.

5.2 Analysis

Although the research presented in this dissertation is of an applied nature, there are some fundamental lenses through which the results can be analyzed. This section presents some thermodynamic and combustion analyses of the dissertation results.

Thermodynamic considerations

The engine experiments in Chapter 3 demonstrate significant improvement in both brake-specific fuel consumption and brake-specific emissions, and a thermodynamic analysis related to the original Otto and Carnot cycles discussed in Section 1.1 is presented here to explain the improvement. As originally stated in Equation 1.4 and reproduced here in Equation 5.1, the efficiency of a Carnot heat engine increases as the average temperature of the high-temperature reservoir, T_H increases:

$$\eta_{\text{Carnot}} = 1 - \frac{T_C}{T_H} \tag{5.1}$$

For an Otto-like cycle, this corresponds to a higher average temperature before the expansion stroke, since this will lead to more heat-to-work conversion in a given cycle. P-V diagrams of the engine experiments are presented in Figures 5.1 and 5.2. The naturally-aspirated operation results are shown in Figure 5.1 and the boosted operation results are shown in Figure 5.2. Figures 5.1 and 5.2 bear a resemblance to the ideal Otto cycle P-V curves depicted in Figure 1.2 in Chapter 1, though with clear differences resulting from the presence of the intake and exhaust strokes not depicted in Figure 1.2. Additionally, the presence of frictional effects and non-ideal combustion phasing—particularly in Figure 5.2—provides a contrast to the ideal cycle.

An analysis of Figure 5.1 reveals no obvious thermodynamic reason for the observed fuel consumption reductions mentioned in Chapter 3 since the P-V curves are quite similar to one another, but the concept of maximum brake torque (Heywood, 1988) as related to Equation 5.1 provides some illumination. Maximum brake torque for a given fuel energy input occurs when this heat is released at a point in the cycle where there is maximum heat-to-work conversion—that is, a combustion event that occurs such as to maximize T_H in Equation 5.1. As was discussed in Section 3.4, the naturally-aspirated loading operation results with the corona discharge ignition system showed greater control over the combustion process—that is, there were fewer slower-than-average combustion events and fewer faster-than-average combustion events, which allowed the maximum brake torque to be achieved to a greater extent in each cycle.

For the boosted operation in Figure 5.2, however, the differences in the P-V curves are more obvious. Through both the corona discharge ignition system and the subsequent exhaust gas recirculation limit extension, the knock limit was extended, allowing for earlier ignition timing to produce a cycle closer to maximum brake torque and a P-V curve that more closely resembles the ideal P-V curves depicted in Figure 1.2. Peak pressures are higher

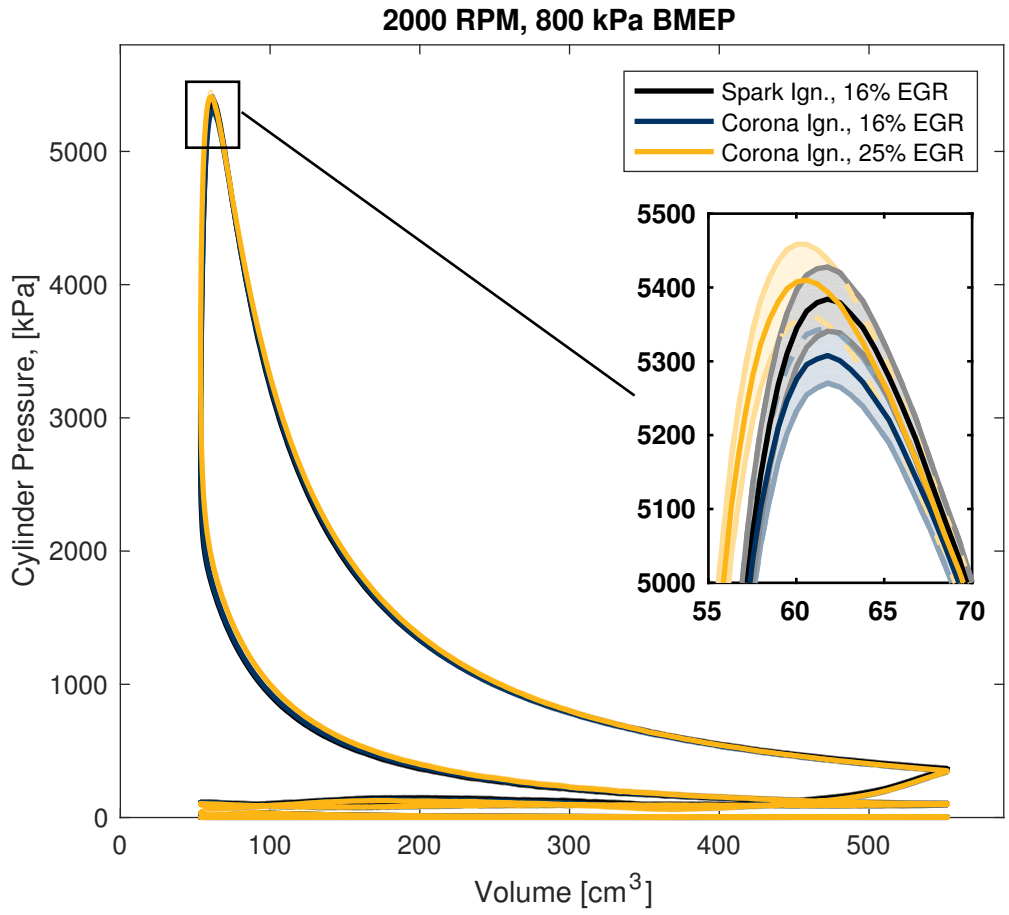

Figure 5.1: Pressure-volume diagram for the naturally-aspirated loading operation engine experiments discussed in Chapter 3. Black curves are for spark-ignition operation with an EGR rate of 16%, blue curves are for corona discharge ignition operation with an EGR rate of 16%, and gold curves are for corona discharge ignition operation with an EGR rate of 25%.

for the corona discharge ignition cases, though changing fuel-air-exhaust gas composition precludes a translation to higher T_H. In general, combustion happened more quickly with the corona discharge ignition system, and this enabled the use of less fuel for the same amount of work output.

Reduced combustion duration is also the theme for the constant volume chamber experiments presented in Chapter 4. In that case, the volume was constant and so no work was done, but reduced combustion duration generally translates to less time for heat loss to the walls of the combustion chamber, and in an engine, this also translates to less time for engine knock to occur. This was also observed in the engine experiments discussed in Chapter 3, and this concept has important implications for automotive engines, as outlined in Section 5.3.

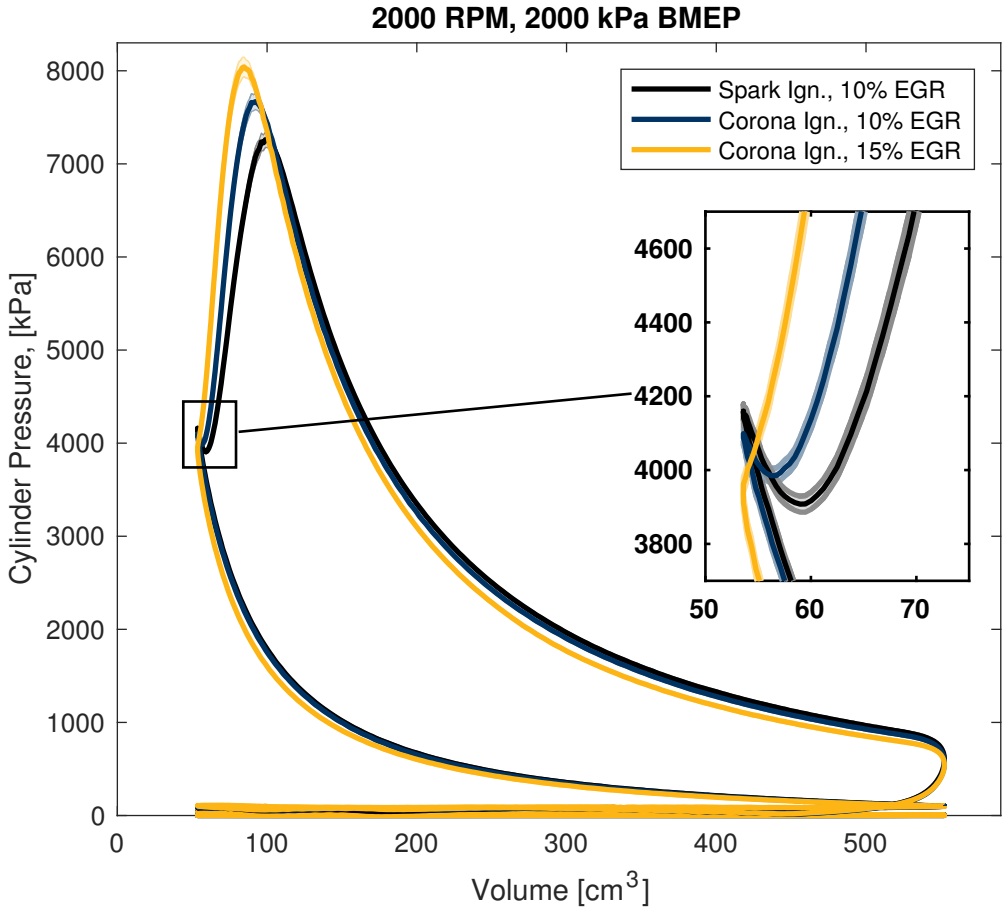

Figure 5.2: Pressure-volume diagram for the boosted loading operation engine experiments discussed in Chapter 3. Black curves are for spark-ignition operation with an EGR rate of 10%, blue curves are for corona discharge ignition operation with an EGR rate of 10%, and gold curves are for corona discharge ignition operation with an EGR rate of 15%.

5.3 Relevance and impact

The work presented in this dissertation is immediately relevant to the transportation energy paradigm discussed in Chapter 1; as mentioned, substantial reductions in transportation fuel consumption are necessary to both curb global anthropogenic climate change and increase energy security. Additionally, as the compression ratios of automotive engines increase, reductions in nitrogen oxide emissions are necessary to mitigate photochemical smog, which has negative effects on human health and the environment, as discussed in Chapter 1. The fact that both fuel consumption and nitrogen oxide emissions were reduced in the engine experiments presented in Chapter 3 is clearly relevant to these goals; however, the implications of the research in the context of automotive engines merit further comment.

Benefits to automotive engines

The research presented is a demonstration of only one of many novel methods to accomplish reductions in fuel consumption and emissions, and other methods discussed in Chapter 1 must also be pursued in tandem. The non-thermal plasma ignition techniques outlined in this dissertation can extend both the lean and the exhaust gas dilution limits of stable engine operation, representing progress both in the long-term goal of implementing lean-burn engines and in the short-term goal of advancing efficiency while continuing use of three-way catalytic converters in consumer automobiles. The engine-specific strategies (National Research Council, 2011; U.S. DRIVE, 2013; Reitz, 2013; National Research Council, 2015) originally outlined in Chapter 1 on which advancements were made in this dissertation are as follows:

- *Downsizing and boosting*: The results of the engine experiments presented in Chapter 3 demonstrate that boosted operation is possible using advanced ignition strategies, and that these strategies can benefit both fuel economy and emissions by extending the knock limit beyond what is possible with traditional inductive spark ignition operation.

- *Stoichiometric gasoline direct injection*: The results of the engine experiments presented in Chapter 3 show that substantial fuel consumption reductions are possible even when keeping overall stoichiometry of combustion at $\phi = 1$. Thus, the strategies make it possible to keep using existing three-way catalytic converter technology to eliminate engine-out pollutants at maximum possible efficiency (Figure 1.6) while lean-burn engines are under development.

- *Increased Exhaust Gas Recirculation*: The corona discharge ignition technique utilized in the experiments in Chapter 3 demonstrated an ability to reliably ignite fuel-air mixtures at greater exhaust gas recirculation rates than is possible with traditional inductive spark ignition technologies. Additionally, the pulsed nanosecond discharge ignition strategy discussed in Chapter 4 has been shown by Sevik et al. (2016) to also extend the exhaust gas recirculation limits of stable engine operation. Thus, both of the advanced ignition techniques discussed in this dissertation have been demonstrated to more reliably ignite more dilute mixtures and subsequently reduce NO_X emissions.

- *Reduced combustion duration*: The results of the experiments in both Chapters 3 and 4 show reduced combustion duration when using advanced ignition strategies, particularly in regards to the earliest stages of flame kernel development. This reduction in flame kernel development time is a significant factor in the improved performance for engines in dilute operating regimes (Sjöberg et al., 2014; Sevik et al., 2016; Pineda, Wolk, Chen and Dibble, 2016), since only relatively modest improvements in flame kernel rise time have been observed so far.

- *Increased hybridization*: Though the research presented in this dissertation does not have a direct impact on the expected increased hybridization in the automotive fleet

over the next 10–15 years, all of the progress made will indirectly increase the efficiency of the engines in these vehicles.

Benefits to ignition technology

The engine operation conditions of the experiments presented in Chapter 3 represent some of the most boosted operating conditions present in the literature for gasoline direct-injection engines with advanced ignition technologies. As discussed in Chapter 2, increased pressure can significantly hinder the accessibility to plasma chemistry beneficial to combustion by decreasing the reduced electric field E/n. While less effective at reducing combustion duration at higher loads, the corona discharge ignition system still provided other benefits, such as extending the knock limit, and this work nonetheless informs future development on corona discharge ignition systems.

The work presented in Chapter 4 has already been used to inform advancements in the research and development of practical pulsed nanosecond discharge ignition technologies for automotive engines; the collaborators in the project have tested refined versions of their technology in research engine experiments with natural gas (Singleton, 2015) and gasoline (Sevik et al., 2016) for stationary power generation and automotive propulsion applications, respectively. Additionally, they have subsequently been able to scale down the technology to fit in a consumer automobile as a drop-in replacement for traditional spark plugs, with generally positive results (Singleton et al., 2017). Importantly, the results presented in Chapter 4 highlight the importance of non-chemical combustion enhancement provided by advanced ignition technologies, and these hydrodynamic effects could be a factor in the sustained success of these techniques in engine-relevant density regimes where E/n is low. This is discussed in more detail in Section 5.4.

5.4 Open questions and future work

This section reviews some concepts about plasma-assisted ignition that merit future efforts in understanding, from both technical and scientific perspectives. Plasma-assisted ignition is still a nascent field, and, much like combustion throughout history, progress is often made on technical fronts with scientific understanding coming later, and vice-versa. This dissertation highlights important questions that will need to be answered by the community to meet the transportation energy goals and global emissions targets.

Engineering and technical considerations

This dissertation adds to the body of literature detailing the use of non-thermal plasma ignition technologies in internal combustion engines, with a specific aim for automotive engines. As discussed in Chapter 1, the automotive industry is currently in a dynamic state,

with dramatic shifts in powertrain technologies and energy sources expected within the next 30 years (National Research Council, 2013).

Advanced ignition with future fuels

The Renewable Fuel Standard in the United States has specified the inclusion of an increasing share of biofuels in the automotive fuel supply (Schnepf and Yacobucci, 2013) and biofuels will play a significant role in reducing the carbon intensity of transportation in the near and far term (Pacala and Socolow, 2004). Additionally, natural gas is experiencing a rise in use for not only power generation, but transportation technologies as well (U.S. Energy Information Administration, 2017), and hydrogen-powered heat engines could enter the transportation sector if the appropriate technical challenges are overcome (U.S. DRIVE, 2013). The performance of non-thermal plasma ignition technologies with these new fuels will need to be examined, particularly since the concentrations and ratios of fuel and air can change dramatically depending on the fuel. For example, for $\phi = 1$, H_2 can make up about 30% of the fuel-air mixture by volume, while for CH_4 this number is about 9.5%, and for iC_8H_{18} (an approximation of gasoline), this number is about 1.7%. If the fast gas heating mechanisms via O_2 and N_2 described in Chapter 2 are critical to non-thermal plasma ignition, they will be less influential in fuel-air mixtures in which the fuel has a larger concentration. Additionally, electron-impact dissociation reactions in which an $\cdot$H atom is abstracted from a fuel molecule will need to be more well-characterized for these new fuels, because the kinetics of ignition and flame propagation are strongly influenced by chain-branching reactions in which $\cdot$H is a reactant (Law, 2006). For these reasons, both fundamental and applied experimental and computational investigations will need undertaking to identify the best use of non-thermal plasma ignition techniques with future fuels and engines.

Model predictive control for non-thermal plasma ignition

The discharge development process described in Chapter 2 is highly sensitive to number density, which can be influenced by temperature and pressure gradients in a combustion environment. The corona discharge ignition system used in the engine experiments presented in Chapter 3 possessed internal circuitry to limit overall current flow and prevent transition to thermal arc, and similar control strategies have been developed for similar systems in the literature (Mariani and Foucher, 2014). Regardless, arcing was still observed for some of the engine cycles, and the frequency of these events was controlled predominantly by manually adjusting the power settings on the system during steady-state engine operation. Much work remains to be done to have this process automated, especially since automotive engines must function at a wide range of speeds and loads to meet driver demands.

The transitions to arcing observed in the constant volume chamber experiments presented in Chapter 4 likewise raise important questions regarding how to best control the evolution of non-thermal plasma discharges for combustion applications. Wolk and Ekoto (2017) have investigated the arcing phenomenon in a concurrent study with a similar pulsed

nanosecond discharge ignition system, and they have been able to determine that the behavior and chemical products of 'primary' and 'secondary' streamers formed in discharges (Ono and Oda, 2003) can be drastically different. In particular, primary streamer discharges in air generate more $\cdot$O atoms than secondary streamer discharges, which are more likely to transition to a thermal arc. In contrast, the secondary steamer discharges have high electrical-to-thermal energy conversion efficiencies, which increase the local gas temperature more than primary streamer discharges. As mentioned in Chapter 4, ignition using the pulsed nanosecond discharge system was not possible in the experiments with only one pulse, and a possible explanation is that even though there was generation of reactive species, the local gas temperature did not increase sufficiently for chain-branching reactions to lead to successful ignition. This presents a control problem—how can discharges be used to simultaneously alter the chemical and thermal environment to generate robust flame kernels?

Scientific and simulation considerations

Concurrent to technical and applied investigations, more fundamental research is needed in plasma-assisted ignition, particularly in regards to the interactions between non-thermal plasma chemistry and ignition chemistry. Many of these fundamental studies are carried out via numerical simulations, which present their own problems, as discussed here.

Combustion simulations with plasma kinetics

Coupling combustion simulations to non-thermal plasma chemistry—particularly for those in which spatial dimensions are considered—presents problems with marrying disparate timescales. Much of the electron-impact chemistry described in Chapter 2 takes place on the order of nanoseconds or less, while ignition chemistry takes place on the order of microseconds to milliseconds depending on the combustion environment. Simulations generally require resolution at the smallest timescale of interest, making three dimensional computational fluid dynamics simulations of non-thermal plasma ignition challenging without creative solutions to separate the timescales. Such is the approach taken by Casey et al. (2017), Castela et al. (2016), and others, who isolate the non-thermal plasma chemistry from the ignition chemistry and fluid transport equations with reasonable success. However, these approaches are limited to simulations of pulsed nanosecond discharges like those discussed in Chapter 4, since these discharges take place for tens of nanoseconds and then cease. For simulations of corona discharges, like those discussed in Chapter 3, this approach is less fruitful, since the discharges last for periods of time that are on the same order as those relevant to combustion chemistry. More clever numerical schemes will be required for dimensional simulations in which non-thermal plasma chemistry is coupled with an automotive engine simulation.

Coupled chemical kinetics and hydrodynamic transport

The imaging results from the engine experiments by Sjöberg et al. (2014) and from the constant volume chamber experiments presented in Chapter 4 show that the hydrodynamic interactions of the developing flame kernels with the unburned fuel-air mixture play a large role in the experimentally observed combustion enhancement. These "jetting" effects are produced by rapid heating of gases between the electrodes, and the interaction of these fast gas heating processes with induced hydrodynamic flow is thus an important consideration for the design of future automotive ignition systems. More experiments with these ignition systems—particularly those that can measure radical species concentrations at highly resolved timescales—will be needed, particularly at engine-relevant number densities and mixture compositions, in order to assess their optimization for production engines.

Additionally, the results of the experiments presented in Chapter 4 highlight that there is a fundamental coupling between the chemical kinetics and hydrodynamic transport; thus, a current problem is distinguishing the relative contributions of chemical kinetic and transport effects to the enhancement of plasma-assisted combustion at a level accessible via numerical simulations. Currently, the transport properties of many of the excited-state species relevant to fast gas heating and plasma-assisted ignition are not known or available in the literature (Bourig et al., 2009). As numerical investigations of plasma-assisted ignition and combustion move to simulations in one or more dimensions, these properties will need to be determined to accurately model these systems and discern their chemical kinetic contribution to any enhancement. A preliminary investigation related to this dissertation (Pineda and Chen, 2016) showed that updating the transport properties of $O_2(a^1\Delta_g)$ and $O_2(b^1\Sigma_g^+)$ in premixed flame simulations changes flame speed calculations by approximately 0.25%, though a subsequent investigation (Pineda, Shi, Casey and Chen, 2017) analyzing the general error associated with transport properties shows that this estimate is within expected modeling uncertainty. Thus, the current discrepancies between models and experiments (Starik et al., 2008; Ombrello et al., 2010; Konnov, 2015) in plasma-assisted combustion are likely due to uncertainties in the chemical kinetic mechanisms rather than in the transport properties.

5.5 Conclusions

The work presented in this dissertation demonstrates that non-thermal plasma ignition is a promising solution to both increase fuel economy and decrease emissions of future automotive engines. However, as automotive engines and fuels evolve, these advanced ignition techniques will need more experimental exploration before implementation in production automotive engines. Additionally, at a more fundamental level, much work remains to be done to understand the beneficial coupling between the detailed non-thermal plasma chemistry and the hydrodynamics associated with these real ignition devices.

Appendix A

Matlab code to generate Otto cycle curves

The following MATLAB code was used to generate the Otto cycle curves of Figure 1.2 in Chapter 1.

```
% generate isentropic curves for gamma = 1.4 (air)
clear
gamma = 1.4;
cp = 1; %kJ/kg-K
v_BDC = 0.5;
oneAtm = 101.325; % kPa/atm
Rair = 0.287; % kJ/kg-K

% use '0' for the 'grid' of isentropic curves
v_TDC_0 = v_BDC/50;
v_comp_0 = 0.525:-0.001:v_TDC_0;

p_0i_1 = 0.5.*oneAtm;
p_0i_2 = 2.5.*oneAtm;
p_0i_3 = 4.5.*oneAtm;
p_0i_4 = 6.5.*oneAtm;
p_0i_5 = 8.5.*oneAtm;
p_0i_6 = 10.5.*oneAtm;
p_0i_7 = 12.5.*oneAtm;
p_0i_8 = 14.5.*oneAtm;
p_0i_9 = 16.5.*oneAtm;

p_0f_1 = p_0i_1.*(v_BDC./v_comp_0).^gamma;
p_0f_2 = p_0i_2.*(v_BDC./v_comp_0).^gamma;
```

```
p_0f_3 = p_0i_3.*(v_BDC./v_comp_0).^gamma;
p_0f_4 = p_0i_4.*(v_BDC./v_comp_0).^gamma;
p_0f_5 = p_0i_5.*(v_BDC./v_comp_0).^gamma;
p_0f_6 = p_0i_6.*(v_BDC./v_comp_0).^gamma;
p_0f_7 = p_0i_7.*(v_BDC./v_comp_0).^gamma;
p_0f_8 = p_0i_8.*(v_BDC./v_comp_0).^gamma;
p_0f_9 = p_0i_9.*(v_BDC./v_comp_0).^gamma;


v_TDC_1 = v_BDC/4;
v_TDC_2 = v_BDC/6;
v_TDC_3 = v_BDC/8;
v_TDC_4 = v_BDC/10;
v_TDC_5 = v_BDC/12;

v_comp_1 = v_BDC:-0.001:v_TDC_1;
v_comp_2 = v_BDC:-0.001:v_TDC_2;
v_comp_3 = v_BDC:-0.001:v_TDC_3;
v_comp_4 = v_BDC:-0.001:v_TDC_4;
v_comp_5 = v_BDC:-0.001:v_TDC_5;

p_i_1 = 1.*oneAtm;
p_f_1 = p_i_1.*(v_BDC./v_comp_1).^gamma;
t_i_1 = 300;
m_a_1 = p_i_1.*v_BDC./(Rair.*t_i_1);
t_f_1 = t_i_1.*(p_f_1./p_i_1).^((gamma-1)/gamma);

p_i_2 = 1.*oneAtm;
p_f_2 = p_i_2.*(v_BDC./v_comp_2).^gamma;
t_i_2 = 300;
m_a_2 = p_i_2.*v_BDC./(Rair.*t_i_2);
t_f_2 = t_i_2.*(p_f_2./p_i_2).^((gamma-1)/gamma);

p_i_3 = 1.*oneAtm;
p_f_3 = p_i_3.*(v_BDC./v_comp_3).^gamma;
t_i_3 = 300;
m_a_3 = p_i_3.*v_BDC./(Rair.*t_i_3);
t_f_3 = t_i_3.*(p_f_3./p_i_3).^((gamma-1)/gamma);

p_i_4 = 1.*oneAtm;
p_f_4 = p_i_4.*(v_BDC./v_comp_4).^gamma;
t_i_4 = 300;
```

```
m_a_4 = p_i_4.*v_BDC./(Rair.*t_i_4);
t_f_4 = t_i_4.*(p_f_4./p_i_4).^((gamma-1)/gamma);

p_i_5 = 1.*oneAtm;
p_f_5 = p_i_5.*(v_BDC./v_comp_5).^gamma;
t_i_5 = 300;
m_a_5 = p_i_5.*v_BDC./(Rair.*t_i_5);
t_f_5 = t_i_5.*(p_f_5./p_i_5).^((gamma-1)/gamma);

% what are the number of kilomoles of air?
%(kJ/m^3)*m^3/(kJ/kmol-K)*K
n_1 = p_f_1(end)*v_TDC_1./(8.314*t_f_1(end));
n_2 = p_f_2(end)*v_TDC_2./(8.314*t_f_2(end));
n_3 = p_f_3(end)*v_TDC_3./(8.314*t_f_3(end));
n_4 = p_f_4(end)*v_TDC_4./(8.314*t_f_4(end));
n_5 = p_f_5(end)*v_TDC_5./(8.314*t_f_5(end));

% what are the required kilomoles of fuel (methane?)?
nf_1 = (0.21*n_1)/2;
nf_2 = (0.21*n_2)/2;
nf_3 = (0.21*n_3)/2;
nf_4 = (0.21*n_4)/2;
nf_5 = (0.21*n_5)/2;

% what is energy contained in fuel?
Q_1 = 1000.*800*nf_1; % kJ/kmol
Q_2 = 1000.*800*nf_2; % kJ/kmol
Q_3 = 1000.*800*nf_3; % kJ/kmol
Q_4 = 1000.*800*nf_4; % kJ/kmol
Q_5 = 1000.*800*nf_5; % kJ/kmol



t_c_1 = t_f_1(end) + Q_1/(m_a_1*cp);
t_c_2 = t_f_2(end) + Q_2/(m_a_2*cp);
t_c_3 = t_f_3(end) + Q_3/(m_a_3*cp);
t_c_4 = t_f_4(end) + Q_4/(m_a_4*cp);
t_c_5 = t_f_5(end) + Q_5/(m_a_5*cp);

% how much does that increase the pressure?
p_c_1 = m_a_1*Rair*t_c_1/v_TDC_1;
p_c_2 = m_a_2*Rair*t_c_2/v_TDC_2;
```

```
p_c_3 = m_a_3*Rair*t_c_3/v_TDC_3;
p_c_4 = m_a_4*Rair*t_c_4/v_TDC_4;
p_c_5 = m_a_5*Rair*t_c_5/v_TDC_5;

% now we must expand isentropically
v_exp_1 = fliplr(v_comp_1);
v_exp_2 = fliplr(v_comp_2);
v_exp_3 = fliplr(v_comp_3);
v_exp_4 = fliplr(v_comp_4);
v_exp_5 = fliplr(v_comp_5);

p_e_1 = p_c_1.*(v_TDC_1./v_exp_1).^gamma;
p_e_2 = p_c_2.*(v_TDC_2./v_exp_2).^gamma;
p_e_3 = p_c_3.*(v_TDC_3./v_exp_3).^gamma;
p_e_4 = p_c_4.*(v_TDC_4./v_exp_4).^gamma;
p_e_5 = p_c_5.*(v_TDC_5./v_exp_5).^gamma;

% assemble vectors
v_1_total = [v_comp_1(1:end-1) v_TDC_1 ...
v_TDC_1 v_exp_1(2:end) v_BDC];
v_2_total = [v_comp_2(1:end-1) v_TDC_2 ...
v_TDC_2 v_exp_2(2:end) v_BDC];
v_3_total = [v_comp_3(1:end-1) v_TDC_3 ...
v_TDC_3 v_exp_3(2:end) v_BDC];
v_4_total = [v_comp_4(1:end-1) v_TDC_4 ...
v_TDC_4 v_exp_4(2:end) v_BDC];
v_5_total = [v_comp_5(1:end-1) v_TDC_5 ...
v_TDC_5 v_exp_5(2:end) v_BDC];

p_1_total = [p_f_1(1:end-1) p_f_1(end) ...
p_c_1 p_e_1(2:end) p_i_1];
p_2_total = [p_f_2(1:end-1) p_f_2(end) ...
p_c_2 p_e_2(2:end) p_i_2];
p_3_total = [p_f_3(1:end-1) p_f_3(end) ...
p_c_3 p_e_3(2:end) p_i_3];
p_4_total = [p_f_4(1:end-1) p_f_4(end) ...
p_c_4 p_e_4(2:end) p_i_4];
p_5_total = [p_f_5(1:end-1) p_f_5(end) ...
p_c_5 p_e_5(2:end) p_i_5];

% calculate work output
```

```
w_1 = trapz(v_1_total, p_1_total);
w_2 = trapz(v_2_total, p_2_total);
w_3 = trapz(v_3_total, p_3_total);
w_4 = trapz(v_4_total, p_4_total);
w_5 = trapz(v_5_total, p_5_total);

eta_1 = w_1./Q_1
eta_2 = w_2./Q_2
eta_3 = w_3./Q_3
eta_4 = w_4./Q_4
eta_5 = w_5./Q_5

%%
figure;
hold on;
set(gca, 'FontSize',10);
set(gca,'box','on');

plot(v_comp_0, p_0f_1./1000, '-.', 'Color', [0.7 0.7 0.7]);
plot(v_comp_0, p_0f_2./1000, '-.', 'Color', [0.7 0.7 0.7]);
plot(v_comp_0, p_0f_3./1000, '-.', 'Color', [0.7 0.7 0.7]);
plot(v_comp_0, p_0f_4./1000, '-.', 'Color', [0.7 0.7 0.7]);
plot(v_comp_0, p_0f_5./1000, '-.', 'Color', [0.7 0.7 0.7]);
plot(v_comp_0, p_0f_6./1000, '-.', 'Color', [0.7 0.7 0.7]);
plot(v_comp_0, p_0f_7./1000, '-.', 'Color', [0.7 0.7 0.7]);
plot(v_comp_0, p_0f_8./1000, '-.', 'Color', [0.7 0.7 0.7]);
plot(v_comp_0, p_0f_9./1000, '-.', 'Color', [0.7 0.7 0.7]);


berkeleyColorPalette

leg5 = plot(v_5_total, p_5_total./1000, ...
'LineWidth', 2, 'Color', berkeleyBlue);
leg4 = plot(v_4_total, p_4_total./1000, ...
'LineWidth', 2, 'Color', californiaGoldLight);
leg3 = plot(v_3_total, p_3_total./1000, ...
'LineWidth', 2, 'Color', berkeleyBlueDark);
leg2 = plot(v_2_total, p_2_total./1000, ...
'LineWidth', 2, 'Color', berkeleyBlueLight);
leg1 = plot(v_1_total, p_1_total./1000, ...
'LineWidth', 2, 'Color', californiaGoldDark);
```

```
l_5 = ['Compression Ratio = 12, \eta = ', ...
num2str(round(100*eta_5)/100)];
l_4 = ['Compression Ratio = 10, \eta = ', ...
num2str(round(100*eta_4)/100)];
l_3 = ['Compression Ratio = ', '  ', '8, \eta = ', ...
num2str(ceil(100*eta_3)/100)];
l_2 = ['Compression Ratio = ', '  ', '6, \eta = ', ...
num2str(ceil(100*eta_2)/100)];
l_1 = ['Compression Ratio = ', '  ', '4, \eta = ', ...
num2str(ceil(100*eta_1)/100)];

legend([leg5 leg4 leg3 leg2 leg1], ...
{l_5, l_4, l_3, l_2, l_1}, 'Location', 'NorthEast');

xlim([25 525]./1000);
ylim([0 160].*101.325./1000);
title('Idealized otto cycle')
ylabel('Pressure [MPa]');
xlabel('Volume [m^3]');

annotation('textarrow',[0.5 0.3],[0.37 0.17],'String','Compression')
annotation('textarrow',[0.4 0.25],[0.5 0.4],'String','Power')
annotation('textarrow',[0.33 0.16],[0.6 0.5],'String','Ignition')

print('./figures/idealOttoCyclePV.eps', '-depsc');
```

The MATLAB code depends on the file, `berkeleyColorPalette.m`, detailed below:

```
% establish Berkeley color palette
% written by Daniel Pineda

% converted RGB values from HEX from brand.berkeley.edu
berkeleyBlue = [0 50 98]./255;
californiaGold = [253 181 21]./255;

% change the number of shades to divide the color into for EACH light and
% dark shades
numShadesBlue = 4;
numShadesGold = 4;

% use linspace to establish variation from colors to white
blueMapLight = [linspace(berkeleyBlue(1), 1, numShadesBlue)', ...
linspace(berkeleyBlue(2), 1, numShadesBlue)', ...
linspace(berkeleyBlue(3), 1, numShadesBlue)'];
goldMapLight = [linspace(californiaGold(1), 1, numShadesGold)', ...
linspace(californiaGold(2), 1, numShadesGold)', ...
linspace(californiaGold(3), 1, numShadesGold)'];

% use linspace to establish variation from colors to black
blueMapDark = [linspace(berkeleyBlue(1), 0, numShadesBlue)', ...
linspace(berkeleyBlue(2), 0, numShadesBlue)', ...
linspace(berkeleyBlue(3), 0, numShadesBlue)'];
goldMapDark = [linspace(californiaGold(1), 0, numShadesGold)', ...
linspace(californiaGold(2), 0, numShadesGold)', ...
linspace(californiaGold(3), 0, numShadesGold)'];

% assign light colors
berkeleyBlueLight = blueMapLight(2,:);
berkeleyBlueLighter = blueMapLight(3,:);
californiaGoldLight = goldMapLight(2,:);
californiaGoldLighter = goldMapLight(3,:);

% assign dark colors
berkeleyBlueDark = blueMapDark(2,:);
berkeleyBlueDarker = blueMapDark(3,:);
californiaGoldDark = goldMapDark(2,:);
californiaGoldDarker = goldMapDark(3,:);
```

Appendix B

Python code for Cantera simulations

In Chapters 1 and 2, several figures included plots of flame speeds and ignition delay times calculated using the open-source chemical kinetics software package CANTERA, by Goodwin et al. (2014). The version used throughout this dissertation is version 2.2.0. This appendix details the Python 2.7 code used to generate the data used in those plots. All simulations requiring the use of chemistry used the GRI-MECH 3.0 mechanism by Smith et al. (1999).

B.1 Chapter 1 figures

Figure 1.3 used the following code:

```
"""
A freely-propagating, premixed methane flat flame
adapted from:
http://www.cantera.org/docs/sphinx/html/cython/examples/onedim_adiabatic_flame.html
"""

import cantera as ct
import numpy as np

# Simulation parameters for flame speed
p = 101325
Tin = 300
# simulation parameters for ignition delay
Tinit_ig = 1000
Pinit_ig = 101325
# coal gas composition
#H2frac = 0.504
#COfrac = 0.078
#CH4frac = 0.315
```

```
#N2frac = 0.062
#CO2frac = 0.041
# natural gas composition
H2frac = 0
COfrac = 0
CH4frac = 1
N2frac = 0
CO2frac = 0
fuelReactNames = ['H2', 'CO', 'CH4', 'N2', 'CO2']
fuelReactArray = [H2frac, COfrac, CH4frac, N2frac, CO2frac]
fuelReactants = 'H2:' + str(fuelReactArray[0]) + ', CO:' \
+ str(fuelReactArray[1]) + ', CH4:' + str(fuelReactArray[2]) \
+ ', N2:' + str(fuelReactArray[3]) + ', CO2:' \
+ str(fuelReactArray[4])
gas = ct.Solution('gri30.xml')
gas.X = fuelReactants

# how many moles of O2 for each of the fuels?
O2_stoich_vector = np.zeros(len(fuelReactNames))
for i, fuelName in enumerate(fuelReactNames):
    O2_stoich_vector[i] =  gas.X[gas.species_index(fuelName)] \
     * (gas.n_atoms(fuelName,'C') + 0.25*gas.n_atoms(fuelName,'H') \
     - 0.50*gas.n_atoms(fuelName,'O'))
O2_stoich = sum(O2_stoich_vector)
phis = np.linspace(0.70,1.3,31)
Sus = np.zeros(len(phis))
Tads = np.zeros(len(phis))
tigns = np.zeros(len(phis))
for i, phi in enumerate(phis):
    newX= 'H2:' + str((fuelReactArray[0]*phi/O2_stoich)) + ', CO:' \
     +  str((fuelReactArray[1]*phi/O2_stoich)) + ', CH4:' \
     + str((fuelReactArray[2]*phi/O2_stoich)) + ', CO2:' \
     + str((fuelReactArray[4]*phi/O2_stoich)) +  ', O2:1.0, N2:' \
     + str((3.76 + fuelReactArray[3]*phi/O2_stoich))

    print(" ");
    print("Starting flame speed calculation for phi =" + str(phi))
    # flame simulation
    initial_grid = np.linspace(0.0, 0.02, 10)  # m
    tol_ss = [1.0e-5, 1.0e-13]  # [rtol atol] for steady-state problem
    tol_ts = [1.0e-4, 1.0e-13]  # [rtol atol] for time stepping
    loglevel = 1  # amount of diagnostic output (0 to 8)
```

```
refine_grid = True  # 'True' to enable refinement, 'False' to disable

# IdealGasMix object used to compute mixture properties,
# set to the state of the upstream fuel-air mixture
flameGas = ct.Solution('gri30.xml')
flameGas.TPX = Tin, p, newX

# Flame object
f = ct.FreeFlame(flameGas, initial_grid)
f.flame.set_steady_tolerances(default=tol_ss)
f.flame.set_transient_tolerances(default=tol_ts)

# Solve with the energy equation enabled
f.set_refine_criteria(ratio=3, slope=0.06, curve=0.12)
f.energy_enabled = True
try:
    f.solve(loglevel=loglevel, refine_grid=refine_grid)
except:
    # initial grid failed, try a finer grid
    initial_grid = np.linspace(0.0, 0.02, 30)  # m
    flameGas = ct.Solution('gri30.xml')
    flameGas.TPX = Tin, p, newX
    f = ct.FreeFlame(flameGas, initial_grid)
    f.flame.set_steady_tolerances(default=tol_ss)
    f.flame.set_transient_tolerances(default=tol_ts)
    # Solve with the energy equation enabled
    f.set_refine_criteria(ratio=3, slope=0.06, curve=0.12)
    f.energy_enabled = True
    f.solve(loglevel=loglevel, refine_grid=refine_grid)

# store the flame speed and the adiabatic flame temperature
Sus[i] = f.u[0]
Tads[i] = f.T[-1]
print("Calculated Flame Speed is =" + str(Sus[i]))
print(" ");
print("Starting ignition delay calculation for phi =" + str(phi))
# ignition delay simulation
igGas = ct.Solution('gri30.xml')
igGas.TPX = Tinit_ig, Pinit_ig, newX
r = ct.IdealGasConstPressureReactor(igGas)
sim = ct.ReactorNet([r])
time = 0.0
```

```
numSteps = 10000
times = np.zeros(numSteps)
tIgn = 0
for n in range(numSteps):
    time += 1.e-5
    sim.advance(time)
    times[n] = time * 1e3 # time in ms
    #data[n,0] = r.T
    if ((r.T - Tinit_ig) > 400) and (tIgn == 0):
        tIgn = time*1e3
        print("Calculated Ignition Delay is =" + str(tIgn))
tigns[i] = tIgn
```

B.2 Chapter 2 figures

The data in Figure 2.1 was generated using the same code as for the data in Figure 1.3. The data in Figure 2.2, however, was generated using the code below:

```
"""
A freely-propagating, premixed methane flat flame
adapted from:
http://www.cantera.org/docs/sphinx/html/cython/examples/onedim_adiabatic_flame.html
"""

import cantera as ct
import numpy as np

# Simulation parameters for flame speed - EGR mixtures - just add CO2 + N2
# for now, hard code for methane
p = 101325
Tin = 300
# simulation parameters for ignition delay
Tinit_ig = 1200
Pinit_ig = 101325
# natural gas composition
H2frac = 0
COfrac = 0
CH4frac = 1
N2frac = 0
CO2frac = 0
fuelReactNames = ['H2', 'CO', 'CH4', 'N2', 'CO2']
fuelReactArray = [H2frac, COfrac, CH4frac, N2frac, CO2frac]
fuelReactants = 'H2:' + str(fuelReactArray[0]) + ', CO:' \
+ str(fuelReactArray[1]) + ', CH4:' + str(fuelReactArray[2]) \
+ ', N2:' + str(fuelReactArray[3]) + ', CO2:' \
+ str(fuelReactArray[4])
gas = ct.Solution('gri30.xml')
gas.X = fuelReactants

# how many moles of O2 for each of the fuels?
O2_stoich_vector = np.zeros(len(fuelReactNames))
for i, fuelName in enumerate(fuelReactNames):
    O2_stoich_vector[i] =  gas.X[gas.species_index(fuelName)] \
     * (gas.n_atoms(fuelName,'C') + 0.25*gas.n_atoms(fuelName,'H') \
     - 0.50*gas.n_atoms(fuelName,'O'))
```

```
O2_stoich = sum(O2_stoich_vector)

EGRs = np.linspace(0.00,0.40,21)
phi = 1.00
Sus = np.zeros(len(EGRs))
Tads = np.zeros(len(EGRs))
tigns = np.zeros(len(EGRs))
for i, EGR in enumerate(EGRs):
    newX= 'H2:' + str((fuelReactArray[0]*phi/O2_stoich)) + ', CO:' \
      +  str((fuelReactArray[1]*phi/O2_stoich)) + ', CH4:' \
      + str((fuelReactArray[2]*phi/O2_stoich)) + ', CO2:' \
      + str((EGR*fuelReactArray[2]*phi/O2_stoich)/(1-EGR)) \
      +  ', O2:1.0, N2:' + str((1 + EGR/(1-EGR))*(3.76 \
      + fuelReactArray[3]*phi/O2_stoich))

    nCO2 = (EGR*fuelReactArray[2]*phi/O2_stoich)/(1-EGR)
    print(" ");
    print(" EGR% sanity check=" + str(100*(nCO2)/(0.5 + nCO2)))


    print(" ");
    print("Starting flame speed calculation for EGR% =" + str(100*EGR))
    # flame simulation
    initial_grid = np.linspace(0.0, 0.02, 10)  # m
    tol_ss = [1.0e-5, 1.0e-13]  # [rtol atol] for steady-state problem
    tol_ts = [1.0e-4, 1.0e-13]  # [rtol atol] for time stepping
    loglevel = 1  # amount of diagnostic output (0 to 8)
    refine_grid = True  # 'True' to enable refinement, 'False' to disable

    # IdealGasMix object used to compute mixture properties,
    # set to the state of the upstream fuel-air mixture
    flameGas = ct.Solution('gri30.xml')
    flameGas.TPX = Tin, p, newX

    # Flame object
    f = ct.FreeFlame(flameGas, initial_grid)
    f.flame.set_steady_tolerances(default=tol_ss)
    f.flame.set_transient_tolerances(default=tol_ts)

    # Solve with the energy equation enabled
    f.set_refine_criteria(ratio=3, slope=0.06, curve=0.12)
    f.energy_enabled = True
```

```
try:
    f.solve(loglevel=loglevel, refine_grid=refine_grid)
except:
    # initial grid failed, try a finer grid
    initial_grid = np.linspace(0.0, 0.02, 30)  # m
    flameGas = ct.Solution('gri30.xml')
    flameGas.TPX = Tin, p, newX
    f = ct.FreeFlame(flameGas, initial_grid)
    f.flame.set_steady_tolerances(default=tol_ss)
    f.flame.set_transient_tolerances(default=tol_ts)
    # Solve with the energy equation enabled
    f.set_refine_criteria(ratio=3, slope=0.06, curve=0.12)
    f.energy_enabled = True
    f.solve(loglevel=loglevel, refine_grid=refine_grid)

# store the flame speed and the adiabatic flame temperature
Sus[i] = f.u[0]
Tads[i] = f.T[-1]
print("Calculated Flame Speed is =" + str(Sus[i]))
print(" ");
print("Starting ignition delay calculation for EGR% =" + str(100*EGR))
# ignition delay simulation
igGas = ct.Solution('gri30.xml')
igGas.TPX = Tinit_ig, Pinit_ig, newX
r = ct.IdealGasConstPressureReactor(igGas)
sim = ct.ReactorNet([r])
time = 0.0
numSteps = 10000
times = np.zeros(numSteps)
#data = np.zeros((numSteps, 4))
tIgn = 0
for n in range(numSteps):
    time += 1.e-5
    sim.advance(time)
    times[n] = time * 1e3 # time in ms
    #data[n,0] = r.T
    if ((r.T - Tinit_ig) > 400) and (tIgn == 0):
        tIgn = time*1e3
        print("Calculated Ignition Delay is =" + str(tIgn))
tigns[i] = tIgn
```

The data in Figure 2.7 was generated using the code below, along with initial conditions discerned from the work of Kosarev et al. (2008) in an attempt to replicate their results:

```
import cantera as ct
import numpy as np
Tinit_ig = 1530
Pinit_ig = 110000

igGas = ct.Solution('gri30.xml')
# Use gas mixtures estimated from Kosarev (2008)
#igGas.TPX = Tinit_ig, Pinit_ig, "CH4:3.3,O2:6.7,AR:90"
igGas.TPX = Tinit_ig, Pinit_ig, \
"CH4:3.1929,O2:6.5845,AR:90,O:0.231, H:0.109, \
CH3:9.31E-2, CH2:1E-2, H2:6E-3, CH:4E-3"
r = ct.IdealGasConstPressureReactor(igGas)
sim = ct.ReactorNet([r])
time = 0.0
numSteps = 100000
times = np.zeros(numSteps)
data = np.zeros((numSteps, 11))
tIgn = 0
for n in range(numSteps):
    time += 1.e-7
    sim.advance(time)
    times[n] = time * 1e6 # time in us
    data[n,0] = r.T
    if ((r.T - Tinit_ig) > 400) and (tIgn == 0):
        tIgn = time*1e3
        print("Calculated Ignition Delay is =" + str(tIgn))
    data[n,1:] = \
     r.thermo['OH', 'H', 'O','H2','CH3', 'CH4', 'O2','H2O','CO','CO2'].X
tigns = tIgn

np.savetxt("data.csv", data, delimiter=",")
```

Appendix C

Uncertainty analysis for engine experiments

An uncertainty analysis is given in this section for the following values and calculations reported in Chapter 3: EGR rate, in-cylinder pressure, cylinder volume, net heat release rate, total cumulative net heat release, combustion phasing, BSFC, in-cylinder temperature, and brake-specific emissions. For each of these values, the uncertainty was calculated according to the general formula in Equation C.1 (Mandel, 1964; Coleman and Steele, 2009), similar to the engine data uncertainty analysis performed by Rapp et al. (2012):

$$U_r = \sqrt{\left(\frac{\partial r}{\partial x_1} U_{x_1}\right)^2 + \left(\frac{\partial r}{\partial x_2} U_{x_2}\right)^2 + \cdots + \left(\frac{\partial r}{\partial x_n} U_{x_n}\right)^2} \tag{C.1}$$

where the uncertainty U_r is being calculated for the quantity r and x_n are the variables on which r depends. This formula assumes that the uncertainties for x_n, U_{x_n}, are independent of one another and this can be added in quadrature. For all measurement uncertainties with repeated measurements, U_{x_n} is calculated similarly as the square root of the sum of squares of the systematic uncertainty S_{x_n} and the random uncertainty R_{x_n} according to Equation C.2.

$$U_{x_n} = \sqrt{S_{x_n}^2 + R_{x_n}^2} \tag{C.2}$$

The systematic uncertainty for the measurement device is specified by the manufacturer and the random uncertainty is calculated using the 95% confidence interval (Mandel, 1964) according to Equation C.3,

$$R_{x_n} = t_{95\%} \frac{\sigma_{x_n}}{\sqrt{N}} \tag{C.3}$$

where N is the number of measurements (in Chapter 3, $N = 300$), σ_{x_n} is the standard deviation of the measurements, and $t_{95\%}$ is the value of the Student's t, which for 300 measurements is $t = 1.9679$.

C.1 In-cylinder pressure

The uncertainty in in-cylinder pressure, U_P, is calculated by applying Equation C.2:

$$U_P = \sqrt{S_P^2 + R_P^2} \tag{C.4}$$

where the systematic uncertainty of the Kistler 6043Asp pressure transducer is specified as ± 20 kPa, and the random uncertainty is calculated according to Equation C.3 over 300 cycles.

C.2 Volume

The volume at each crank angle is calculated by the slider-crank formula (Heywood, 1988), expressed in Equation C.5:

$$V = V_C + \frac{\pi B^2}{4}\left(l + a - a \cdot \cos\theta - \left(l^2 - a^2 \cdot \sin^2\theta\right)^{1/2}\right) \tag{C.5}$$

where V_C is the clearance volume when the piston is at top dead center, B is the bore diameter, l is the length of the connecting rod, a is the crank radius, and θ is the crank angle degree. The uncertainty in volume is then given by applying Equation C.1 to Equation C.5:

$$U_V = \frac{\partial V}{\partial \theta} U_\theta \tag{C.6}$$

where U_θ is the uncertainty in crank angle degree, which for the results in Chapter 3 is ± 0.5 °CA. $\partial V/\partial\theta$ is evaluated by taking the partial derivative of Equation C.5 with respect to θ and Equation C.6 becomes Equation C.7.

$$U_V = \frac{\pi B^2}{4}\left(a \cdot \sin\theta + \frac{a^2 \sin\theta\cos\theta}{\sqrt{l^2 - a^2 \cdot \sin^2\theta}}\right) \cdot U_\theta \tag{C.7}$$

C.3 Net heat release rate and total cumulative net heat release

The net heat release rate is calculated according to Equation 3.1. The uncertainty in net HRR, U_{HRR}, is calculated by applying Equation C.1 to Equation 3.1 to get Equation C.8:

$$U_{HRR}^2 = \left(\frac{\partial HRR}{\partial P} U_P\right)^2 + \left(\frac{\partial HRR}{\partial \gamma} U_\gamma\right)^2 + \left(\frac{\partial HRR}{\partial V} U_V\right)^2 \tag{C.8}$$

where U_P and U_V are given by Equations C.4 and C.7, respectively, and U_γ is calculated using Equation C.3; U_γ is assumed to be dominated by the random uncertainty associated with

calculating γ for each of the 300 cycles. Carrying out the partial derivatives and simplifying, Equation C.8 becomes Equation C.9.

$$U_{HRR}^2 = \left(\left(\frac{\gamma}{\gamma-1}\cdot\frac{dV}{d\theta}\right)U_P\right)^2 + \left(\left(\frac{P}{(\gamma-1)^2}\cdot\frac{dV}{d\theta} + \frac{V}{(\gamma-1)^2}\cdot\frac{dP}{d\theta}\right)U_\gamma\right)^2 + \left(\left(\frac{1}{\gamma-1}\cdot\frac{dP}{d\theta}\right)U_V\right)^2 \tag{C.9}$$

For the uncertainty in cumulative net heat release, U_{HR}, Equation C.9 is numerically integrated over θ using the trapezoidal method of integration; thus, U_{HR} generally increases with θ for the θ of interest.

C.4 Combustion phasing

Values of CA10, CA50, and CA90 (collectively, CAxx) were calculated by locating the crank angle where 10%, 50%, and 90% of the total net cumulative heat release was reached for each of the 300 cycles. The uncertainty in these combustion phasing values CAxx is calculated by applying Equation C.2:

$$U_{CAxx} = \sqrt{U_\theta^2 + R_{CAxx}^2} \tag{C.10}$$

where U_θ is the systematic uncertainty in crank angle, $\pm$ 0.5 °CA, and R_{CAxx} is the random uncertainty in the combustion phasing calculated from Equation C.3 for the 300 cycles. For the burn duration angles, such as burning angle $\Delta\theta_b$, which is calculated from CA90 - CA10, the uncertainties are summed (Mandel, 1964), e.g.:

$$U_{\Delta\theta_b} = U_{CA90} + U_{CA10} \tag{C.11}$$

C.5 Exhaust gas recirculation rate

The Equation for calculating the EGR rate used in Chapter 3 is given by both Equation 2.18 and Equation 3.3. The uncertainty, U_{EGR}, is calculated by applying Equation C.1 to Equations 2.18 and 3.3:

$$U_{EGR}^2 = \left(\frac{\partial EGR}{\partial X_{\mathrm{CO_2},in}}U_{X_{\mathrm{CO_2},in}}\right)^2 + \left(\frac{\partial EGR}{\partial X_{\mathrm{CO_2},exh}}U_{X_{\mathrm{CO_2},exh}}\right)^2 \tag{C.12}$$

where $U_{X_{\mathrm{CO_2},in}}$ and $U_{X_{\mathrm{CO_2},exh}}$ are the uncertainties in the mole fraction of CO_2 in the intake and exhaust manifolds, respectively, which are both assumed to be equal to $\pm$ 1000 ppm in this thesis, converted to mole fractions in these equations. Evaluating the partial derivatives and simplifying, Equation C.12 becomes Equation C.13:

$$U_{EGR}^2 = \left(\frac{100\cdot U_{X_{\mathrm{CO_2}}}}{X_{\mathrm{CO_2},exh} - X_{\mathrm{CO_2},amb}}\right)^2 \cdot \left(1 + \left(\frac{EGR}{100}\right)^2\right) \tag{C.13}$$

where the factors of 100 are added to convert the final value to a percentage.

C.6 Brake-specific fuel consumption

Brake-specific fuel consumption is calculated by the mass flow rate of fuel $\dot{m}_f$ divided by the brake power produced by the engine, which is equal to the brake torque $\mathcal{T}$ times the speed of the engine, ω. The uncertainty in BSFC, U_{BSFC}, can be calculated by applying Equation C.1:

$$U_{BSFC}^2 = \left(\frac{\partial BSFC}{\partial \dot{m}_f} U_{\dot{m}_f}\right)^2 + \left(\frac{\partial BSFC}{\partial \mathcal{T}} U_{\mathcal{T}}\right)^2 + \left(\frac{\partial BSFC}{\partial \omega} U_{\omega}\right)^2 \tag{C.14}$$

where $U_{\dot{m}_f}$ is given by the systematic uncertainty in the fuel flow meter (0.8% of the total flow rate), $U_{\mathcal{T}}$ is given by the systematic uncertainty of the torque meter (0.05% of the measured value), and U_{ω} is the systematic uncertainty in the engine speed ($\pm$ 2 RPM). Evaluating the partial derivatives and simplifying, Equation C.14 becomes Equation C.15:

$$U_{BSFC}^2 = \left(\frac{1}{\mathcal{T}\omega}\right)^2 \left(U_{\dot{m}_f}^2 + \left(\frac{\dot{m}_f}{\mathcal{T}} U_{\mathcal{T}}\right)^2 + \left(\frac{\dot{m}_f}{\omega} U_{\omega}\right)^2\right) \tag{C.15}$$

C.7 Estimated in-cylinder temperature

The estimated in-cylinder temperature is calculated according to Equation 3.2 in Chapter 3, and it depends on the mass of the gases in the cylinder m_{ch}, which has its own uncertainty since it is estimated by dividing the sum of the mass flow rates of air, fuel, and EGR by the frequency of engine cycles (which for four-stroke engines is equal to $\omega/2$), as in Equation C.16:

$$m_{ch} = \frac{2}{\omega}\left(\dot{m}_{air} + \dot{m}_{EGR} + \dot{m}_f\right) \tag{C.16}$$

The uncertainty in m_{ch} can be calculated by applying Equation C.1 to Equation C.16, and the evaluated and simplified form is presented in Equation C.17:

$$U_{m_{ch}}^2 = \left(\frac{2}{\omega}\right)^2 \left(U_{\dot{m}_{air}}^2 + U_{\dot{m}_{EGR}}^2 + U_{\dot{m}_f}^2 + \left(\frac{m_{ch}}{2} U_{\omega}\right)^2\right) \tag{C.17}$$

The uncertainty for in-cylinder temperature, U_T, can then be calculated by applying Equation C.1.

$$U_T^2 = \left(\frac{\partial T}{\partial P} U_P\right)^2 + \left(\frac{\partial T}{\partial V} U_V\right)^2 + \left(\frac{\partial T}{\partial m_{ch}} U_{m_{ch}}\right)^2 \tag{C.18}$$

After evaluating the partial derivatives and simplifying, Equation C.18 becomes Equation C.19.

$$U_T^2 = \left(\frac{1}{m_{ch} R}\right)^2 \left((V U_P)^2 + (P U_V)^2 + \left(\frac{PV}{m_{ch}} U_{m_{ch}}\right)^2\right) \tag{C.19}$$

C.8 Brake-specific emissions

For the results in Chapter 3, the uncertainties for the mole fractions of specific pollutants i, U_{X_i} were calculated based on the uncertainty estimates (e.g. 1% of the full scale) for the ranges used on the emissions measurement system. The uncertainty for nitrogen oxide (NO_X) measurement is approximately 25 ppm (5 ppm for the 4000 rpm / 2000 kPa BMEP results); 100 ppm for carbon monoxide (CO) (1000 ppm for the 4000 rpm / 2000 kPa BMEP results); 25 ppm for unburned hydrocarbons (UHC) (35 ppm for the 2000 rpm / 2000 kPa BMEP results); and 1000 ppm for carbon dioxide (CO_2). Brake-specific emissions for pollutant i are calculated using formula in Equation C.20:

$$E_i = \frac{\dot{m}_{exh} X_i}{\mathcal{T}\omega} \frac{M_i}{M_{mix}} \tag{C.20}$$

where $\dot{m}_{exh}$ is the mass flow rate of the exhaust, X_i, is the measured mole fraction of the pollutant, M_i is the molecular weight of the pollutant, and M_{mix} is the mixture-averaged molecular weight of the exhaust stream. The uncertainty in the brake-specific emissions can be calculated by applying Equation C.1 to Equation C.20, and, after simplification, becomes Equation C.21:

$$U_{e_i}^2 = \left(\frac{\dot{m}_{exh} X_i}{\mathcal{T}\omega} \frac{M_i}{M_{mix}}\right)^2 \left(\left(\frac{U_{X_i}}{X_i}\right)^2 + \left(\frac{U_{\dot{m}_{exh}}}{\dot{m}_{exh}}\right)^2 + \left(\frac{U_{\mathcal{T}}}{\mathcal{T}}\right)^2 + \left(\frac{U_\omega}{\omega}\right)^2\right) \tag{C.21}$$

Bibliography

Adamovich, I. V., Li, T. and Lempert, W. R. (2015). Kinetic mechanism of molecular energy transfer and chemical reactions in low-temperature air-fuel plasmas, *Philosophical Transactions of the Royal Society A: Mathematical, Physical and Engineering Sciences* **373**(2048): 20140336.

Aleksandrov, N. L., Kindysheva, S. V., Kosarev, I. N., Starikovskaia, S. M. and Starikovskiy, A. Y. (2009). Mechanism of ignition by non-equilibrium plasma, *Proceedings of the Combustion Institute* **32**(1): 205–212.

Altshuler, A., Anderson, M., Jones, D., Roos, D. and Womack, J. (1984). *The Future of the Automobile*, The MIT Press, Cambridge, MA.

Amann, C. A. (1989). The Automotive Spark-Ignition Engine – An Historical Perspective, *in* E. F. C. Somerscales and A. A. Zagotta (eds), *History of the Internal Combustion Engine*, The American Society of Mechanical Engineers, New York, NY, pp. 33–45.

Anslyn, E. V. and Dougherty, D. A. (2006). *Modern Physical Organic Chemistry*, University Science Books.

Arrhenius, S. (1896). On the Influence of Carbonic Acid in the Air upon the Temperature of the Ground, *Philosophocal Magazine and Journal of Science* **41**(5): 237–276.

Asik, J. R. and Bates, B. (1976). The Ferroresonant Capacitor Discharge Ignition (FCDI) System: A Multiple Firing CD Ignition with Spark Discharge Sustaining Between Firings, pp. 1–12.

Bak, M. S., Kim, W. and Cappelli, M. A. (2011). On the quenching of excited electronic states of molecular nitrogen in nanosecond pulsed discharges in atmospheric pressure air, *Applied Physics Letters* **98**(1): 011502.

Ball, M. and Wietschel, M. (2009). The future of hydrogen opportunities and challenges, *International Journal of Hydrogen Energy* **34**(2): 615–627.

Barnola, J. M., Raynaud, D., Korotkevich, Y. S. and Lorius, C. (1987). Vostok ice core provides 160,000-year record of atmospheric CO2, *Nature* **329**(6138): 408–414.

Barraza-Botet, C. L., Wagnon, S. W. and Wooldridge, M. S. (2016). Combustion Chemistry of Ethanol: Ignition and Speciation Studies in a Rapid Compression Facility, *The Journal of Physical Chemistry A* p. acs.jpca.6b06725.

Beaton, K. (1957). *Enterprise in Oil: A History of Shell Oil in the United States*, Appleton-Century-Crofts, Inc, New York, NY.

Berhane, K., Chang, C.-C., McConnell, R., Gauderman, W. J., Avol, E., Rapapport, E., Urman, R., Lurmann, F. and Gilliland, F. (2016). Association of Changes in Air Quality With Bronchitic Symptoms in Children in California, 1993-2012, *JAMA* **315**(14): 1491.

Bisetti, F. and El Morsli, M. (2012). Calculation and analysis of the mobility and diffusion coefficient of thermal electrons in methane/air premixed flames, *Combustion and Flame* **159**(12): 3518–3521.

Bjork, B. J., Bui, T. Q., Heckl, O. H., Changala, P. B., Spaun, B., Heu, P., Follman, D., Deutsch, C., Cole, G. D., Aspelmeyer, M., Okumura, M. and Ye, J. (2016). Direct frequency comb measurement of OD + CO –> DOCO kinetics, *Science* **354**(6311): 444–448.

Bohon, M. D., Guiberti, T. F., Mani Sarathy, S. and Roberts, W. L. (2017). Variations in non-thermal NO formation pathways in alcohol flames, *Proceedings of the Combustion Institute* **36**(3): 3995–4002.

Bonazza, T. J., VanVoorhies, K. L. and Smith, J. E. (1992). RF Plasma Ignition System Concept for Lean Burn Internal Combustion Engines.

Bourig, A., Thévenin, D., Martin, J.-P., Janiga, G. and Zähringer, K. (2009). Numerical modeling of H2O2 flames involving electronically-excited species O2(a1Δg)O2(a1Δg),O(1D)O(1D) and OH(2Σ+)OH(2Σ+), *Proceedings of the Combustion Institute* **32**(2): 3171–3179.

Brau, C. A. and Jonkman, R. M. (1970). Classical Theory of Rotational Relaxation in Diatomic Gases, *The Journal of Chemical Physics* **52**(2): 477–484.

Briggs, T., Alger, T. and Mangold, B. (2014). Advanced Ignition Systems Evaluations for High-Dilution SI Engines, *SAE International Journal of Engines* **7**(4): 2014–01–2625.

Callen, H. B. (1985). *Thermodynamics and an Introduction to Thermostatistics*, 2 edn, John Wiley & Sons, Inc., New York.

Carnot, N. L. S. (1897). *Reflections on the Motive Power of Heat*, 2nd edn, John Wiley & Sons, Inc., New York, NY.

Casey, T. (2016). *Electric field effects in combustion with non-thermal plasma*, Phd dissertation, University of California, Berkeley.

Casey, T. A., Han, J., Belhi, M., Arias, P. G., Bisetti, F., Im, H. G. and Chen, J.-Y. (2017). Simulations of planar non-thermal plasma assisted ignition at atmospheric pressure, *Proceedings of the Combustion Institute* **36**(3): 4155–4163.

Castela, M., Fiorina, B., Coussement, A., Gicquel, O., Darabiha, N. and Laux, C. O. (2016). Modelling the impact of non-equilibrium discharges on reactive mixtures for simulations of plasma-assisted ignition in turbulent flows, *Combustion and Flame* **166**: 133–147.

Cathey, C. D., Tang, T., Shiraishi, T., Urushihara, T., Kuthi, A. and Gundersen, M. A. (2007). Nanosecond Plasma Ignition for Improved Performance of an Internal Combustion Engine, *IEEE Transactions on Plasma Science* **35**(6): 1664–1668.

Chen, F. F. (2010). *Introduction to Plasma Physics and Controlled Fusion*.

Chukalovsky, A. A., Klopovsky, K. S., Palov, A. P., Mankelevich, Y. A. and Rakhimova, T. V. (2016). Reaction of hydrogen atoms with singlet delta oxygen (O 2 (a 1 Δ g)). Is everything completely clear?, *Journal of Physics D: Applied Physics* **49**(48): 485202.

Coleman, H. W. and Steele, W. G. (2009). *Experimentation, Validation, and Uncertainty Analysis for Engineers*, 3rd edn, John Wiley & Sons, Inc., Hoboken, NJ, USA.

Cook, J., Nuccitelli, D., Green, S. A., Richardson, M., Winkler, B., Painting, R., Way, R., Jacobs, P. and Skuce, A. (2013). Quantifying the consensus on anthropogenic global warming in the scientific literature, *Environmental Research Letters* **8**(2): 024024.

Cooney, S. and Yacobucci, B. D. (2007). *U.S. Automotive Industry: Policy Overview and Recent History*, Novinka Books, New York.

Cummins, C. L. (1976). Early IC and Automotive Engines, *A history of the Automotive Internal Combustion Engine*, Vol. 85, pp. 1960–1971.

Cummins, C. L. (1989). *Internal Fire*, 2nd edn, Society of Automotive Engineers, Inc., Warrendale, PA.

Dale, J., Checkel, M. and Smy, P. R. (1997). Application of high energy ignition systems to engines, *Progress in Energy and Combustion Science* **23**(5-6): 379–398.

Dale, J. D. and Oppenheim, A. K. (1981). Enhanced Ignition for I. C. Engines with Premixed Gases, *Trans, SAE Paper 810146*, Vol. 90, pp. 606–621.

Dale, J. D., Smy, P. R. and Clements, R. M. (1978). Laser Ignited Internal Combustion Engine - An Experimental Study, pp. 1539–1548.

Dames, E. E., Rosen, A. S., Weber, B. W., Gao, C. W., Sung, C. J. and Green, W. H. (2015). A detailed combined experimental and theoretical study on dimethyl ether/propane blended oxidation, *Combustion and Flame* **168**: 310–330.

DeFilippo, A. C. (2013). *Microwave-Assisted Ignition for Improved Internal Combustion Engine Efficiency*, Phd dissertation, UC Berkeley.

DeFilippo, A. C. and Chen, J.-Y. (2016). Modeling plasma-assisted methaneair ignition using pre-calculated electron impact reaction rates, *Combustion and Flame* **172**: 38–48.

DeFilippo, A., Saxena, S., Rapp, V., Dibble, R., Chen, J.-Y., Nishiyama, A. and Ikeda, Y. (2011). Extending the Lean Stability Limits of Gasoline Using a Microwave-Assisted Spark Plug, (1).

DeFilippo, A., Wolk, B., Chen, J.-Y., Dibble, R. W. and Ikeda, Y. (2015). Stability Limit Extension of a Wet Ethanol-fueled SI Engine using a Microwave-assisted Spark, *Advances in Automobile Engineering* **04**(02).

Dockery, D. W., Pope, C. A., Xu, X., Spengler, J. D., Ware, J. H., Fay, M. E., Ferris, B. G. and Speizer, F. E. (1993). An Association between Air Pollution and Mortality in Six U.S. Cities, *New England Journal of Medicine* **329**(24): 1753–1759.

Edgar, G. (1927). Measurement of Knock Characteristics of Gasoline in Terms of a Standard Fuel, *Industrial & Engineering Chemistry* **19**(1): 145–146.

Fridman, A. (2008a). Electric Discharges in Plasma Chemistry, *Plasma Chemistry*, Cambridge University Press, New York, NY, chapter 4, pp. 157–258.

Fridman, A. (2008b). Elementary Plasma-Chemical Reactions, *Plasma Chemistry*, Cambridge University Press, New York, NY, chapter 2, pp. 12–91.

Fridman, A. (2008c). Introduction to Theoretical and Applied Plasma Chemistry, *Plasma Chemistry*, Cambridge University Press, New York, NY, chapter 1, pp. 1–11.

Gauderman, W. J., Urman, R., Avol, E., Berhane, K., McConnell, R., Rappaport, E., Chang, R., Lurmann, F. and Gilliland, F. (2015). Association of Improved Air Quality with Lung Development in Children, *New England Journal of Medicine* **372**(10): 905–913.

Ghoniem, A. F. (2011). Needs, resources and climate change: Clean and efficient conversion technologies, *Progress in Energy and Combustion Science* **37**(1): 15–51.

Goodwin, D. G., Moffat, H. K. and Speth, R. L. (2014). Cantera: An object-oriented software toolkit for chemical kinetics, thermodynamics, and transport processes.

Griffiths, D. J. (1999). *Introduction to Electrodynamics*, 3rd edn, Prentice Hall, Inc, Upper Saddle River, NJ.

Guerreiro, C., Gonzalez Ortiz, A., de Leeuw, F., Viana, M. and Horalek, J. (2016). Air quality in Europe: 2016 report, *Technical Report 28/2016*, European Environment Agency, Luxembourg.

Guillaume, E., Marlair, G., Delacroix, A. and Drysdale, D. (2016). Considerations on combustion and fire behaviour of materials: A change of mind during the 18th century, *Journal of Fire Sciences* **34**(1): 69–84.

Haagen-Smit, A. J. (1952). Chemistry and Physiology of Los Angeles Smog, *Industrial & Engineering Chemistry* **44**(6): 1342–1346.

Haagen-Smit, A. J., Bradley, C. E. and Fox, M. M. (1953). Ozone Formation in Photochemical Oxidation of Organic Substances, *Industrial & Engineering Chemistry* **45**(9): 2086–2089.

Hagelaar, G. J. M. and Pitchford, L. C. (2005). Solving the Boltzmann equation to obtain electron transport coefficients and rate coefficients for fluid models, *Plasma Sources Science and Technology* **14**(4): 722–733.

Hampe, C., Bertsch, M., Beck, K. W., Spicher, U., Bohne, S. and Rixecker, G. (2015). Influence of High Frequency Ignition on the Combustion and Emission Behaviour of Small Two-Stroke Spark Ignition Engines, *JSAE/SAE 2013 Small Engine Technology Conference*, pp. 1–10.

Hampe, C., Kubach, H., Spicher, U., Rixecker, G. and Bohne, S. (2013). Investigations of Ignition Processes Using High Frequency Ignition, *SAE 2013 World Congress & Exhibition*.

Han, J. (2016). *Numerical Study of Electric Field Enhanced Combustion*, Phd dissertation, King Abdullah University of Science and Technology.

Harrington, J. A., Shishu, R. C. and Asik, J. R. (1974). A Study of Ignition System Effects on Power, Emissions, Lean Misfire Limit, and EGR Tolerance of a Single-Cylinder Engine-Multiple Spark versus Conventional Single Spark Ignition, *SAE Technical Paper*, number 740188, pp. 837–845.

Hayashi, N., Sugiura, A., Abe, Y. and Suzuki, K. (2017). Development of Ignition Technology for Dilute Combustion Engines, *SAE International Journal of Engines* **10**(3).

Heise, V., Farah, P., Husted, H. and Wolf, E. (2011). High Frequency Ignition System for Gasoline Direct Injection Engines, *SAE 2011 World Congress & Exhibition*.

Heywood, J. B. (1988). *Internal Combustion Engine Fundamentals*, 1st edn, McGraw-Hill.

Hoepke, B., Jannsen, S., Kasseris, E. and Cheng, W. K. (2012). EGR Effects on Boosted SI Engine Operation and Knock Integral Correlation, *SAE International Journal of Engines* **5**(2): 2012–01–0707.

Ikeda, Y., Nishiyama, A., Katano, H., Kaneko, M. and Jeong, H. (2009). Research and Development of Microwave Plasma Combustion Engine (Part II: Engine Performance of Plasma Combustion Engine).

Ionin, A. A., Kochetov, I. V., Napartovich, A. P. and Yuryshev, N. N. (2007). Physics and engineering of singlet delta oxygen production in low-temperature plasma, *Journal of Physics D: Applied Physics* **40**(2): R25–R61.

IPCC (2013). IPCC, 2013: Summary for Policymakers, *in* T. Stocker, D. Qin, G.-K. Plattner, M. Tignor, S. Allen, J. Boschung, A. Nauels, Y. Xia, V. Bex and P. Midgley (eds), *Climate Change 2013: The Physical Science Basis. Contribution of Working Group I to the Fifth Assessment Report of the Intergovernmental Panel on Climate Change*, Cambridge University Press, United Kingdom.

Johnston, R. W., Neuman, J. G. and Agarwal, P. D. (1975). Programmable Energy Ignition System For Engine Optimization, number 3, pp. 847–855.

Ju, Y. and Sun, W. (2015). Plasma assisted combustion: Dynamics and chemistry, *Progress in Energy and Combustion Science* **48**: 21–83.

Karl, T. R., Arguez, A., Huang, B., Lawrimore, J. H., McMahon, J. R., Menne, M. J., Peterson, T. C., Vose, R. S. and Zhang, H.-M. (2015). Possible artifacts of data biases in the recent global surface warming hiatus, *Science* **348**(6242): 1469–1472.

Keeling, C. D. (1960). The Concentration and Isotopic Abundances of Carbon Dioxide in the Atmosphere, *Tellus* **12**(2): 200–203.

King, J. and Böcker, O. (2013). Multiple Injection and Boosting Benefits for Improved Fuel Consumption on a Spray Guided Direct Injection Gasoline Engine, *Proceedings of the FISITA 2012 World Automotive Congress*, Vol. 189, Springer Berlin Heidelberg, pp. 229–241.

Kittel, C. and Kroemer, H. (1980). *Thermal Physics*, 2nd edn, W.H. Freeman and Company, San Francisco, CA.

Kolodziej, C. P., Ciatti, S., Vuilleumier, D., Das Adhikary, B. and Reitz, R. D. (2014). Extension of the Lower Load Limit of Gasoline Compression Ignition with 87 AKI Gasoline by Injection Timing and Pressure, number Di, pp. 1–14.

Konnov, A. A. (2015). On the role of excited species in hydrogen combustion, *Combustion and Flame* **162**(10): 3755–3772.

Kopecek, H., Maier, H., Reider, G., Winter, F. and Wintner, E. (2003). Laser ignition of methaneair mixtures at high pressures, *Experimental Thermal and Fluid Science* **27**(4): 499–503.

Kosarev, I. N., Aleksandrov, N. L., Kindysheva, S. V., Starikovskaia, S. M. and Starikovskiy, A. Y. (2008). Kinetics of ignition of saturated hydrocarbons by nonequilibrium plasma: CH4-containing mixtures, *Combustion and Flame* **154**(3): 569–586.

Kosarev, I. N., Kindysheva, S. V., Plastinin, E., Aleksandrov, N. L. and Starikovskiy, A. Y. (2016). Comparative Shock-Tube Study of Autoignition and Plasma-Assisted Ignition of C2-Hydrocarbons, *54th AIAA Aerospace Sciences Meeting*, number January, American Institute of Aeronautics and Astronautics, Reston, Virginia, pp. 1–5.

Lavoie, G. A., Heywood, J. B. and Keck, J. C. (1970). Experimental and Theoretical Study of Nitric Oxide Formation in Internal Combustion Engines, *Combustion Science and Technology* **1**(4): 313–326.

Lavoie, G. A., Ortiz-Soto, E., Babajimopoulos, A., Martz, J. B. and Assanis, D. N. (2013). Thermodynamic sweet spot for high-efficiency, dilute, boosted gasoline engines, *International Journal of Engine Research* **14**(3): 260–278.

Law, C. K. (2006). *Combustion Physics*, Cambridge University Press, New York.

Lawton, J. and Weinberg, F. J. (1969). *Electrical Aspects of Combustion*, Oxford University Press.

Lefkowitz, J., Ju, Y., Tsuruoka, R. and Ikeda, Y. (2012). A Studies of Plasma-Assisted Ignition in a Small Internal Combustion Engine, *50th AIAA Aerospace Sciences Meeting including the New Horizons Forum and Aerospace Exposition*, number January, American Institute of Aeronautics and Astronautics, Reston, Virigina, p. 8.

Lefkowitz, J. K. and Ombrello, T. (2017a). An exploration of inter-pulse coupling in nanosecond pulsed high frequency discharge ignition, *Combustion and Flame* **180**: 136–147.

Lefkowitz, J. K. and Ombrello, T. (2017b). Study of Nanosecond Pulsed High Frequency Discharge Ignition in a Flowing Methane/Air Mixture, *55th AIAA Aerospace Sciences Meeting*, number January, American Institute of Aeronautics and Astronautics, Reston, Virginia, pp. 1–10.

Lewis, J. (1985). Lead Poisoning: A Historical Perspective, *EPA Journal* **11**(4): 15–18.

Lieberman, M. A. and Lichtenberg, A. J. (2005a). Atomic Collisions, *Principles of Plasma Discharges and Materials Processing*, John Wiley & Sons, Inc., Hoboken, NJ, USA, chapter 3, pp. 43–85.

Lieberman, M. A. and Lichtenberg, A. J. (2005b). Molecular Collisions, *Principles of Plasma Discharges and Materials Processing*, John Wiley & Sons, Inc., Hoboken, NJ, USA, chapter 8, pp. 235–283.

Little, D. (2008). Opening the Door: Business, Diplomacy, and America's Stake in Middle East Oil, *American Orientalism: The United States and the Middle East since 1945*, 3rd edn, The University of North Carolina Press, Chapel Hill, chapter 2, pp. 43–75.

Llewellyn-Jones, F. (1966). *The Glow Discharge*, Methuen & Co, Ltd, London.

Lo, A., Cessou, A., Boubert, P. and Vervisch, P. (2014a). Space and time analysis of the nanosecond scale discharges in atmospheric pressure air: I. Gas temperature and vibrational distribution function of N 2 and O 2, *Journal of Physics D: Applied Physics* **47**(11): 115201.

Lo, A., Cessou, A., Boubert, P. and Vervisch, P. (2014b). Space and time analysis of the nanosecond scale discharges in atmospheric pressure air: II. Energy transfers during the post-discharge, *Journal of Physics D: Applied Physics* **47**: 115201.

Lockwood, M. (2008). Recent changes in solar outputs and the global mean surface temperature. III. Analysis of contributions to global mean air surface temperature rise, *Proceedings of the Royal Society A: Mathematical, Physical and Engineering Sciences* **464**(2094): 1387–1404.

Lovascio, S., Ombrello, T., Hayashi, J., Stepanyan, S., Xu, D., Stancu, G. D. and Laux, C. O. (2017). Effects of pulsation frequency and energy deposition on ignition using nanosecond repetitively pulsed discharges, *Proceedings of the Combustion Institute* **36**(3): 4079–4086.

Mandel, J. (1964). *The Statistical Analysis of Experimental Data*, John Wiley & Sons, Inc., New York.

Mariani, A. and Foucher, F. (2014). Radio frequency spark plug: An ignition system for modern internal combustion engines, *Applied Energy* **122**: 151–161.

McAllister, S., Chen, J.-Y. and Fernandez-Pello, A. C. (2011). *Fundamentals of Combustion Processes*, 1st edn, Springer, New York.

Mcintyre, D. L., Thompson, G. J. and Smith, J. E. (2001). The Coaxial Cavity Resonator as a RF IC Engine Ignition Source, number 724.

McQuarrie, D. A. and Simon, J. D. (1997). *Physical Chemistry: A Molecular Approach*, illustrate edn, University Science Books.

Melillo, J. M., Richmond, T. C. and Yohe, G. W. (2014). Climate Change Impacts in the United States: The Third National Climate Assessment, *Technical report*, U.S. Global Change Research Program.

Mintoussov, E. I., Pendleton, S. J., Gerbault, F. G., Popov, N. A. and Starikovskaia, S. M. (2011). Fast gas heating in nitrogenoxygen discharge plasma: II. Energy exchange in the afterglow of a volume nanosecond discharge at moderate pressures, *Journal of Physics D: Applied Physics* **44**(28): 285202.

Mondt, J. R. (1989a). An Historical Overview of Emission-Control Techniques for Spark-Ignition Engines: Part A – Prior to Catalytic Converters, *in* E. F. C. Somerscales and A. A. Zagotta (eds), *History of the Internal Combustion Engine*, The American Society of Mechanical Engineers, New York, NY, pp. 47–55.

Mondt, J. R. (1989b). An Historical Overview of Emission-Control Techniques for Spark-Ignition Engines: Part B – Using Catalytic Converters, *in* E. F. C. Somerscales and A. A. Zagotta (eds), *History of the Internal Combustion Engine*, The American Society of Mechanical Engineers, New York, NY, pp. 57—-63.

Moran, M. J. and Shapiro, H. N. (2000). *Fundamentals of Engineering Thermodyamics*, 4th edn, John Wiley & Sons, Inc., New York, NY.

Murphy, D. C., Sánchez-Sanz, M. and Fernandez-Pello, C. (2017). The role of non-thermal electrons in flame acceleration, *Combustion and Flame* **182**: 48–57.

Nagaraja, S., Yang, V. and Adamovich, I. V. (2013). Multi-scale modelling of pulsed nanosecond dielectric barrier plasma discharges in plane-to-plane geometry, *Journal of Physics D: Applied Physics* **46**(15): 155205.

Nakamura, N., Baika, T. and Shibata, Y. (1985). Multipoint Spark Ignition for Lean Combustion.

National Research Council (1972). *Lead: Airbone Lead in Perspective*, National Academy of Sciences, Washington, D.C.

National Research Council (1977a). *Energy and Climate: Studies in Geophysics*, National Academy of Sciences, Washington, D.C.

National Research Council (1977b). *Nitrogen Oxides*, National Academy of Sciences, Washington, D.C.

National Research Council (2002). *Effectiveness and Impact of Corporate Average Fuel Economy (CAFE) Standards*, National Academies Press, Washington, D.C.

National Research Council (2010). *Technologies and Approaches to Reducing the Fuel Consumption of Medium- and Heavy-Duty Vehicles*, National Academies Press, Washington, D.C.

National Research Council (2011). *Assessment of Fuel Economy Technologies for Light-Duty Vehicles*, National Academies Press, Washington, D.C.

National Research Council (2013). *Transitions to Alternative Vehicles and Fuels*, National Academies Press, Washington, D.C.

National Research Council (2015). *Cost, Effectiveness, and Deployment of Fuel Economy Technologies for Light-Duty Vehicles*, National Academies Press, Washington, D.C.

Nevin, R. (2000). How Lead Exposure Relates to Temporal Changes in IQ, Violent Crime, and Unwed Pregnancy, *Environmental Research* **83**(1): 1–22.

Ombrello, T., Won, S. H., Ju, Y. and Williams, S. (2010). Flame propagation enhancement by plasma excitation of oxygen. Part II: Effects of O2(a1Δg), *Combustion and Flame* **157**(10): 1916–1928.

Ono, R. (2016). Optical diagnostics of reactive species in atmospheric-pressure nonthermal plasma, *Journal of Physics D: Applied Physics* **49**(8): 083001.

Ono, R. and Oda, T. (2003). Formation and structure of primary and secondary streamers in positive pulsed corona discharge effect of oxygen concentration and applied voltage, *Journal of Physics D: Applied Physics* **36**(16): 1952.

Ono, R., Teramoto, Y. and Oda, T. (2010). Gas density in a pulsed positive streamer measured using laser shadowgraph, *Journal of Physics D: Applied Physics* **43**(34): 345203.

Osborne, R., Rouaud, C., Andersson, J., Pendlebury, K., Keenan, M., Hametner, T., Walters, D. and Bowen, J. P. (2014). Lean stratified turbocharged gasoline engines to meet emissions and fuel economy targets in 2018, *in* M. Bargende, H.-C. Reuss and J. Wiedemann (eds), *14. Internationales Stuttgarter Symposium*, Proceedings, Springer Fachmedien Wiesbaden, Wiesbaden, pp. 1325–1338.

Pacala, S. and Socolow, R. (2004). Stabilization Wedges: Solving the Climate Problem for the Next 50 Years with Current Technologies, *Science* **305**(5686): 968–972.

Pancheshnyi, S., Nikipelov, A., Anokhin, E. and Starikovskiy, A. (2014). SI Engine with Repetitive NS Spark Plug, *52nd Aerospace Sciences Meeting*, number January, American Institute of Aeronautics and Astronautics, Reston, Virginia, pp. 1–16.

Pendleton, S. J., Bowman, S., Carter, C., Gundersen, M. A. and Lempert, W. (2013). The production and evolution of atomic oxygen in the afterglow of streamer discharge in atmospheric pressure fuel/air mixtures, *Journal of Physics D: Applied Physics* **46**(30): 305202.

Peters, N. D. and Akih-Kumgeh, B. (2017). Spark and Laser Ignition of Iso-octane and Ethanol Blends, *10th U.S. National Combustion Meeting*, The Combustion Institute, College Park, MD.

Peterson, M. B., Barter, G. E., West, T. H. and Manley, D. K. (2014). A parametric study of light-duty natural gas vehicle competitiveness in the United States through 2050, *Applied Energy* **125**: 206–217.

Phuoc, T. X. and White, F. P. (1999). Laser-induced spark ignition of CH4/air mixtures, *Combustion and Flame* **119**(3): 203–216.

Pineda, D. I. and Chen, J.-Y. (2016). Effects of updated transport properties of singlet oxygen species on steady laminar flame simulations, *2016 Spring Technical Meeting of the Western States Section of the Combustion Institute*, number Paper 1B01, University of Washington, The Combustion Institute, Seattle, WA.

Pineda, D. I., Chen, J.-Y. and Dibble, R. W. (2016). Corona discharge ignition in a single cylinder research engine under boosted conditions, *2016 Spring Technical Meeting of the Western States Section of the Combustion Institute*, number 2A06, The Combustion Institute, The Combustion Institute, Seattle, WA.

Pineda, D. I., Shi, X., Casey, T. A. and Chen, J.-Y. (2017). Analysis of the errors associated with molecular transport parameters in combustion modeling and their effects on one-dimensional flame simulations, *10th U.S. National Combustion Meeting*, The Combustion Institute, College Park, MD, pp. 1–6.

Pineda, D. I., Wolk, B., Chen, J.-Y. and Dibble, R. W. (2016). Application of Corona Discharge Ignition in a Boosted Direct-Injection Single Cylinder Gasoline Engine: Effects on Combustion Phasing, Fuel Consumption, and Emissions, *SAE International Journal of Engines* **9**(3): 2016–01–9045.

Pineda, D. I., Wolk, B., Sennott, T., Chen, J.-Y., Dibble, R. W. and Singleton, D. (2017). The role of hydrodynamic enhancement on ignition of lean methane-air mixtures by pulsed nanosecond discharges for automotive engine applications, *Combustion Science and Technology* (In Revision).

Pineda, D. I., Wolk, B., Sennott, T., Chen, J.-Y., Dibble, R. W. and Singleton, D. R. (2015). Nanosecond Pulsed Discharge in a Lean Methane-Air Mixture, *Laser Ignition Conference*, Vol. C, Argonne National Laboratory, OSA Publishing, Lemont, IL, p. T5A.2.

Pintassilgo, C. D. and Guerra, V. L. (2015). On the different regimes of gas heating in air plasmas, *Plasma Sources Science and Technology* **24**(5): 055009.

Pischinger, S. and Heywood, J. B. (1991). A model for flame kernel development in a spark-ignition engine, *Symposium (International) on Combustion* **23**(1): 1033–1040.

Pomerance, R. (1986). The Dangers from Climate Warming: A Public Awakening, *EPA Journal* **12**(10): 15–16.

Pope, A. W. and Murdock, J. A. (1932). Compression-Ignition Characteristics of Injection-Engine Fuels, *Technical Report 320040*, Society of Automotive Engineers.

Popov, N. A. (2011). Fast gas heating in a nitrogenoxygen discharge plasma: I. Kinetic mechanism, *Journal of Physics D: Applied Physics* **44**: 285201.

Popov, N. A. (2016). Kinetics of plasma-assisted combustion: effect of non-equilibrium excitation on the ignition and oxidation of combustible mixtures, *Plasma Sources Science and Technology* **25**(4): 043002.

Quader, A. A. (1976). What Limits Lean Operation in Spark Ignition Engines-Flame Initiation or Propagation?, *SAE International*, number 760760, pp. 2374–2387.

Ragone, D. V. (1968). Review of Battery Systems for Electrically Powered Vehicles, *SAE Technical Papers*.

Rapp, V. H., DeFilippo, A. C., Saxena, S., Chen, J.-Y., Dibble, R. W., Nishiyama, A., Moon, A. and Ikeda, Y. (2012). Extending Lean Operating Limit and Reducing Emissions of Methane Spark-Ignited Engines Using a Microwave-Assisted Spark Plug, *Journal of Combustion* **2012**: 1–8.

Reitz, R. D. (2013). Directions in internal combustion engine research, *Combustion and Flame* **160**(1): 1–8.

Ren, W., Mitchell Spearrin, R., Davidson, D. F. and Hanson, R. K. (2014). Experimental and Modeling Study of the Thermal Decomposition of C3C5 Ethyl Esters Behind Reflected Shock Waves, *The Journal of Physical Chemistry A* **118**(10): 1785–1798.

Ricardo, H. R. (1922). Recent Research Work on the Internal-Combustion Engine, *Technical Report 220001*, Society of Automotive Engineers.

Ronney, P., Lim, E., McIlroy, A. and Syage, J. (2001). Laser Ignition Studies.

Rousso, A., Yang, S., Lefkowitz, J., Sun, W. and Ju, Y. (2017). Low temperature oxidation and pyrolysis of n-heptane in nanosecond-pulsed plasma discharges, *Proceedings of the Combustion Institute* **36**(3): 4105–4112.

SAE International Surface Vehicle Standard (2011). Engine Power Test Code - Spark Ignition and Compression Ignition - As Installed Net Power Rating, (SAE J1349).

Sagan, C. (1961). The Planet Venus: Recent observations shed light on the atmosphere, surface, and possible biology of the nearest planet, *Science* **133**(3456): 849–858.

Sarathy, S. M., Oßwald, P., Hansen, N. and Kohse-Höinghaus, K. (2014). Alcohol combustion chemistry, *Progress in Energy and Combustion Science* **44**: 40–102.

Schenk, A., Rixecker, D. G. and Bohne, S. (2015). Results from Gasoline and CNG Engine Tests with the Corona Ignition System EcoFlash, *Laser Ignition Conference*, Vol. 1, OSA, Argonne National Laboratory, p. W4A.4.

Schenk, A., Rixecker, G., Brichzin, V. and Becker, M. (2014). Potential of corona ignition on gas engines using EGR and lean combustion, *14. Internationales Stuttgarter Symposium*, pp. 373–388.

Schnepf, R. and Yacobucci, B. D. (2013). Renewable Fuel Standard (RFS): Overview and Issues, *Technical Report R40155*.

Schoettle, B. and Sivak, M. (2016). The Relative Merits of Battery-Electric Vehicles and Fuel-Cell Vehicles, *Technical Report UMTRI-2016-7*, The University of Michigan Transportation Research Institute, Ann Arbor, MI.

Scholte, T. and Vaags, P. (1959). Burning velocities of mixtures of hydrogen, carbon monoxide and methane with air, *Combustion and Flame* **3**: 511–524.

Seinfeld, J. H. (1975). *Air Pollution: Physical and Chemical Fundamentals*, McGraw-Hill, New York, NY.

Sevik, J., Wallner, T., Pamminger, M., Scarcelli, R., Singleton, D. and Sanders, J. (2016). Extending Lean and Exhaust Gas Recirculation-Dilute Operating Limits of a Modern Gasoline Direct-Injection Engine Using a Low-Energy Transient Plasma Ignition System, *Journal of Engineering for Gas Turbines and Power* **138**(11): 112807.

Shelton, E. M., Whisman, M. L. and Woodward, P. W. (1981). Trends in Motor Gasolines: 1942-1981, *Technical Report DOE/BETC/RI-82/4*, Department of Energy, Bartlesville Energy Technology Center, Bartlesville, OK.

Sher, E., Ben-Ya'ish, J., Pokryvailo, A. and Spector, Y. (1992). A Corona Spark Plug System for Spark-Ignition Engines, *SAE International Congress & Exposition*.

Shiraishi, T., Urushihara, T. and Gundersen, M. (2009). A trial of ignition innovation of gasoline engine by nanosecond pulsed low temperature plasma ignition, *Journal of Physics D: Applied Physics* **42**(13): 135208.

Shkurenkov, I. and Adamovich, I. V. (2016). Energy balance in nanosecond pulse discharges in nitrogen and air, *Plasma Sources Science and Technology* **25**(1): 015021.

Shkurenkov, I., Burnette, D., Lempert, W. R. and Adamovich, I. V. (2014). Kinetics of excited states and radicals in a nanosecond pulse discharge and afterglow in nitrogen and air, *Plasma Sources Science and Technology* **23**(6): 065003.

Sims, R., Schaeffer, R., Creutzig, F., Cruz-Núñez, X., D'Agosto, M., Dimitriu, D., Figueroa Meza, M., Fulton, L., Kobayashi, S., Lah, O., McKinnon, A., Newman, P., Ouyang, M., Schauer, J., Sperling, D. and Tiwari, G. (2014). Transport, *in* O. Edenhofer, R. Pichs-Madruga, Y. Sokona, E. Farahani, S. Kadner, K. Seyboth, A. Adler, I. Baum, S. Brunner, P. Eickemeier, B. Kriemann, J. Savolainen, S. Schlömer, C. von Stechow, T. Zwickel and J. Minx (eds), *Climate Change 2014: Mitigation of Climate Change. Contribution of Working Group III to the Fifth Assessment Report of the Intergovernmental Panel on Climate Change*, Cambridge University Press, Cambridge, UK, chapter 8, p. 599.

Singleton, D. (2015). Advanced Low-Energy Ignition System for Improved Fuel Efficiency and Transient Plasma Systems, *Technical Report EISG Grant No. 57828A/13-03TNG*, California Energy Commission, Sacramento, CA.

Singleton, D. R., Pendleton, S. J. and Gundersen, M. A. (2011). The role of non-thermal transient plasma for enhanced flame ignition in C2H4 air, *Journal of Physics D: Applied Physics* **44**(2): 022001.

Singleton, D., Sanders, J. M., Thomas, M. A., Sjöberg, M., Sevik, J., Pamminger, M. and Wallner, T. (2017). Demonstration of Improved Dilution Tolerance Using a Production-Intent Compact Nanosecond Pulse Ignition System, *Ignition Systems for Gasoline Engines*, Springer International Publishing, Cham, pp. 52–65.

Sivak, M. and Schoettle, B. (2016). What Individual Americans Can Do to Assist in Meeting the Paris Agreement, *Technical Report UMTRI-2016-7*, The University of Michigan Transportation Research Institute, Ann Arbor, MI.

Sivak, M. and Schoettle, B. (2017). Monthly monitoring of vehicle fuel economy and emissions.

Sjöberg, M., Zeng, W., Singleton, D., Sanders, J. M. and Gundersen, M. A. (2014). Combined Effects of Multi-Pulse Transient Plasma Ignition and Intake Heating on Lean Limits of Well-Mixed E85 DISI Engine Operation, *SAE International Journal of Engines* **7**(4): 2014–01–2615.

Smith, C. (2003). Force, Energy, and Thermodynamics, *in* M. J. Nye (ed.), *The Cambridge History of Science Volume 5: The Modern Physical and Mathematical Sciences*, Cambridge University Press, New York, NY, chapter 15, pp. 289–310.

Smith, G. P., Golden, D. M., Frenklach, M., Moriarty, N. W., Eiteneer, B., Goldenberg, M., Bowman, C. T., Hanson, R. K., Song, S., Gardiner, W. C., Lissianski, V. V. and Qin, Z. (1999). GRI-MECH 3.0.

Splitter, D., Pawlowski, A. and Wagner, R. (2016). A Historical Analysis of the Co-evolution of Gasoline Octane Number and Spark-Ignition Engines, *Frontiers in Mechanical Engineering* **1**(x).

Stancu, G. D., Kaddouri, F., Lacoste, D. A. and Laux, C. O. (2010). Atmospheric pressure plasma diagnostics by OES, CRDS and TALIF, *Journal of Physics D: Applied Physics* **43**(12): 124002.

Stanton, D. W. (2013). Systematic Development of Highly Efficient and Clean Engines to Meet Future Commercial Vehicle Greenhouse Gas Regulations, *SAE International Journal of Engines* **6**(3): 2013–01–2421.

Starik, A. M., Kozlov, V. E. and Titova, N. S. (2008). On mechanisms of a flame velocity increase upon activation of O 2 molecules in electrical discharge, *Journal of Physics D: Applied Physics* **41**(12): 125206.

Starik, A. M., Loukhovitski, B. I., Sharipov, A. S. and Titova, N. S. (2015). Physics and chemistry of the influence of excited molecules on combustion enhancement, *Philosophical Transactions of the Royal Society A: Mathematical, Physical and Engineering Sciences* **373**(2048): 20140341.

Starikovskaia, S. M. (2006). Plasma assisted ignition and combustion, *Journal of Physics D: Applied Physics* **39**(16): R265–R299.

Starikovskaia, S. M. (2014). Plasma-assisted ignition and combustion: nanosecond discharges and development of kinetic mechanisms, *Journal of Physics D: Applied Physics* **47**(35): 353001.

Starikovskiy, A. Y. and Aleksandrov, N. L. (2013). Plasma-assisted ignition and combustion, *Progress in Energy and Combustion Science* **39**(1): 61–110.

Stein, R. A., Anderson, J. E. and Wallington, T. J. (2013). An Overview of the Effects of Ethanol-Gasoline Blends on SI Engine Performance, Fuel Efficiency, and Emissions, *SAE International Journal of Engines* **6**(1): 2013–01–1635.

Steinfeld, J. I., Francisco, J. S. and Hase, W. L. (1998). *Chemical Kinetics and Dynamics*, 2nd edn, Prentice Hall, Upper Saddle River, NJ.

Stiles, R., Thompson, G. J. and Smith, J. E. (1997). Investigation of a Radio Frequency Plasma Ignitor for Possible Internal Combustion Engine Use, number 412.

Takana, H., Adamovich, I. V. and Nishiyama, H. (2014). Computational Simulation of Nanosecond Pulsed Discharge for Plasma Assisted Ignition, *Journal of Physics: Conference Series* **550**: 012051.

Thelen, B. C., Chun, D., Toulson, E. and Lee, T. (2013). A study of an energetically enhanced plasma ignition system for internal combustion engines, *IEEE Transactions on Plasma Science* **41**(12): 3223–3232.

Tholin, F., Lacoste, D. A. and Bourdon, A. (2014). Influence of fast-heating processes and O atom production by a nanosecond spark discharge on the ignition of a lean H2air premixed flame, *Combustion and Flame* **161**(5): 1235–1246.

Tilman, D., Socolow, R., Foley, J. A., Hill, J., Larson, E., Lynd, L., Pacala, S., Reilly, J., Searchinger, T., Somerville, C. and Williams, R. (2009). Beneficial Biofuels–The Food, Energy, and Environment Trilemma, *Science* **325**(5938): 270–271.

Tropina, A. A., Shneider, M. N. and Miles, R. B. (2016). Ignition by Short Duration, Nonequilibrium Plasma: Basic Concepts and Applications in Internal Combustion Engines, *Combustion Science and Technology* **188**(6): 831–852.

Turner, J., Popplewell, A., Patel, R., Johnson, T., Darnton, N., Richardson, S., Bredda, S., Tudor, R., Bithell, C., Jackson, R., Remmert, S., Cracknell, R., Fernandes, J., Lewis, A., Akehurst, S., Brace, C., Copeland, C., Martinez-Botas, R., Romagnoli, A. and Burluka, A. (2014). Ultra Boost for Economy: Extending the Limits of Extreme Engine Downsizing, *SAE International Journal of Engines* **7**(1): 387–417.

Uddi, M., Jiang, N., Mintusov, E., Adamovich, I. V. and Lempert, W. R. (2009). Atomic oxygen measurements in air and air/fuel nanosecond pulse discharges by two photon laser induced fluorescence, *Proceedings of the Combustion Institute* **32**(1): 929–936.

U.K. Department for Transport (2016). Vehicle Emissions Testing Programme: Moving Britain Ahead, *Technical Report April*, UK Department for Transport, London, UK.

U.S. DRIVE (2013). Advanced Combustion and Emission Control Technical Team Roadmap, *Technical Report June*, U.S. Driving Research and Innovation for Vehicle efficiency and Energy sustainability.

U.S. Energy Information Administration (2016). International Energy Outlook 2016, *Technical Report DOE/EIA-0484(2016)*, US DOE Office of Energy Analysis, Washington, D.C.

U.S. Energy Information Administration (2017). Monthly Energy Review: January 2017, *Technical Report DOE/EIA-0035(2017/1)*, U.S. Department of Energy, Washington, D.C.

U.S. Environmental Protection Agency (2016). Inventory of U.S. Greenhouse Gas Emissions and Sinks: 1990 2014, *Technical Report EPA 430-R-16-002*, U.S. Environmental Protection Agency, Washington, D.C.

U.S. EPA and U.S. NHTSA (2012). 2017 and Later Model Year Light-Duty Vehicle Greenhouse Gas Emissions and Corporate Average Fuel Economy Standards, *Federal Register* **77**(199): 62624–63200.

Vallinayagam, R., Vedharaj, S., Naser, N., Roberts, W. L., Dibble, R. W. and Sarathy, S. M. (2017). Terpineol as a novel octane booster for extending the knock limit of gasoline, *Fuel* **187**: 9–15.

VanVoorhies, K. L., Bonazza, T. J. and Smith, J. E. (1992). Analysis of RF Corona Discharge Plasma Ignition, *27th Intersociety Energy Conversion Engineering Conference (1992)*.

Varma, A. R. and Thomas, S. (2013). Simulation, Design and Development of a High Frequency Corona Discharge Ignition System, *Symposium on International Automotive Technology 2013*, pp. 1–10.

Vincenti, W. G. and Kruger, C. H. (1967). *Introduction to Physical Gas Dynamics*, 2 edn, John Wiley & Sons, Inc., New York.

Vuilleumier, D. M. (2016). *The Effect of Ethanol Addition to Gasoline on Low- and Intermediate-Temperature Heat Release under Boosted Conditions in Kinetically Controlled Engines*, Ph.d. disseration, University of California, Berkeley.

Vuilleumier, D., Taritas, I., Wolk, B., Kozarac, D., Saxena, S. and Dibble, R. W. (2016). Multi-level computational exploration of advanced combustion engine operating strategies, *Applied Energy* **184**: 1273–1283.

Warnatz, J., Maas, U. and Dibble, R. (2006). *Combustion: Physical and Chemical Fundamentals, Modeling and Simulation, Experiments, Pollutant Formation*, 4th edn, Springer, Berlin, Germany.

Westbrook, C. K., Naik, C. V., Herbinet, O., Pitz, W., Mehl, M., Sarathy, S. M. and Curran, H. J. (2011). Detailed chemical kinetic reaction mechanisms for soy and rapeseed biodiesel fuels, *Combustion and Flame* **158**(4): 742–755.

Wolk, B. and Chen, J.-Y. (2014). Computational Study of Partial Fuel Stratification for HCCI Engines Using Gasoline Surrogate Reduced Mechanism, *Combustion Science and Technology* **186**(3): 332–354.

Wolk, B., Chen, J.-Y. and Dec, J. E. (2015). Computational study of the pressure dependence of sequential auto-ignition for partial fuel stratification with gasoline, *Proceedings of the Combustion Institute* **35**(3): 2993–3000.

Wolk, B., DeFilippo, A. C., Chen, J.-Y., Dibble, R. W., Nishiyama, A. and Ikeda, Y. (2013). Enhancement of flame development by microwave-assisted spark ignition in constant volume combustion chamber, *Combustion and Flame* **160**(7): 1225–1234.

Wolk, B. M. and Ekoto, I. (2017). Calorimetry and Imaging of Plasma Produced by a Pulsed Nanosecond Discharge Igniter in EGR Gases at Engine-Relevant Densities, *SAE International Journal of Engines* **10**(3): 2017–01–0674.

Xu, D. A., Shneider, M. N., Lacoste, D. A. and Laux, C. O. (2014). Thermal and hydrodynamic effects of nanosecond discharges in atmospheric pressure air, *Journal of Physics D: Applied Physics* **47**(23): 235202.

Zel'dovich, Y. B. (1946). The Oxidation of Nitrogen in Combustion and Explosions, *Acta Physicochimica U.R.S.S.* **21**(4): 577–628.

Zheng, M. and Yu, S. (2015). Advanced Ignition Systems for Future Future Clean Combustion Engines: Review, *Journal of Automotive Safety and Energy* **6**(4): 295–313.